

https://dspace.org/

The synthesis and characterization of ZnS nanoparticles from zinc-based thiourea derivative complexes for potential use in photocatalysis

Lethobane, Manthako Hycinth

2017

https://hdl.handle.net/10539/25002

Lethobane, Manthako Hycinth (2017) The synthesis and characterization of ZnS nanoparticles from zinc-based thiourea derivative complexes for potential use in photocatalysis, University of the Witwatersrand, Johannesburg, <http://hdl.handle.net/10539/25002>

Downloaded from a DSpace repository. https://dspace.org/

THE SYNTHESIS AND CHARACTERIZATION OF ZnS NANOPARTICLES FROM ZINC-BASED THIOUREA DERIVATIVE COMPLEXES FOR POTENTIAL USE IN PHOTOCATALYSIS



WITS
UNIVERSITY

A dissertation submitted to the Faculty of Science, University of the Witwatersrand in partial fulfilment of the requirement for the degree

Master of Science (M.Sc.) in Chemistry

By

MANTHAKO HYCINTH LETHOBANE

Student number: 892367

Signed

_____on this 31st day of October 2017

Student: Ms. M. Lethobane

Signed by

_____on this 31st day of October 2017

Supervisor: Dr. I. Kotze

Co-Supervisor: Prof N. Moloto

Declaration

I declare that this dissertation that is submitted at the Faculty of Science, University of Witwatersrand Johannesburg is my own work and that I have not previously submitted it at any institution for examination.

Signed

_____on this 31st day of October 2017

Abstract

Nanotechnology has been instrumental in finding strategies of combating some of the world's grand challenges. Water scarcity and the growing industrialization have made it an imperative to find ways of cleaning water. Photocatalysis is a promising method for water purification personified by the use of solar energy as well as nanomaterials with tailored properties. Colloidal synthesis has made it possible to synthesize new materials with tailored properties, in particular the single-source precursor method has been found to be a useful method in synthesizing nanomaterials with high purity. In the synthesis of metal chalcogenides, the single-source precursor method has an advantage of the precursor having the desired metal-chalcogenide bond hence eliminating the possible formation of side products particularly metal oxides. Herein, acylthiourea (ATU) and thiourea (TU) zinc complexes were used as precursors for the synthesis of ZnS nanoparticles. Bis(N,N-diethyl-N'-benzoylthiourea)Zn(II) [$Zn(ATU)_2$] and bis(diaminomethylthio)Zn(II) chloride [$Zn(TU)_2Cl_2$] complexes were synthesized using a conventional method and characterized with elemental analysis, ^{1}H NMR , 2D NMR, COSY, FTIR, mass spectrometry and X-Ray crystallography.

The resultant precursors, $Zn(ATU)_2$ and $Zn(TU)_2Cl_2$ complexes were then thermolyzed to yield ZnS nanocrystals and characterized fully. Reaction parameters that included the synthetic time, temperature, concentration and capping agents were optimized for each single-source precursor in an attempt to control the nanoparticles yielded hence their properties. Time and temperature studies generally demonstrated the most pronounced effect and with an increase, they showed increasing particle sizes through the Ostwald ripening effect. Also visible from the TEM was that the temperature had an effect on the morphology of the nanoparticles. Increasing the precursor concentration resulted in the agglomeration of nanoparticles, while using different capping agents yielded similar nanoparticles with different degrees of agglomeration. Evident from the results the ATU precursor behaved similar to the TU precursor and generally the particles obtained from the two precursors regardless of the reaction condition were very small. Preliminary investigations into the use of the synthesized nanoparticles obtained from the two precursors revealed potential in photocatalytic degradation of Rhodamine B (RhB) dye in water. While smaller particles were obtained from the synthesized nanoparticles, the degradation efficiencies were lower than the

commercial ZnO and TiO_2. This is due to the presence of the long-chained capping agents on the synthesized particles blocking the interaction of the core ZnS and the light.

Acknowledgements

- First and foremost, I would like to thank the Almighty God for giving me strength throughout this project, for having seen this work to completion; I could have never done this without Him.
- Thank you to my supervisor, Dr. Izak Kotzé for his advice throughout the tenure of this project.
- I would also like to extend my gratitude to my co-supervisor, Prof Nosipho Moloto, for her constant guidance through it all, most importantly for never giving up on me; it has been a complete pleasure to work under your supervision.
- Thank you to my mother, 'Mamoipone Lethobane, for the support, the love, for the motivation and the constant reminder of why I started. To my brother and sisters, Thabo Molapo, T'sepiso Molapo and Moipone Lethobane; your support does not go unnoticed.
- To my partner, Sifiso Khumalo for being there throughout. For celebrating the best days and having your shoulder through the worst days, thank you.
- To my fellow group members of the inorganic and quantum dots group, thank you to everyone for making this a memorable experience. From you, I have gained life-long friendships, brothers and sisters.
- I would like to acknowledge the Wits' Microscopy and Microanalysis Unit, PXRD Facility and the X-ray crystallography group.
- Thank you to MERG for the funding awarded to me during the course of my studies.
- And finally, thank you to the School of Chemistry and the University of the Witwatersrand.

Presentations

- Inorganic group seminar, March 2015, University of the Witwatersrand, Oral Presentation.
- Catalysis and Materials group seminar, September 2015, University of the Witwatersrand, Oral Presentation.
- Inorganic group seminar, November 2015, University of the Witwatersrand, Oral Presentation.
- Inorganic group seminar, February 2016, University of the Witwatersrand, Oral Presentation.
- NanoAfrica conference, April 2016, UNISA, Poster presentation.
- Inorganic group seminar, June 2016, University of the Witwatersrand, Oral Presentation.
- Inorganic group seminar, August 2016, University of the Witwatersrand, Oral Presentation.
- NYRS symposium, October 2016, MINTEK, oral presentation. Awarded the 2nd best oral presentation.

Table of Contents

Declaration iii

Abstract iv

Presentations vii

List of Figures xii

List of Tables xvi

List of Schemes xvii

List of Abbreviations xviii

Chapter 1: Introduction

1.1. General background 1

1.2. Literature Review 3

1.2.1. Introduction to semiconductor nanocrystals 3

1.2.2. Optical and electronic Properties of nanocrystals 4

1.2.3. Nanoparticle preparation methods 6

1.2.4. Size Control of the nanocrystals 12

1.2.5. Applications in photocatalysis 12

1.3. Project motivation 15

1.4. Aim and Objectives 15

1.5. References 16

Chapter 2: Synthesis and characterisation of N, N-diethyl-N'-acylthiourea and thiourea zinc complexes

2.1. Introduction 23

2.2. Experimental 24

2.2.1. Instrumentation 24

2.2.2. Reagents 24

2.2.3. Synthesis of the *N*,*N*-diethyl-*N*'-benzoylthiourea ligand 24

2.2.4. Synthesis of the Bis(N,N-diethyl-N'-benzoylthiourea) Zinc (II) complex 25

2.2.5. Synthesis of Bis(diaminomethylthio) Zinc(II) Chloride 26
2.3. Results and discussion 27
2.3.1. Characterization of the ATU ligand 27
2.3.2. Characterization of $Zn(ATU)_2$ complex 29
2.3.3. Characterization of the zinc thiourea chloride 37
2.4. References 40
Chapter 3: Synthesis and Characterization of ZnS nanocrystals from $Zn(ATU)_2$
3.1. Introduction 42
3.2. Experimental procedures 43
3.2.1. Chemicals 43
3.2.2. Synthesis of ZnS nanoparticles using $Zn(ATU)_2$ complex as a single-source precursor 44
3.2.3. Characterisation techniques 46
3.2.3.1. Optical characterization 46
3.2.3.2. Electron microscopy 46
3.2.3.3. Powder X-Ray diffraction 46
3.3. Results and discussion 47
3.3.1. Effect of time on the properties of ZnS 47
3.3.1.1. Structural properties 47
3.3.1.2. Optical properties 51
3.3.2. Effect of temperature on the properties of ZnS 52
3.3.2.1. Structural properties 52
3.3.2.2. Optical properties 56
3.3.3. Effect of precursor concentration on the properties of ZnS 58
3.3.3.1. Structural properties 58
3.3.3.2. Optical properties 61
3.3.4. Effect of capping agent on the properties of ZnS 62
3.3.4.1. Structural properties 62
3.3.4.2. Optical properties 65

3.4. Conclusions 69
3.5. References 69

Chapter 4: Synthesis and Characterization of ZnS nanocrystals from the $Zn(TU)_2Cl_2$ complex

4.1. Introduction 72
4.2. Experimental procedure 74
4.2.1. Chemicals 74
4.2.2. Synthesis of ZnS nanoparticles using the $Zn(TU)_2Cl_2$ complex as a single-source precursor 74
4.2.3. Characterisation Techniques 75
4.2.3.1. Optical characterization 75
4.2.3.2. Electron microscopy 76
4.2.3.3. Powder X-Ray diffraction 76
4.3. Results and discussion 77
4.3.1. Temperature effects on the nanoparticles using $Zn(TU)_2Cl_2$ as a single-source precursor method 77
4.3.1.1. Structural properties 77
4.3.1.2. Optical properties 79
4.3.2. Precursor concentration effects on the nanoparticles using TU as a single-source precursor method 80
4.3.2.1. Structural properties 80
4.3.2.2. Optical properties 83
4.3.3. Capping agent effects on the nanoparticles using TU as a single-source precursor method 85
4.3.3.1. Structural properties of the oleylamine capped ZnS 85
4.3.3.2. Optical properties 87
4.4. Conclusions 89
4.5. References 90

Chapter 5: Photocatalytic degradation of Rhodamine B using the as-synthesized ZnS photocatalysts

5.1. Introduction 92
5.2. Experimental 94
1.5.1. Chemicals 94
1.5.2. Photocatalytic degradation of RhB over commercial and the a-synthesized photocatalysts 95
1.5.3. Characterisation Techniques 95
5.2.1.1. Powder X-Ray diffraction 95
5.2.1.2. Optical characterization 95
5.2.1.3. Electron microscopy 96
5.3. Results and discussion 96
5.4. Conclusions 100
5.5. References 101
Summary and Recommendations 103

List of Figures

Figure 1.1: Electronic energy states of a semiconductor showing the transition between molecules to QDs and bulk materials. 4

Figure 1.2: A display of the size-quantization effect as a color change of the aqueous solutions of CdSe/ZnS QDs. The particle sizes increase from left to right.[30] 5

Figure 1.3: A theoretical decomposition schematic for the preparation of TOPO-capped CdSe using a general single-source precursor. 9

Figure 1.4: A schematic diagram that represents and illustrates La Mer's theory on nucleation.[75] 11

Figure 1.5: Photocatalytic activation of a semiconductor nanocrystal.[84] 13

Figure 2.1: ^{1}H NMR spectrum of the ATU ligand in $CDCl_3$ at 300 K. (*Please note break between 4.2 ppm and 7.1 ppm*) 28

Figure 2.2: Infrared spectrum of a) ATU (black) and b) $Zn(ATU)_2$ (red). 29

Figure 2.3: ^{1}H NMR spectrum of the $Zn(ATU)_2$ complex in $CDCl_3$ at 300 K. (Please note breaks between 4.2 ppm and 7.1 ppm also between 1.8 ppm and 3.6 ppm) 30

Figure 2.4: ^{1}H,^{1}H COSY spectra of Zn(ATU)2 in $CDCl_3$ at 300 K where (a) is the aliphatic region and (b) is the aromatic region. 32

Figure 2.5: ^{1}H, ^{13}C HSQC spectra of $Zn(ATU)_2$ in $CDCl_3$ where (a) is the aliphatic region and (b) is the aromatic region. 33

Figure 2.6: ^{13}C NMR spectra of $Zn(ATU)_2$ in $CDCl_3$ at 300 K with an insert of an enlarged view of the $C^{4,4'}$ and $C^{5,5'}$ carbons. 34

Figure 2.7: Molecular structure of $Zn(ATU)_2$ where (a) is the ORTEP diagram and (b) and (c) are the general packing diagrams. 36

....37

Figure 2.8: ^{13}C NMR spectrum of a) Zn(TU)2Cl2 and b) HL2 in DMSO-d6 at 300 K. 37

Figure 3.1: A structure of Zn(ATU)2. 43

Figure 3.2: PXRD patterns of zinc sulfide nanoparticles collected from $Zn(ATU)_2$ at (a) 5 min, (b) 10 min, (c) 15 min, (d) 20 min, (e) 25 min and (f) 30 min in OAm at 160 °C. 48

Figure 3.3: TEM micrographs of zinc sulfide nanoparticles collected from $Zn(ATU)_2$ at (a) 5 min, (b) 10 min, (c) 15 min, (d) 20 min, (e) 25 min and (f) 30 min in OAm at 160 °C. 50

Figure 3.4: (a) Absorption and (b) emission spectra (λ_{exc}= 250 nm) of zinc sulfide nanoparticles collected from $Zn(ATU)_2$ at 5 min, 10 min, 15 min, 20 min, 25 min and 30 min in OAm at 160 °C. 51

Figure 3.5: PXRD patterns of zinc sulfide nanoparticles collected from $Zn(ATU)_2$ at (a) 160 °C, (b) 180 °C, (c) 200 °C, (d) 220 °C, (e) 240 °C and (f) 260 °C in OAm. 53

Figure 3.6: TEM micrographs of zinc sulfide nanoparticles collected from Zn(ATU)2 at (a) 160 °C, (b) 180 °C, (c) 200 °C, (d) 220 °C, (e) 240 °C and (f) 260 °C in OAm after 20 min 55

Figure 3.7: (a) Absorption and (b) emission spectra of zinc sulfide nanoparticles (λ_{exc}= 250 nm) collected from $Zn(ATU)_2$ at 160 °C, 180 °C, 200 °C, 220 °C, 240 °C and 260 °C in OAm.....57

Figure 3.8: PXRD patterns of zinc sulfide nanoparticles collected from $Zn(ATU)_2$ at (a) 1:15, (b) 2.5:15, (c) 5:15, (d) 7.5:15 and (e) 10:15 in OAm. 59

Figure 3.9: TEM micrographs of zinc sulfide nanoparticles collected from $Zn(ATU)_2$ at (a) 1:15, (b) 2.5:15, (c) 5:15, (d) 7.5:15 and (e) 10:15. 60

Figure 3.10: (a) Absorption and (b) emission spectra of zinc sulfide nanoparticles (λ_{exc}= 250 nm) collected from zinc (II) diethyl acylthiourea at 160 °C in OAm for various ratios (1:15, 2.5:15, 5:15, 7.5:15 and 10:15).....61

Figure 3.11: PXRD patterns of zinc sulfide nanoparticles collected from $Zn(ATU)_2$ in (a) OAm, (b) 1-DDT and (c) HDA after 20 minutes at 160 °C at a 2.5:15 ratio. 64

Figure 3.12: TEM micrographs of zinc sulfide nanoparticles from $Zn(ATU)_2$ in (a) OAm, (b) 1-DDT and (c) HDA after 20 minutes at 160 °C at a 2.5:15 ratio. 65

Figure 3.13: (a) Absorption and (b) emission spectra of zinc sulfide nanoparticles (λ_{exc}= 250 nm) collected from zinc(II) diethyl acyl thiourea at 160 °C for various capping agents (OAm, 1-DDT, and HDA) 66

Figure 3.14: Size trends of the nanoparticles extracted from XRD using the Scherrer equation as a function of varying reaction conditions 68

Figure 4.1: The structure of (a) thiourea and (b) a general structure of substituted thiourea ligands. 72

Figure 4.2: A structure of $Zn(TU)_2Cl_2$. 73

Figure 4.3: PXRD patterns of zinc sulfide nanoparticles collected from $Zn(TU)_2Cl_2$ at (a) 160 °C, (b) 200 °C and (c) 260 °C. 78

Figure 4.4: TEM micrographs of zinc sulfide nanoparticles collected from $Zn(TU)_2Cl_2$ at (a) 160 °C, (b) 200 °C and (c) 260 °C. 79

Figure 4.5: (a) Absorption and (b) Emission spectra of zinc sulfide nanoparticles collected from $Zn(TU)_2Cl_2$ at different temperatures. 80

Figure 4.6: PXRD patterns of zinc sulfide nanoparticles collected from $Zn(TU)_2Cl_2$ at different precursor concentrations. 81

Figure 4.7: TEM micrographs of zinc sulfide nanoparticles collected from $Zn(TU)_2Cl_2$ at (a) 1:15, (b) 2.5:15, (c) 5:15, (d) 7.5:15 and (e) 10:15 precursor to capping agent molar ratios. .83

Figure 4.8: (a) Absorption and (b) Emission spectra of zinc sulfide nanoparticles collected from $Zn(TU)_2Cl_2$ at different precursor concentrations. 84

Figure 4.9: PXRD patterns of zinc sulfide nanoparticles collected from $Zn(TU)_2Cl_2$ at different precursor concentrations. 86

Figure 4.10: TEM micrographs of zinc sulfide nanoparticles collected from $Zn(TU)_2Cl_2$ in (a) OAm, (b) 1-DDT and (c) HDA.....87

Figure 4.11: (a) Absorption and (b) Emission spectra of zinc sulfide nanoparticles collected from $Zn(TU)_2Cl_2$ at different capping agents 88

Figure 4.12: Size trends of the nanoparticles extracted from XRD using the Scherrer equation as a function of varying reaction conditions. 89

Figure 5.1: The chemical structure of RhB.....94

Figure 5.2: XRD pattern of (a) ZnS QDs synthesized from the ATU ligand, (b) ZnS QDs synthesized from the TU ligand, (c) commercial TiO_2 (anatase) and (d) commercial ZnO. ...97

Figure 5.3: TEM micrographs of (a) ZnS QDs synthesized from the ATU ligand, (b) ZnS QDs synthesized from the TU ligand, (c) commercial anatase and (d) commercial ZnO. 98

Figure 5.4: The absorbance spectra changes of RhB solution in (a) commercial TiO_2(anatase), (b) commercial ZnO, (c) ZnS nanoparticles synthesized from $Zn(ATU)_2$ and (d) ZnS nanoparticles synthesized from $Zn(TU)_2Cl_2$. 99

Figure 5.5: Photocatalytic degradation kinetics of RhB using different photocatalysts under visible light. (C_0 and C are the equilibrium concentrations of RhB before and after irradiation, respectively). 100

List of Tables

Table 2.1: Ligands and complexes synthesized with full and abbreviated names.....27
Table 2.2: Crystal data and structure refinement for $Zn(ATU)_2$.....38
Table 2.3: Bond lengths [Å] and angles [°] for $Zn(ATU)_2$.....39
Table 3-1: Reaction parameters for time experiments.....45
Table 3-2: Reaction parameters for temperature experiments.....45
Table 3-3: Reaction parameters for the precursor: capping agent molar ratio experiments.....45
Table 3-4: Reaction parameters for the coordinating solvent experiments.....46
Table 3-5: Optical properties of ZnS nanocrystals of the time experiments synthesized from $Zn(ATU)_2$.....52
Table 3-6: Optical properties of ZnS nanocrystals of the temperature experiments synthesized from $Zn(ATU)_2$.....57
Table 3-7: Optical Properties of ZnS nanocrystals of the concentration experiments synthesized from $Zn(ATU)_2$.....62
Table 3-8: Optical Properties of ZnS nanocrystals of the capping agent experiments synthesized from $Zn(ATU)_2$.....66
Table 4-1: Reaction parameters for temperature experiments.....75
Table 4-2: Reaction parameters for the precursor: capping agent molar ratio experiments.....75
Table 4-3: Reaction parameters for the coordinating solvent experiments.....75
Table 4-4: Optical properties of ZnS nanocrystals of the temperature experiments synthesized from $Zn(TU)_2Cl_2$.....80
Table 4-5: Optical Properties of ZnS nanocrystals of the concentration experiments synthesized from $Zn(TU)_2Cl_2$.....84
Table 4-6: Optical Properties of ZnS nanocrystals of the capping agent experiments synthesized from $Zn(TU)_2Cl_2$.....88
Table 5-1: Reaction conditions used to prepare the a-synthesized ZnS nanoparticles from both the ATU and the TU precursors.....94

List of Schemes

Scheme 2.1: Schematic diagram showing the general procedure of the formation of the ATU ligand.....25

Scheme 2.2: A schematic diagram displaying the synthesis of the $Zn(ATU)_2$ complex.....26

Scheme 3.1: A scheme showing the thermolysis of $Zn(ATU)_2$ in the presence of a capping agent to form metal chalcogenides. 44

Scheme 3.2: Different capping agent molecules and their functionalities.....63

Scheme 5.1: Mechanism of photocatalytic mineralization of Rhodamine B.[17].....96

List of Abbreviations

DBPs	disinfecting by-products
VB	valence band
CB	conduction band
AOPs	advanced oxidation processes
UV	ultraviolet
QDs	quantum dots
TOPO	tri-n-octylphosphine oxide
TOPSe	trioctylphosphine selenide
mL	millilitres
TU	thiourea
ATU	*N,N'*-diethyl-*N'*-acylthiourea
$Zn(TU)_2Cl_2$	Bis(diaminomethylthio) Zinc(II) Chloride
$Zn(ATU)_2$	Bis(N,N-diethyl-N'-benzoylthiourea) Zinc (II)
CHNS	elemental analysis
$CDCl_3$	deuterated chloroform
DMSO	dimethylsulfoxide
ppm	parts per million
mol	molar
COSY	correlation ordered spectroscopy
NMR	nuclear magnetic resonance
HSQC	heteronuclear single quantum coherence
FT-IR	fourier transform infra-red
ATR	attenuated total reflection
DEPT	distortionless enhancement by polarization
OAm	oleylamine
1-DDT	dodecanethiol
HDA	hexadecylamine
TOP	trioctylphosphine
min	minutes
TEM	transmission electron microscopy
XRD	X-Ray diffraction
FWHM	full width at half maximum

PXRD	powder X-Ray diffraction
UV-Vis	ultra violet visibility
AACVD	aerosol assisted chemical vapour deposition
JCPDS	joint committee on powder diffraction standards
PVP	polyvinyl pyrrolidone
MB	methylene blue
RhB	Rhodamine B

Chapter 1: Introduction

1.1. General background

For millions of years, life on earth has been dependent on water for survival. Even though 70% of the earth's surface is covered with water,[1] only 3% of the water is available for consumption. Water scarcity has been reported to be a critical concern for South Africa and the world as whole as a consequence of the uneven distribution of both the human population and water resources across the globe.[2] More recently, it has become even more apparent that fresh water scarcity is becoming a threat to sustainable development of human society due to the steadily increasing demand.[3] As a result of the rapidly increasing population, improving living standards, changing consumption patterns and the expansion of irrigated agriculture and consequently, water use per capita in many areas of the world, the world's population has been found to be currently living under physical water scarcity.[4] Adding on to the strain, there has been a continued increase in the demand for water for non-agricultural uses such as urban and industrial uses resulting in water pollution in most cases.[5] Industrial activities which are dependent on using commercial colourants generate large amounts of waste water which if not managed properly, are discharged into rivers, landfills, and nearby water sources.[6] Waste water from these industrial processes is concentrated with highly reactive and toxic dyes which contribute as major pollutants.[7] The discharge of the dye-containing effluents into the water environment is undesirable as they exhibit poor biodegradability, therefore, considerable research has been directed towards the discovery of effective water treatment techniques that will significantly reduce water pollution levels.[8] Different methods have been employed in the effort to treat waste-water to remove organic and inorganic contaminants. Physical, chemical and biological techniques have been investigated and these include chemical oxidation (chlorination and ozonization), adsorption and air stripping methods. Most of these methods have a number of limitations due to either their corresponding energy sources, their selective treatment of pollutants and/or harmful waste generation.[9]

Chemical oxidation (chlorination and ozonation) as a method of decontamination is unable to break down all organic substances and is only economically feasible for the removal of pollutants in high concentrations due to the high cost involved in. Chlorination results in the

formation of disinfecting by-products (DBPs) such as trihalomethanes, which have been identified as possible carcinogens and also result in secondary pollution.[10] The efficiency of this process is affected by the presence of nitrite and suspended solid particles which would need high investments for filter systems.[10] While ozonation does not form the hazardous DBPs associated with the chlorination process, it was found to require highly-priced capital costs as it has to be generated on site with strict monitoring of the gasses used and generated.[11] Additionally, small amounts of bromate ions (3–68 ppb) have been discovered as by-products and are suspected to be cancer agents.[10] Economic reasons, therefore, explain why the development of re-usable inorganic adsorbents is attracting increasing interest. Adsorption techniques have been reported to make use of activated carbon, this has shown great potential in effectively removing organic pollutants, but the regeneration process of this method is also expensive.[12] The effectiveness of this method has also been reduced dramatically due to carbon being a non-selective adsorbent which adsorbs almost all natural organic matter present in water, resulting in the incapacity to accumulate pollutants.[10] Other methods such as air stripping have been investigated. Air stripping, which decontaminates water by extracting volatile organics has shown a good capacity to treat wastewater. However, its downfall, is that pollutants are transferred from water into the air instead of being destroyed.[10] This poses a new environmental problem of air pollution and requires methods that will involve air cleaning techniques.

In the last decade, premier alternatives to conventional water purification have been that of advanced oxidation processes (AOPs), which have shown to be effective in the destruction of refractory pollutants (e.g. microorganisms, industrial toxins).[13] AOPs constitute a promising technology for the treatment of wastewaters that is characterized by their capability to exploit the high reactivity of hydroxyl (HO) radicals in driving the oxidation process.[14] Of particular interest, photocatalysis is an emerging AOP that has been widely employed for the treatment of several dyes and has demonstrated its efficiency in the elimination of organic and inorganic pollutants from aqueous and gaseous media.[15,16] The process makes use of semiconducting metal oxides and chalcogenides to create oxidized holes, which directly degrade the adsorbed pollutants. The small sizes and high optical activity of metal chalcogenides make them attractive tools for applications in photocatalysis. Unlike the traditional methods mentioned, photocatalysis makes use of the very abundant solar energy and can be achieved under room temperature in a few hours without the formation of any polycyclic products.[10]

1.2. Literature Review

1.2.1. Introduction to semiconductor nanocrystals

The emergence of nanotechnology since the 1980's has attracted a great deal of attention due to its potential in the development of new industries that are based on cost-efficient materials and contribution to a sustainable economic growth.[24] In general, the term nanoparticle refers to particles containing a couple of hundred to a couple of thousand atoms, where materials in the size regime of 1 to 100 nm bridge the gap between individual atoms and the solid state.[25] Semiconductor materials generally have electrical conductivity lying between a conductor and an insulator.[26] In semiconductors nanomaterials, the highest occupied energy band, the valence band (VB) is completely filled with electrons and the next one, which is empty is the conduction band (CB). A unique property of these semiconductor nanoparticles is their ability to alter their resistivity by up to ten orders of magnitude,[27] a function which is either impossible to alter or very difficult in the case of conductors and insulators. The term semiconductor nanoparticle is used interchangeably with terms semiconductor nanocrystal and quantum dots (QDs). The small dimensions of QDs result in material properties that are different from their corresponding bulk materials and also enable the exploitation of the useful properties of the crystalline materials. Because of the small sizes, QDs have a variety of applications in areas of optoelectronics, catalysis and medicine systems to mention a few.

The bulk semiconductors are characterized by band gap energy (E_g), which is the minimum energy required to excite an electron from the VB to the CB. (Figure 1.1) When the absorption of the photon energy is greater than the E_g, the excitation of the negatively charged electron (e^-) leaves behind an orbital hole (h^+) in the VB. The presence of an electric field may then potentially mobilize the e^- and h^+ to produce a current, but their lowest energy state is an electrostatically bound e^-/h^+ pair, known as the exciton. The relaxation of the excited electron back to the valence band destroys the exciton and is a process known as e^-/h^+ recombination.[28]

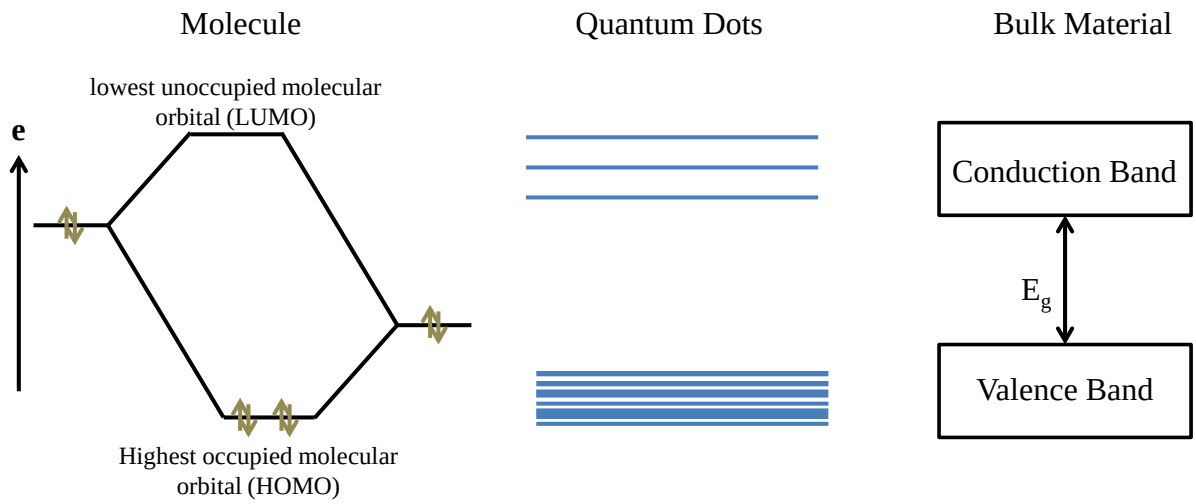


Figure 1.1: Electronic energy states of a semiconductor showing the transition between molecules to QDs and bulk materials.

The exciton has a defined size within the crystal defined by the Bohr radius (a_B). The Bohr radius of the bulk exciton depends on the effective masses of the electrons m_e and holes m_h and on the high-frequency dielectric constant of the material, ε: (Equation 1.1)

$$a_B = \frac{\hbar^2 \varepsilon}{e^2}\left[\frac{1}{m_e^*} + \frac{1}{m_h^*}\right] \qquad (1.1)$$

If the size of a semiconductor nanocrystal is smaller than the size of the exciton, the charge carriers become spatially confined, which raises their kinetic energy.[29] Therefore, the exciton size defines the transition between the regime of bulk crystal properties and the quantum confinement regime, in which the optical and electronic properties are dependent on the nanocrystal size.

1.2.2. Optical and electronic Properties of nanocrystals

The most striking property of QDs is their massive change in optical properties as a function of size. A well-known demonstration of the size-dependant properties of QDs is the colour change witnessed in the aqueous solutions of CdSe/ZnS QDs dispersed in toluene (UV light irradiation) with decreasing particle sizes (Figure 1.2).[30] As size is increased, the electronic excitations shift to a lower energy, and the oscillator strength is no longer concentrated into just a few transitions.[31]

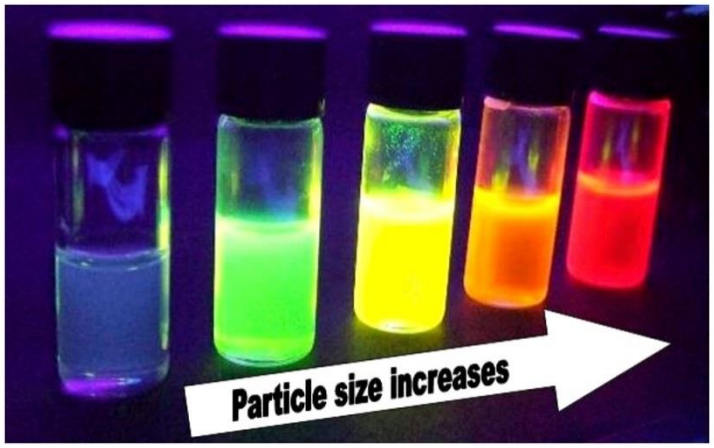


Figure 1.2: A display of the size-quantization effect as a color change of the aqueous solutions of CdSe/ZnS QDs. The particle sizes increase from left to right.[30]

QDs with diameters ranging between 1-20 nm have become a major interdisciplinary area of research interest. Efros *et al.*[32], Ekimov *et al.*[33], Henglein *et al.*[34] and Brus *et al.*[35] represent QDs as a system lying in the transition regime between the bulk solid and molecules, and report that the small dimensions of the nanoparticles result in properties differing from those seen in the corresponding bulk materials. The reasons for this behaviour is reported to be due to two fundamental factors.[36] The first is described as the high dispersity of nanocrystalline systems; the ratio of surface atoms to those in the interior is reported to increase as the particles get smaller, which results in surface properties playing an important role in the physical and optical properties of QDs. The second incident is related to the actual size of the nanoparticles. The change in electronic properties of semiconductor nanocrystals is inevitable; as the sizes of the particles become smaller, the band gap gradually increases as a result of quantum confinement effects.[37] This effect is a result of charge carriers that are treated as "particles in a box", where the size of the box is given by the dimensions of the crystallites that gives rise to the valence and the conduction band splitting into discrete energy levels rather than a continuous band as in the corresponding bulk material.[38] The coulombic interaction in these materials cannot be neglected; they have higher kinetic energy compared to their bulk counterparts. The major consequence of the quantum confinement effect in semiconductors is an increase of the apparent band gap with decrease of the particle size which is experimentally observed as a blue shift in the absorption onset.[39] This prediction has been confirmed experimentally for a wide range of semiconductor nanocrystallites.[27,36,40–43]

1.2.3. Nanoparticle preparation methods

Since the discovery of QDs, investigations into their synthesis in order to tailor their properties by controlling their sizes and shapes have been well documented.[44] Particle sizes and the method of nanoparticle preparation determine the physical, optical and electronical properties of QDs produced, giving scientists the ability to uniquely change the electronic and chemical properties of a semiconductor material by simply controlling particle sizes and preparative conditions used.[37] While there are a number of reported methods of synthesis, not all methods will work well for the preparation of well-passivated and mono-dispersed QDs. In earlier works, Matijevic[45] reported on the development of reproducible synthetic methods for near mono-dispersed colloidal particles. Over the years, significant progress on the synthesis of semiconductor nanoparticle materials showing quantum size effects has been achieved. The colloidal synthesis of nanoparticles in a suitable solvent medium is referred to as a "bottom-up" way to achieve nanostructured systems. Ideally, synthetic routes should yield desired particle sizes over the largest possible range, particles with narrow size distributions, good crystallinity, controllable surface functionalization and high luminescent quantum yields.[29]

1.2.3.1. Colloidal synthesis of QDs

The synthesis of quantum dots dates back to the 19th century, with the preparation of colloids of relatively monodispersed gold nanoparticles by Faraday.[46] The availability of reliable colloidal routes leading to QDs that are uniform in size, composition, shape and surface chemistry is vital for both the study of their size-dependant properties and employment in various applications.[37] Earlier work was done on group II-VI compounds that included CdS and CdSe.[47] Initially, the arrested precipitation method was used with the strategy of "keeping the particles small".[48] The synthesis of highly monodispersed colloids was first explained by La Mer *et al.* who suggested that seeds of very small particles would collide and grow into larger ones, which are more thermodynamically stable, thereby resulting into monodispersed particles.[49] This process was termed Ostwald ripening. The driving force of the Ostwald ripening process is the low solubility of nanoparticles which can be achieved by an appropriate solvent, temperature, passivating agent and pH. Brus *et al.*[50] described the process for the synthesis of CdS nanoparticles, which involved the reaction between aqueous solutions of $CdSO_4$ and $(NH_4)_2S$. Nucleation kinetics was altered using pH in order to control the sizes of the nanocrystalline CdS particles. The method was reported to work well in the

growth of some nanoparticles and failed for others due to air sensitivity and poor crystallinity of the material.[51]

1.2.3.2. Synthesis of QDs in a structured medium

More recently, synthesis in a structured medium have appeared in literature. Nanoparticles are reported to grow in host materials that have defined spaces within their structure, with the host materials acting as chambers. These include preparing nanoparticles using zeolites, micelles, sol-gel system, polymers and molecular sieves.[49] The downfall of this method is that the host structure degrades upon the formation of the nanoparticles with particle dimensions being decided by the restricting material. The disadvantage of this method is the use of aqueous solvents and materials which could lead to particle degradation with time.

1.2.3.3. Organometallic routes

A popular method for the preparation of high quality nanoparticles is the molecular precursor method which uses organometallic and/or metal organic compounds under anaerobic conditions. This method was first described by Murray *et al.* in 1993.[47] In this method, $(CH_3)_2Cd$ was dissolved in tri-n-octylphosphine oxide (TOPO) and a chalcogenide source, trioctylphosphine selenide (TOPSe), the solution was injected into a hot TOPO solution at temperatures varying from 120 °C to 300 °C. The method produced TOPO-capped nanocrystallites of CdSe of high quality and low defects. However, this method made use of hazardous material, $(CH_3)_2Cd$, introducing drawbacks for the method.

1.2.3.4. Single-source precursor method

The single-source precursor method is a modification of the organometallic method report above where less toxic precursors are used. Originally, most potential single-molecular precursors were intended for use in the growth of semiconductor thin films from chemical vapour deposition (CVD) techniques but their low volatility and lack stoichiometric control put them at a disadvantage. Among others, Barron *et al.* used the gallium and indium selenium clusters, $[(^tBu)GaSe]_4$ and $[(EtMe_2C)InSe]_4$ to produce nanoparticles.[52] Because of the already present metal-chalcogenide bond within the precursor, this method provides the opportunity to form QDs in a one-pot step which possesses great advantages over the traditional methods. One of the method's most attractive advantages is the ability to avoid the

use of volatile and toxic precursors. In addition, synthesis can be achieved at lower temperatures (up to 300 °C).[37] Because this method is performed under anaerobic conditions, the resulting nanoparticles are moisture stable. The single source precursor method is considered a facile, reproducible route for well-defined nanocrystals.[53]

The use of single-source precursor method has provided researchers with a simple route to high quality, air stable and low toxicity samples of nanoparticles.[54] This method has been extensively studied by researchers, amongst many, Trindade and O'Brien used cadmium dithio and diselenocarbamate (CH_2NSe_2/CH_2NSe_2) complexes as precursors for the preparation of TOPO-capped CdS/CdSe QDs.[55] They reported that the formation of nanoparticles is driven by the decomposition of precursors and the termination of growth occurs when the precursor supply is depleted. In their earlier works, O'Brien and group prepared metal complexes of bis(alkyl/selenocarbamato)Cd(II)/Zn(II) and thermolyzed the complexes in TOPO to give metal sulphide and metal selenide nanoparticles.[56] There have been several other types of precursors having a metal sulphide bond that have been used for the preparation of metal sulphide nanoparticles. Xanthates and dithiocarbamates are very close in structure making them the ideal precursors for metal sulphide nanoparticles. Metal sulphide nanoparticles of different morphologies (M = Cd, Zn, Hg, Pb, Ni, Cu, Mn) have also been synthesized using metal alkyl xanthates in hexadecylamine (HDA).[57] The reaction time, temperature and concentration were used to achieve size and spectroscopic tuneability of the particles. Nair *et al*.[58] also used a Cd(II) complex of dithiobiurea, [$Cd(NH_2CSNHNHCSNH_2)Cl_2$], the precursor was decomposed in tri-n-octylphosphine oxide to give CdS nanoparticles that show quantum confinement effects with characteristic close to band edge luminescence, with narrow size distribution. Trindade and O'Brien have also synthesized PbSe and PbS by using various dithio and diselenocarbamates. Metal complexes of alkylthioureas have also proven to be very good precursors for quantum dot synthesis.[53] A series of Cd(II) complexes with N-alkyl/aryl and N,N'-dialkyl/aryl thioureas have been synthesized by Moloto *et. al*.[59] From studies they performed, they discovered the possibility of nanoparticles giving a mixture of sulphides of two major stoichiometry's, $Cu_{18}S$ and $Cu_{31}S_{16}$.[60] The morphology of the particles they produced was well-defined, triangular and hexagonal in shape. Bruce, Revaprasadu and Koch have been successful in synthesizing Cds and CdSe nanoparticles using bis(N,N-diethyl-N'-benzoyl/seleno thioureato)Cd(II) complexes as precursors.[61] Their nanoparticles were HDA-stabilized and took on a spherical shape. They noted that the selenourea analogue was

somewhat less thermodynamically stable compared to the corresponding acylthiourea analogue over a range of increasing temperature. This, to them was a confirmation of a thermodynamic growth control of CdS and CdSe from these precursors.

More recently, O'Brien *et al.*[62] have used bis(dialkyldithio/diselenocarbamato) cadmium and Zinc (II) compounds as single-molecular precursors in the growth of II-VI thin films by low-pressure and aerosol-assisted CVD. These compounds have been shown to be good precursors for the preparation of nanoparticles, a process that involves their decomposition in a high boiling point coordinating solvent (Lewis base) such as tri-n-octylphosphine oxide (TOPO) or hexadecylamine (HDA), as shown Figure 1.3.

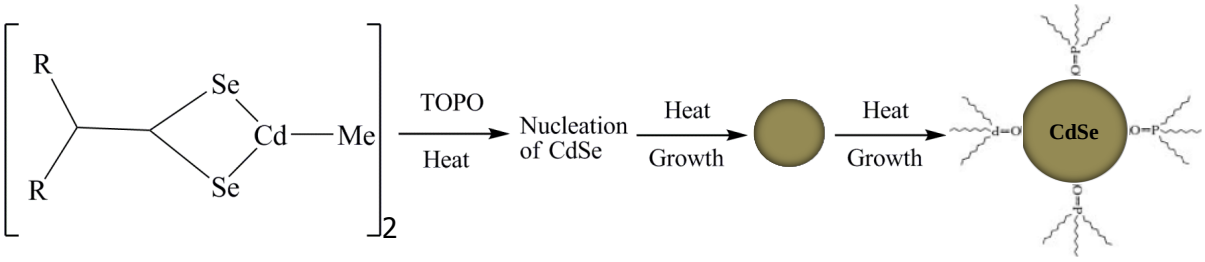


Figure 1.3: A theoretical decomposition schematic for the preparation of TOPO-capped CdSe using a general single-source precursor.

Thiourea and *N,N'*-diethyl-*N'*-acylthiourea complexes of zinc have gained much attention over the years for their potential use as single-source precursors.[56] Their easy preparation and diverse coordination modes to the metal centre make them a very interesting point of study. They have the potential to coordinate to metals through the sulphur atom of the C-S group, the oxygen of the C-O group (acylthioureas) and the nitrogen atom of the N-H groups.[56] Sufficient studies have shown that the coordination proceeds through the oxygen and sulphur atoms and that they are good precursors for the preparation of metal sulphide nanocrystals.[63] Acylthioureas can be described as versatile ligands capable of binding to a wide variety of metal ions in different coordination modes to form stable complexes.[64] The complexing abilities of these ligands are very good since the oxygen, nitrogen, and sulphur donor atoms provide a vast number of bonding possibilities.[65] Acylthioureas can be considered as substituted analogues of β-diketones acting as potential S,O-donor ligands.[66]. Three different coordination modes have been found so far for acylthiourea ligands with transition metal complexes. They may be mono-, di-, or tetra substituted derivatives depending on the extent of the substitution on the nitrogen groups. Specifically, the mono-substituted derivatives may

have are monobasic bidentate or chelating mode (O, S) or neutral bidentate (O, N) modes, which typically proceed with the deprotonation of the N-H in the ligand. Another reported coordination mode is the neutral monodentate coordination which forms through the S donor atom and proceeds without deprotonation.[67] A study conducted by Westra *et al*. shows that the majority of structurally characterized complexes where acylthiourea is the ligand, act as bidentate O, S-monoanionic ligands.[68] The coordination between the acylthiourea derivative and metal ions is reported to proceed through a reaction where the amide group of the ligand is deprotonated during complex formation.[69] In recent years, a variety of metal complexes having thiourea ligands have been prepared and probed as useful intermediates used in environmental control and as ionophores in ion-selective electrodes.[70] New properties and applications for these metal complexes involve interesting luminescent properties[71] and their ability to function as precursors for metal sulphide nanoparticles, among others.[72]

1.2.3.5. Growth Mechanism of nanocrystals

The growing demand to obtain well-passivated nanoparticles of great quality and narrow particle size distribution is met largely by the solution route synthesis of the nanocrystals,[73] due to the ease of implementation and flexibility associated with it. Understanding the coarsening processes that lead to the growth of the minority phase within the majority phase results in a deeper understanding of how the average sizes and size distributions depend on the reaction parameters.[74] In recent times, there has been a renewed interest in understanding the growth process of the solid phase within another solid in aqueous media.

(a) Nucleation

The formation mechanism of nanocrystals in colloidal synthesis is governed by nucleation and growth processes. It has been shown that nucleation is a crucial parameter for determining the size distribution of the particles. Therefore, it is essential that it takes place very quickly. This may be easily achieved in hot injection methods where nucleation occurs immediately after injection of the precursor into the solvent. The nucleation process can either be homogeneous or heterogeneous. In homogeneous nucleation, metal ions are reduced in order to create a critical composition of atomic species. Nucleation begins when the concentration of the atomic species is above a critical level. The process will occur by rapid consumption of the reactants. Subsequent to that growth process will occur on the pre-

existing nuclei. Further nucleation is ceased by a drop in the concentration reactants to below the critical limit as depicted in Figure 1.4.[51]

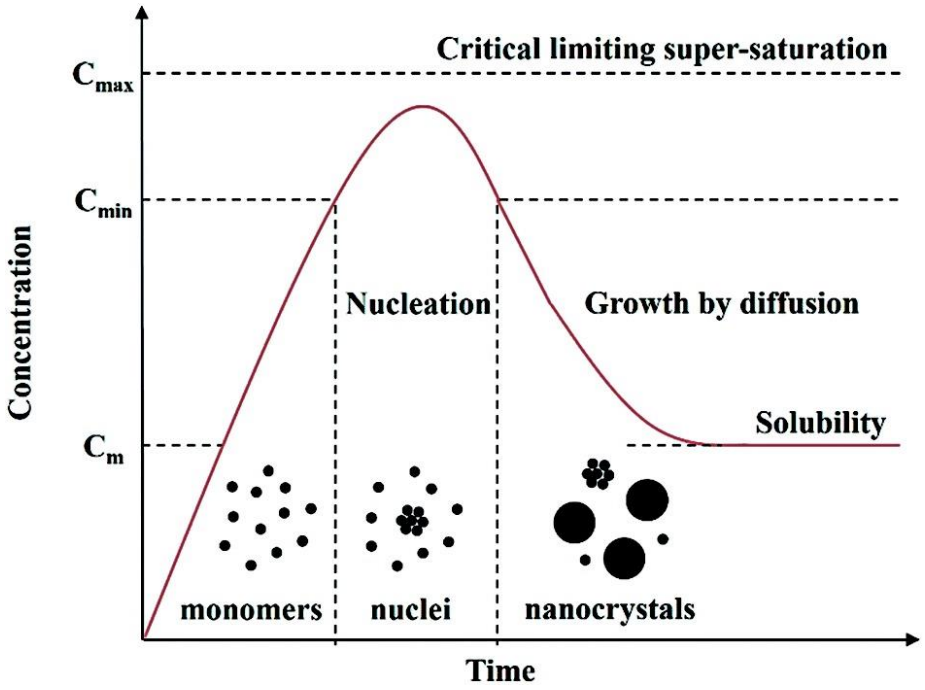


Figure 1.4: A schematic diagram that represents and illustrates La Mer's theory on nucleation.[75]

(b) Growth

Soon after La Mer interpreted the model for nucleation on monodispersed nanoparticles, Reiss developed a growth model known as growth by diffusion.[76] In his model, he suggested that the growth of spherical particles depended on the monomer flux supplied to the particles only. He further explained that if indeed the diffusional growth is only dependant on the monomer flux, smaller particles will grow faster in the presence of larger ones resulting in narrow size distributions of nanocrystals (size focusing). The mechanism was however too simplified as it did not account for effects such as aggregation, coalescence and dissolution (Ostwald's ripening). Sugimoto *et al.*[74]further quantitatively extended Reiss' model by including dissolution effects obtaining a size-dependent growth rate by considering the Gibbs-Thomson equation. Experimentally, Alivasitos and co-workers also deduced a size focusing and defocusing behaviour of the size distribution for the hot injection synthesis of CdSe QDs.[73] In summary, a colloidal particle grows by a sequence of monomer diffusion towards the surface followed by reaction of the monomers at the surface of the nanocrystal. Coarsening effects, controlled either by mass transport or diffusion, are often termed the

Ostwald ripening process. This diffusion limited Ostwald ripening process is the most predominant growth mechanism and was first quantified by Lifshitz and Slyozov.[77]

1.2.4. Size Control of the nanocrystals

To maintain sustainability, future electronic material must deliver desirable optoelectronic properties while containing the abundant and benign elements. In order to maximize their full potential in respective applications, size tuneability is an important character of QDs as properties are largely size dependent. Attempts to control colloidal QDs have been made through optimizing reaction parameters such as the length of the reaction, synthetic temperature, precursor concentration and capping agents employed in the synthesis of QDs.
In optimizing time and temperature, careful monitoring is required for a given synthesis.[78] Many reports have shown that increasing reaction time and temperature results in the growth of nanoparticles sizes as a result of Ostwald's ripening.[79] One such investigation that was performed by Tang *et al*.[80] reported the synthesis of copper indium gallium selenide nanoparticles using hot injection method. The formation of the nanoparticles is made by a rapid injection of precursors in oleylamine at elevated temperatures. However, higher injection temperatures such as 270 °C favored the growth of larger particles. Controlling the concentration of precursors and employing various capping agents has been reported to affect the sizes and shapes of nanoparticles.[81]

1.2.5. Applications in photocatalysis

Heller's early works that focused on the development of semiconductor photoelectrochemistry has assisted tremendously in the development of photocatalysis.[76,82] The use of semiconductor nanocrystals as photosensitizers for the complete degradation of pollutants by oxygen continues to be a growing interest in recent years.[83] Because of their unique electronic structure characterized by a filled valence band (VB) and an empty conduction band (CB), semiconductors are able to make use of the solar energy to break down organic compounds in wastewater. Ideally, an efficient photocatalyst should be stable under air-saturated and water-rich environments as the photocatalytic reactions proceed under these conditions, additionally, the photocatalyst should be able to remain physically and chemically stable after multiple uses.[84] Figure 1.5 shows a visual representation of the mechanism by which photocatalysis follows. When a semiconductor nanocrystal is illuminated by the sun, it absorbs photons with energy equal to or greater than its bandgap;

the electrons in the filled VB are then excited to the empty CB. This excitation of electrons results in the generation of a hole (h^+) in the VB and the electrons (e^-) in the CB.[85]

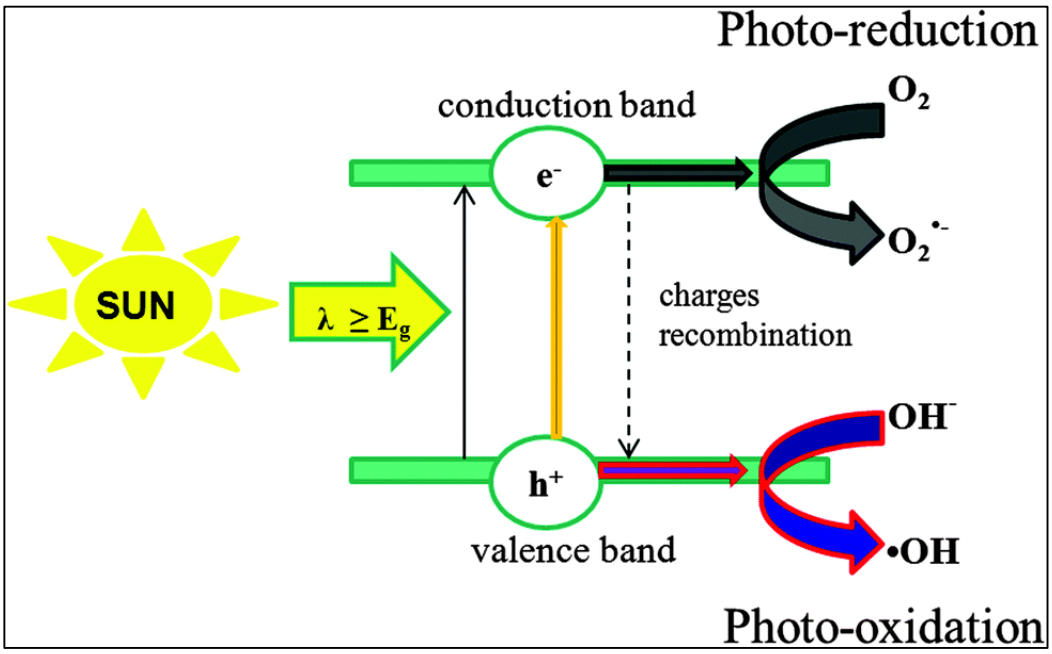


Figure 1.5: **Photocatalytic activation of a semiconductor nanocrystal.**[84]

Upon the formation of the e^-/h^+, a series of reactions take place in order to facilitate the degradation of the pollutant. The hole oxidizes the pollutant directly (Equation 1.2) or ionizes the water to produce hydroxyl radicals, ·OH. (Equation 1.3) These hydroxyl radicals are very reactive and are capable of oxidizing a variety of organic pollutants.[16]

$$h^+ + \text{organic dye} \rightarrow \text{intermediate} \rightarrow CO_2 + H_2O \qquad (1.2)$$

$$h^+ + H_2O \rightarrow OH^- + H^+ \qquad (1.3)$$

The electron excited to the CB reduces the oxygen adsorbed on the photocatalysts to form peroxide radicals followed by a number of steps forming H_2O_2 or •OH radicals thus can prevent the recombination of an electron-hole pair. (Equation 1.4(a) and (b))

$$HOO\cdot + e^- \rightarrow HOO^- \qquad (1.4(a))$$

$$HOO^- + H^+ \rightarrow H_2O_2 \qquad (1.4(b))$$

The •OH attacks organic compounds resulting in various reaction intermediates depending on the nature of the compounds.[13] The resulting intermediates further react with .OH to produce final degradation products such as CO_2 and H_2O. (Equation 1.5)

$$^{\cdot}OH + \text{organic dye} \rightarrow \text{intermediate} \rightarrow CO_2 + H_2O \qquad (1.5)$$

Since the early 1970's, when Fujishima and Honda[86] revealed the possibility of hydrogen production through water decomposition by photocatalysis, TiO_2 has been a subject of growing interest in the academic and industrial fields.[87] In their work, the pair made use of TiO_2 semiconductor photoanode coupled to a Pt cathode. They discovered that TiO_2 possesses powerful oxidation capabilities as it is non-toxic, chemically stable and low-cost making it the most efficient photocatalyst to date. Because TiO2 is a large bandgap material (3.2 eV for the anatase and brookite phases and 3.0 eV for the rutile phase), it requires an excitation wavelength that falls within the ultraviolet region, giving rise to a very low energy efficiency in utilizing solar light.[88] The UV light only accounts for 5% of the sun's energy compared to the visible light (4 %) resulting in applications being limited to absorbing the small fraction of the incident solar irradiation.[18] Due to this limitation, researchers have developed and used several semiconductor photocatalysts that allow easy modification of their bandgaps for applications in the treatment of wastewater pollutants and some of these include ZnO, ZnS, WO_3, SnO_2 and CdS.[13] Wide bandgap materials such as ZnO and ZnS have particularly been of interest due to their small sizes and high optical activity.[9] Similarly, the wide bandgap of ZnO (3.37 eV)[89] and ZnS (3.7 eV)[90] limits light absorption to the UV region, however, possible strategies to extend the photoabsorption of these materials by modifying the valence band positions have been reported to narrow their band gap thereby increasing their photocatalytic activity. Li *et. al.* have reported on the successful doping of ZnO nanoparticles with Mn in order to narrow its bandgap and enhance the performance of the nanoparticles in photocatalysis. Nitrogen doping studies were also performed on ZnS nanoparticles and results showed an increased efficiency of these nanoparticles as photocatalysts.[6] While doping has proven that its capabilities in bandgap narrowing, a simpler more effective way of valence band modification could be to optimize reaction parameters while synthesizing these semiconductor nanoparticles; these parameters could include time of synthesis, reaction temperatures, varying precursor concentration and varying the capping agents used in the nanoparticle synthesis.

1.3. Project motivation

Since the discovery of TiO_2 for photo-electrochemical splitting of water in 1972,[17] great efforts have been directed towards the research of using TiO_2 as a photocatalyst due to its characteristic powerful oxidation capacity, non-toxicity and chemical stability.[6] To date, the TiO_2 photocatalyst has been considered one of the most efficient decontamination technologies amongst available water-treatment plans. Even with its high efficiencies, the use of TiO_2 has shown a number of limitations arising from its narrow photocatalytic region.[18] Some of these limitations include its poor affinity towards hydrophobic organic pollutants resulting in slow photocatalytic degradations. TiO_2 aggregation during photocatalysis has also been observed due to the instability of the nanosized particles, which hamper the light incidence on the active centres and consequently reduce the catalytic activity. In addition, TiO_2 has been shown to have fast recombination times.[19] In order to maximize the utilization of the visible light, several attempts to modify the TiO_2 catalyst have been made.[20,21] Efforts to optimize the synthesis of the catalyst were explored,[22] and an attempt to design and develop the second generation TiO_2 with high separation abilities was attempted.[23] Several countermeasures have been encountered in the process, those of which largely include short-term efficiency of the catalyst, further decreasing the photocatalytic activity and high modification and optimization costs, to mention a few.[18]

In the past two decades, the emergence of nanomaterials as new building blocks in photocatalysis has attracted increasing attention. Wide band-gap nanomaterials such as ZnS (340 nm) have not been studied in detail. Because of their characteristic wide band-gap, these materials can only work under ultra violet light radiation, which accounts for a small part of the solar energy.[9] However, quantum confinement effects in ZnS nanoparticles can result in other advantageous properties such as long excitation lifetime which can minimize recombination. In addition, colloidal synthesis of ZnS can result in capped nanoparticles which can minimize agglomeration, result in small sizes and possibly have an affinity to hydrophobic contaminants.

1.4. Aim and Objectives

The aim of this project was therefore to synthesize and characterize ZnS nanoparticles from $Zn(ATU)_2$ and $Zn(TU)_2Cl_2$ for the photodegradation of rhodamine B.

In order to fulfil the above-mentioned aim, the following objectives were identified:

- Synthesis and characterization of the *N*,*N*-diethyl-*N'*-benzoylthiourea ligand (ATU).
- Synthesis and characterization of the zinc complexes of Acylthiourea and thiourea (TU); $Zn(ATU)_2$ and $Zn(TU)_2Cl_2$.
- Synthesis, characterization and optimization of the zinc nanocrystals from $Zn(ATU)_2$.
- Synthesis, characterization and optimization of the zinc nanocrystals from $Zn(TU)_2Cl_2$.
- Photocatalytic activity testing of the zinc sulfide nanocrystals obtained from both $Zn(ATU)_2$ and $Zn(TU)_2Cl_2$ against Rhodamine B and comparison to the photocatalytic activity of commercial TiO_2 (anatase) and ZnO.

1.5. References

1. Liu, Q., Yu, G. & Liu, J. J. Solar Radiation as Large-Scale Resource for Energy-Short World. *Energy & Environ.* **20,** 319–329 (2009).
2. Postel, S. L. Entering an era of water scarcity: The challenges ahead. *Ecological Applications*, **10,** 941–948 (2000).
3. Mekonnen, M. M. & Hoekstra, A. Y. Four billion people facing severe water scarcity. *Sci. Adv.* **2,** 1–6 (2016).
4. Vörösmarty C. J., Green P., Salisbury J. & Lammers R. B., Global Water Resources: Vulnerability from Climate Change and Population Growth. *Science (80-.).* **289,** 284–288 (2000).
5. Senanayake M., Thirumarpan K. & Thiruchelvam T., Water Pollution: Sources , Effects and Strategies for Prevention in Gampaha District. in *The 7th International Conference on Sustainable Built Environment*, 1–9 (2016).
6. Zegeye, D. Z. Photocatalytic Activity of N-doped ZnS Nanoparticles for Degradation of Organic Pollutant (Methylene Blue). *IJSR*, **5,** 214–219 (2016).
7. Luan M., Jing G., Piao Y., Liu D., Jin L., Treatment of refractory organic pollutants in industrial wastewater by wet air oxidation. *Arab. J. Chem.* **10,** S769–S776 (2017).
8. Zaharia C. & Suteu D., Textile Organic Dyes – Characteristics, Polluting Effects and Separation/Elimination Procedures from Industrial Effluents–A Critical Overview. *Org. Pollut. ten years after Stock. Conv. - Environ. Anal. Updat.* 55–86 (2010).

9. Manoj S., Tarun J., Sukhvir S., Pandeya O.P., Photocatalytic degradation of organic dyes under UV-Visible light using capped ZnS nanoparticles. *Solar Energy,* **86,** 626–633 (2012).
10. Carp O., Huisman C. L. & Reller A. Photoinduced reactivity of titanium dioxide. *Prog. Solid State Chem.* **32,** 33–177 (2004).
11. Vandevivere P. C., Bianchi R. & Verstraete W. Treatment and Reuse of Wastewater from the Textile Wet-Processing Industry. *J. Chem. Technol. Biotechnol.* **72,** 289–302 (1998).
12. Spek A. L. Structure validation in chemical crystallography. *Acta Crystallogr. Sect. D Biol. Crystallogr.* **65,** 148–155 (2009).
13. Herrmann J. Heterogeneous photocatalysis: fundamentals and applications to the removal of various types of aqueous pollutants. *Catal. Today,* **53,** 115–129 (1999).
14. Andreozzi R., Caprio V., Insola I., Marotta R. Advanced oxidation processes (AOP) for water purification and recovery. *Catal. Today* **53,** 51–59 (1999).
15. Zhang H., Chen X., Li X., Kou J., Yu T., Zou Z., Preparation of sensitized ZnS and its photocatalytic activity under visible light irradiation. *J. Phys. D. Appl. Phys.* **40,** 6846–6849 (2007).
16. Herrmann J. M. Heterogeneous photocatalysis: an emerging discipline involving multiphase systems. *Catal. Today* **24,** 157–164 (1995).
17. Mills A. & Le Hunte S. An overview of semiconductor photocatalysis. *J. Photochem. Photobiol. A Chem.* **108,** 1–35 (1997).
18. Dong H., Zeng G., Tang L., Fan C., Zhang C., He X., He Y.. An overview on limitations of TiO_2-based particles for photocatalytic degradation of organic pollutants and the corresponding countermeasures. *Water Res.* **79,** 128–146 (2015).
19. Gao B., Yap P. S., Lim T. M. & Lim T. T. Adsorption-photocatalytic degradation of Acid Red 88 by supported TiO2: Effect of activated carbon support and aqueous anions. *Chem. Eng. J.,* **171,** 1098–1107 (2011).
20. Bannat I., Wessels K., Oekermann T., Rathousky J., Bahnemann D. & Wark M. Improving the Photocatalytic Performance of Mesoporous Titania Films by Modi fication with Gold Nanostructures. *Am. Chem. Soc.* **21,** 1645–1653 (2009).
21. Dong F., Guo S., Wang H., Li X. & Wu Z. Enhancement of the Visible Light Photocatalytic Activity of C-Doped TiO_2 Nanomaterials Prepared by a Green Synthetic Approach. *J. Phys. Chem. C,* **115,** 13285–13292 (2011).
22. Makarova O. V., Rajh T. & Thurnauer M. C. Surface modification of TiO_2

nanoparticles for photochemical reduction of nitrobenzene. *Environ. Sci. Technol.* **34,** 4797–4803 (2000).

23. Nakayama N. & Hayashi T. Preparation and characterization of poly(l-lactic acid)/TiO_2 nanoparticle nanocomposite films with high transparency and efficient photodegradability. *Polym. Degrad. Stab.* **92,** 1255–1264 (2007).
24. Serrano E., Rus G., García-Martínez J., Nanotechnology for sustainable energy. *Renew. Sustain. Energy Rev.* **13,** 2373–2384 (2009).
25. Klimov V. I. Nanocrystal Quantum Dots. *Los Alamos Sci.* 214–220 (2003).
26. Suresh S. Semiconductor Nanomaterials, Methods and Applications: A Review. *Nanosci. Nanotechnol.* **3,** 62–74 (2013).
27. Alivisatos A. P. Semiconductor Clusters, Nanocrytals, and Quantum Dots. *Science.* **271,** 933–937 (1996).
28. Smith A. M & Nie S. Semiconductor Nanocrystals: Structure, Properties, and Band Gap Engineering. *Acc Chem Res.* **43,** 190–200 (2010).
29. Talapin D. V., Rogach A. L., Haase M. & Weller H. Evolution of an ensemble of nanoparticles in a colloidal solution: Theoretical study. *J. Phys. Chem. B* **105,** 12278–12285 (2001).
30. Jorge P., Martins M. A. , Trindade T., Santos J. L. & Farahi F. Optical Fiber Sensing Using Quantum Dots. *Sensors,* **7,** 3489–3534 (2007).
31. Alivisatos A. P. Semiconductor Clusters, nanocrystals and Quantuma dots. *Science.* **271,** 933–937 (1996).
32. Ekimov A. I., Efros A. L. & Onushchenko A. A. Quantum size effect in semiconductor microcrystals. *Solid State Commun.* **56,** 921–924 (1985).
33. Ekimov A. I., Onushchenko A. A. Size quantization of the electron energy spectrum in a microscopic semiconductor crystal. *JETP Lett.* **40,** 337–340 (1984).
34. Henglein, A. Photochemistry of Colloidal Cadium Sulfide and of Colloidal Platinum. *J. Phys. Chem.* **86,** 2291–2293 (1982).
35. Rossetti R., Nakahara S. & Brus L. E. Quantum size effects in the redox potentials, resonance Raman spectra, and electronic spectra of CdS crystallites in aqueous solution. *J. Chem. Phys.* **79,** 1086 (1983).
36. Weller H. Quantized Semiconductor Particles - a Novel State of Matter for Materials Science. *Adv. Mater.* **5,** 88–95 (1993).
37. Trindade T., O'Brien, P. & Pickett N. L. Nanocrystalline semiconductors: Synthesis, properties, and perspectives. *Chemistry of Materials* **13,** 3843–3858 (2001).

38. Kamat P. V. Quantum Dot Solar Cells. Semiconductor Nanocrystals as Light Harvesters. *J. Phys. Chem. C* **112,** 18737–18753 (2008).
39. Luttinger J. M. Quantum Theory of Cyclotron Resonance in Semiconductors: General Theory. *Phys. Rev.* **102,** 1030–1041 (1956).
40. Henglein A. Small-particle research: physicochemical properties of extremely small colloidal metal and semiconductor particles. *Chem. Rev.* **89,** 1861–1873 (1989).
41. Bawendi M. G., Steigerwald M. L. & Brus L. E. The Quantum Mechanics of Larger Semiconductor Clusters ('Quantum Dots'). *Annu. Rev. Phys. Chem.* **41,** 477–496 (1990).
42. Hagfeldt A. & Graetzel M. Light-Induced Redox Reactions in Nanocrystalline Systems. *Chem. Rev.* **95,** 49–68 (1995).
43. Fendler J. H., Fiona C. M The Colloid Chemical Approach to Nanostructured Materials. *Adv. Mater.* **7,** 607–632 (1995).
44. Haug H. & Koch S. W. Quantum Theory of the Optical and Electronic Properties of Semiconductors. *Semiconductors* (2009).
45. Matijevic E. Production of monodispersed colloidal particles. *Annu. Rev. Mater. Sci.* **15,** 483–516 (1985).
46. Daniel M. C. & Astruc D. Gold Nanoparticles: Assembly, Supramolecular Chemistry, Quantum-Size-Related Properties, and Applications Toward Biology, Catalysis, and Nanotechnology. *Chemical Reviews* **104,** 293–346 (2004).
47. Murray C. B., Norris D. J. & Bawendi M. G. Synthesis and Characterization of Nearly Monodisperse CdE (E = S, Se, Te) Semiconductor Nanocrystallites. *J. Am. Chem. Soc.* **19**, 8706–8715 (1993).
48. Abdelhady A. L., Malik M. A. & O'Brien P., Colloidal Synthesis of ZnS, CdS and Zn(x)Cd(1−x)S nanoparticles from zinc and cadmium thiobiuret complexes. *J. Inorg. Organomet. Polym. Mater.* **24,** 226–240 (2014).
49. Green M. & O'Brien P. Recent advances in the preparation of semiconductors as isolated nanometric particles: new routes to quantum dots. *Chemical Communications*, **22**, 2235–2241 (1999).
50. Rossetti R., Hull R., Gibson J. M. & Brus L. E. Hybrid electronic properties between the molecular and solid state limits: lead sulfide and silver halide crystallites. *J.Chem.Phys.* **83,** 1406–1410 (1985).
51. Pickett N. L. & O'Brien P. Syntheses of semiconductor nanoparticles using single-molecular precursors. *Chem. Rec.* **1,** 467–479 (2001).

52. Harlan J. C., Gillan E. G., Bott S. G. & Barron A. R., Tert -Amyl Compounds of Aluminum and Gallium: Halides, Hydroxides, and Chalcogenides. *Organometallics* **15,** 5479–5488 (1996).
53. Revaprasadu N. & Mlondo S. N. Use of metal complexes to synthesize semiconductor nanoparticles. *Pure and Applied Chemistry* **78,** 1691–1702 (2006).
54. Sholin V., Breeze A.J., Anderson I.E., Sahoo Y., Reddy D., Carter S.A., All-inorganic CdSe/PbSe nanoparticle solar cells. *Sol. Energy Mater. Sol. Cells* **92,** 1706–1711 (2008).
55. Trindade T. & O' Brien P. A Single Source Approach to the Synthesis of CdSe Nanocrystallites. *Adv. Mater.* **8,** 161–163 (1996).
56. Moloto N., Revaprasadu N., Moloto M.J., O'Brien P. & Helliwel M. N,N'-Diisopropyl- and N,N'-dicyclohexylthiourea cadmium(II) complexes as precursors for the synthesis of CdS nanoparticles. *Polyhedron* **26,** 3947–3955 (2007).
57. Pradhan N., Katz B. & Efrima S. Synthesis of High-Quality Metal Sulfide Nanoparticles from Alkyl Xanthate Single Precursors in Alkylamine Solvents. *J. Phys. Chem. B* **107,** 13843–13854 (2003).
58. Nair P. S., Radhakrishnan T., Revaprasadu N., Kolawole A. & O' Brien P. A single-source route to CdS nanorods. *Chem. Commun.* 564–565 (2002).
59. Moloto M. J., Malik M. A., O'Brien P., Motevalli M. & Kolawole G. A. Synthesis and characterization of some N-alkyl/aryl and N,N'- dialkyl/aryl thiourea cadmium(II) complexes. *Polyhedron* **22,** 595–603 (2003).
60. Moloto M. J., Revaprasadu N., Kolawole G. A., O'Brien P. & Malik, M. A. The synthesis and characterization of Cu_xS_y and PbS nanoparticles from alkylthiourea lead and copper complexes. *S. Afr. J. Sci.* **101,** 463–465 (2005).
61. Bruce J. C., Revaprasadu N. & Koch K. R. Cadmium(II) complexes of N,N-diethyl-N′-benzoylthio(seleno)urea as single-source precursors for the preparation of CdS and CdSe nanoparticles. *New J. Chem.* **31,** 1647 (2007).
62. O'Brien P., Walsh J. R., Watson I. M., Motevalli M. and Henriksen L. Molecule Precursors for Low-Pressure Metal-Organic Chemical Vapour Deposition. *J. Chem. Soc., Dalt. Trans.* 2491–2496 (1996).
63. Moloto M. J., Revaprasadu N., O'Brien P. & Malik M. A. N-alkylthioureacadmium (II) complexes as novel precursors for the synthesis of CdS nanoparticles. *J. Mater. Sci. Mater. Electron.* **15,** 313–316 (2004).
64. Nakada T. Optical absorption and dispersion in rf-sputtered alpha-HgS films. *J. Appl.*

Phys. **46,** 4857–4861 (1975).

65. Wang Y. & Herron N. Nanometer-sized semiconductor clusters: materials synthesis, quantum size effects, and photophysical properties. *J. Phys. Chem.* **95,** 525–532 (1991).
66. Edelman F., Hahn H., Seifried S., Alof C., Hoche H., Balogh A., Werner P., Zakrzewska K.,Radecka M., Pasierb P., Chack A., Mikhelashvili V. & Eisenstein G., Structural evolution of SnO_2/TiO_2 nanocrystalline films for gas sensors. *Mater. Sci. Eng. B* **69–70,** 386–391 (2000).
67. Ahmad S., Isab A. A. & Arnold A. P. Synthesis and Spectroscopic Characterization of Silver(I) Complexes of Selenones. *J. Coord. Chem.* **56,** 539–544 (2003).
68. Westra A. N., Bourne S. & Koch, K. R. First metallamacrocyclic complexes of Pt(iv) with 3,3,3',3'-tetraalkyl-1,1'-phenylenedicarbonylbis(thioureas): synthesis by direct or electrolytic oxidative addition of I_2, Br_2 and Cl_2. *Dalton Trans.* **3,** 2916–2924 (2005).
69. Moloton N., Revaprasadu N., Moloto M. J., O' Brien P. & Raftery J. N,N'-diisopropylthiourea and N,N'-dicyclohexyl- thiourea zinc (II) complexes as precursors for the synthesis of ZnS nanoparticles. *S. Afr. J. Sci.* **105,** 258–263 (2009).
70. Wilson D., Ángeles M. D. L. & Alegret S. Lead (II) ion selective electrodes with PVC membranes based on two bis-thioureas as ionophores : 1,3-bis (N -benzoylthioureido) benzene and 1,3-bis (N-furoylthioureido) benzene. *J. Hazard. Mater.* **181,** 140–146 (2010).
71. Semeniuc R. F., Reamern T. J., Blitz J. P., Wheeler K. A. and Smith M. D. Functionalized O-Alkyldithiocarbonates :A New Class of Ligands Designed for Luminescent Heterometallic Materials. *Am. Chem. Soc.* **6**, 2624–2629 (2010).
72. Afzaal M., Malik M. A. & O' Brien P. Chemical routes to chalcogenide materials as thin films or particles with critical dimensions with the order of nanometres. *J. Mater. Chem.* **20**, 4031-4040 (2010).
73. Peng X., Wickham J. & Alivisatos A. P. Kinetics of II-VI and III-V colloidal semiconductor nanocrystal growth: "focusing" of size distributions . *J. Am. Chem. Soc.* **120,** 5343–5344 (1998).
74. Viswanatha R. & Sarma D. D. Growth of Nanocrystals in Solution. Nanomaterials Chemistry: Recent Developments and New Directions (2007).
75. Chang J. & Waclawik E. R. Colloidal semiconductor nanocrystals: controlled synthesis and surface chemistry in organic media. *RSC Adv.* **4,** 23505–23527 (2014).
76. Reiss H. The growth of uniform colloidal dispersions. *J. Chem. Phys.* **19,** 482–489

(1951).

77. Niethammer B. Effective Theories for Ostwald Ripening. *Anal. Stochastics Growth Process. Interface Model.* 1–21 (2008).
78. Kim K., Johnson E. V., Kazanskii A. G., Khenkin M. V. & Cabarrocas P. R, Unravelling a simple method for the low temperature synthesis of silicon nanocrystals and monolithic nanocrystalline thin films. *Sci. Rep.* **7,** 1–11 (2017).
79. Liu B. & Zeng H. C. Symmetric and asymmetric ostwald ripening in the fabrication of homogeneous core-shell semiconductors. *Inorg. nanostructures* **1,** 566–571 (2005).
80. Tang J., Hinds S., Kelley S. O. & Sargent E. H. Synthesis of Colloidal $CuGaSe_2$, $CuInSe_2$, and $Cu(InGa)Se_2$ Nanoparticles. *Chem. Mater.* **20,** 6906–6910 (2008).
81. S. Govindraju, M.P. Kalenga, M. Airo, M.J. Moloto, L.M. Sikhwivhilu, N. M. Size quantization in Cu2Se nanocrystals. *Opt. Mater. (Amst).* **38,** 310–313 (2014).
82. Fujishima A., Rao T. N. & Tryk D. A. Titanium dioxide photocatalysis. *J. Photochem. Photobiol. C Photochem. Rev.* **1,** 1–21 (2000).
83. Kutal C. & Athens G. Photochemical conversion and storage of solar energy. *J. Chem. Educ.* **60,** 882–887 (1983).
84. Kumar S. G. & Devi L. G. Review on modified TiO_2 photocatalysis under UV/visible light:Selected results and related mechanisms on interfacial charge carrier transfer dynamics. *J. Phys. Chem. A* **115,** 13211–13241 (2011).
85. Mills A., Davies R. H. & Worsley D. Water purification by semiconductor photocatalysis. *Chem. Soc. Rev.* **22,** 417 (1993).
86. Fujishima A. & Honda K. Electrochemical Evidence for the Mechanism of the Primary State of Photosynthesis. *Bulletin of the Chemical Society of Japan* **44,** 1148–1150 (1971).
87. Lee S. Y. & Park S. J. TiO_2 photocatalyst for water treatment applications. *J. Ind. Eng. Chem.* **19,** 1761–1769 (2013).
88. Yin S., Zhang Q., Saito F. & Sato T. Preparation of Visible Light-Activated Titania Photocatalyst by Mechanochemical Method. *Chem. Lett.* **32,** 358–359 (2003).
89. Li J. H., Shen D. Z., Zhang J. Y., Zhao D. X., Li S., Lu B. & Liu Y. M. The effect of Mn^{2+} doping on structure and photoluminescence of ZnO nanofilms synthesized by sol-gel method. *J. Lumin.* **122–123,** 352–354 (2007).
90. Lippens P. E. & Lannoo M. Calculation of the band gap for small CdS and ZnS crystallites. *Phys. Rev. B* **39,** 10935–10942 (1989).

Chapter 2: Synthesis and characterisation of N, N-diethyl-N'-acylthiourea and thiourea zinc complexes

2.1. Introduction

Thioureas and *N,N*-diethyl-*N'*-acylthiourea derivatives are interesting as single-source precursors for semiconductor nanocrystals as they possess various potential donor sites.[1] The presence of the oxygen, sulphur and nitrogen donor atoms of the multiple site reactive systems provides a wide range of bonding possibilities,[2] consequently, resulting in the possibility of forming either metal chalcogenide or a mixture. The acidic amide of the acylthiourea ligand exposes the oxygen and sulphur donor atoms of the ligand resulting in the ligand acting as a bidentate O-S-monoanionic ligands.[3] Although rare, coordination through sulphur only has previously been observed in a few transition metal complexes.[4] The monodentate coordination is stabilized by an intramolecular hydrogen bond formation between the carbonyl atom and the NH group.

Cadmium complexes of thiourea and N-alkylthioureas have been used as precursors for the preparation of cadmium sulphide nanocrystals.[5,6] Studies showed that the alkyl substituted thiourea cadmium complexes were very easy to prepare and air-stable for long periods of time, which poses an economical and environmental advantage over previous methods that have been used to synthesis semiconductor nanocrystals. Zinc (II) complexes of N,N'-diisopropylthiourea and N,N'-dicyclohexylthiourea have also been found to be effective as precursors for the preparation of hexadecylamine-capped ZnS nanoparticles.[1] Similarly, the complexes were air-stable, easy to prepare and inexpensive. They were also reported to pyrolyse cleanly to give high-quality ZnS nanoparticles. This chapter reports on the synthesis and characterization of the thiourea (TU) and *N,N*-diethyl-*N'*-acylthiourea (ATU) complexes of zinc (II). The thiourea and acylthiourea derivatives were varied to study the effect of the electronic properties of the complexes and the quality of the resulting nanoparticles. Thiourea has previously been used for the synthesis of zinc sulphide nanoparticles, however, to our knowledge, no work has been reported on the thermolysis of the *N,N*-diethyl-*N'*-acylthiourea complexes of zinc (II). *N,N*-diethyl-*N'*-acylthiourea complexes consist of both the Zn-S and Zn-O bonds within the complex, which raises the questions of whether formation of one type

of material over the other can be tuned or if both chalcogenide and oxide form, can the two be separated, or is it possible to form core-shell structures? The aim of this chapter was to therefore synthesize thiourea and *N,N*-diethyl-*N'*-acylthiourea complexes of zinc (II), for use as single-source precursors for the synthesis of ZnS semiconductor nanocrystals.

2.2. Experimental

2.2.1. Instrumentation

^{1}H NMR and 2D NMR experiments were done using a Bruker Avance 500 MHz spectrometer. Infrared spectra were recorded on FT-IR Bruker spectrophotometer using ATR. Melting points were determined using an Electrothermal IA9300 Digital Melting Point Apparatus. CHNS elemental microanalysis was performed on a Flash 2000 CHNS-O Analyzer fitted with an Auto sampler. Mass spectrometry was obtained using a Advion Expression L compact mass spectrometer. Single-crystal intensity data were collected at -100 °C on a Bruker APEX II CCD area detector diffractometer with graphite monochromated Mo K_α radiation (50kV, 30mA). The collection method involved ω-scans of width 0.5 ° and 512 x 512 bit data frames. The crystal structures were solved by direct methods. Non-hydrogen atoms were first refined isotropically followed by anisotropic refinement by full matrix least-squares calculations based on F^2. Hydrogen atoms were first located in the difference map then positioned geometrically and allowed to ride on their respective parent atoms. Software used in this work were as follows: Data collection: *APEX2*[7]; cell refinement and data reduction: *SAINT*; program used to solve and refine structures: *SHELX-2014*;[8] software used to prepare material for publication: *WinGX-2014.1*[9] and *PLATON*.[10]

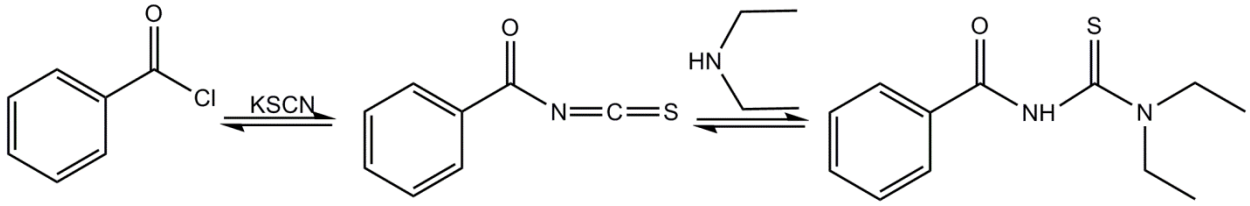
2.2.2. Reagents

Ethanol, acetone and methanol were obtained from Kemical. Zinc chloride, thiourea, potassium thiocyanate, benzoyl chloride, acetone and ethanol (analytical grade) obtained from Aldrich, were used as purchased to prepare the precursors.

2.2.3. Synthesis of the *N,N*-diethyl-*N*'-benzoylthiourea ligand

The *N,N*-diethyl-*N'*-acylthiourea (ATU) ligand was prepared according to the general procedure described by Douglass and Dains,[11] as shown in Scheme 2.1. The method involved a one-pot procedure where benzoyl chloride (3.50 mL) was added to a solution of anhydrous acetone (50 mL) containing potassium thiocyanate (2.9332 g, 0.0302 mol). The

mixture was stirred under reflux for 60 min and cooled to room temperature. Diethylamine (3.12 mL) was added to the reaction mixture and stirred for a further 2 h. The final mixtures were poured into a beaker of cold water to form crystals of the acylated thiourea in good yields. The crystals were filtered, washed with water and then air dried.

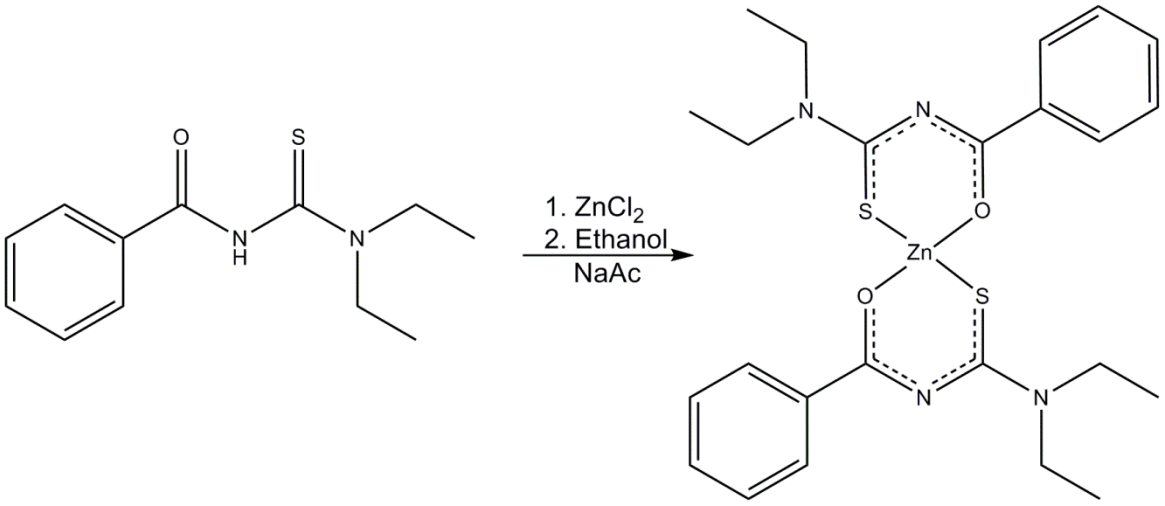


Scheme 2.1: Schematic diagram showing the general procedure of the formation of the ATU ligand

Yield: 4.9587 g, 70 %, m.p., 99 – 99.3 °C. FTIR (ATR)/cm^{-1}: 3288.15(N-H), 2779.88(C-H), 1647(C=O). ^{1}H NMR (δ, $CDCl_3$) ppm: 8.32 (s, 1H, N-H), 7.84 (d, 2H, H^1), 7.48 (t, 1H, H^3), 7.40 (t, 2H, H^2), 4.03 (d, 2H, H^4), 3.61 (d, 2H, $H^{4'}$), 1.37 (t, 3H, H^5), 1.30 (t, 3H, $H^{5'}$). Elemental analysis calcd. (%) for $C_{12}H_{16}N_2OS$: C, 60.99; H, 6.82; N, 11.85; S, 13.57. Found (%): C, 60.52; H, 6.32; N, 11.24; S, 12.77.

2.2.4. Synthesis of the Bis(N,N-diethyl-N'-benzoylthiourea) Zinc (II) complex

Bis(*N*,*N*-diethyl-*N'*-benzoylthiourea) Zinc (II) was prepared according to the modified method highlighted in Scheme 2.2 obtained from Moloto *et al.*[12]. The ATU ligand (2.5057 g, 0.01060 mol) and sodium acetate (0.8543 g, 0.01041 mol) were dissolved in minimum ethanol (10 mL) and left to stir for 10 minutes at room temperature. A solution of zinc chloride (0.7389 g, 0.005421 mol) in ethanol (5 mL) was added to the ligand solution and left to stir for 24 h under reflux. The reaction was monitored using thin layer chromatography. The solvent was removed by gravity filtration to yield a white precipitate which was dried and recrystallized from ethanol by slow evaporation.



Scheme 2.2: A schematic diagram displaying the synthesis of the $Zn(ATU)_2$ complex

Yield: 2.6965 g, 92.80 %, m.p. 135-141 ˚C. FTIR (ATR)/cm^{-1}: 2999.17(C-H), 1517.91 (C-O). ^{1}H NMR (δ, $CDCl_3$) ppm: 8.19 (d, 4H, H^1), 7.57 (t, 2H, H^3), 7.35 (t, 4H, H^2), 3.95 (q, 4H, H^4), 3.88 (q, 4H, $H^{4'}$), 1.35 (t, 6H, H^5), 1.30 (t, 6H, $H^{5'}$). ^{13}C NMR (δ, $CDCl_3$) ppm: 131.40 (s, 1C, C^3), 129.49 (s, 2C, C^1), 127.78 (s, 2C, $C^{2'}$), 45.99 (s, 1C, $C^{4'}$), 45.83 (s, 1C, C^4), 13.25 (s, 1C, $C^{5'}$), 12.78 (s, C, C^5). Elemental analysis calcd. (%) for $C_{24}H_{30}N_4O_2S_2Zn$: C, 53.77; H, 5.64; N, 10.45; S, 11.96. Found (%): C, 53.48; H 5.50; N, 9.94; S, 11.25. ESI^+ [M^+]: 536.02 M/z

2.2.5. Synthesis of Bis(diaminomethylthio) Zinc(II) Chloride

The Bis(diaminomethylthio) Zinc(II) Chloride complex was synthesized using high purity grade zinc chloride and thiourea according to a procedure obtained from Rajasekaran *et. al.*[13] In a typical synthesis, $ZnCl_2$ (0.4491 g, 0.007037 mol) was dissolved in minimum distilled water (5 ml) while thiourea (1 .0418 g, 0.01369 mol) was separately dissolved in minimum distilled water (5 ml) as well. The zinc chloride solution was added to the thiourea solution drop wise and refluxed for 3 hours. The reaction was monitored using thin layer chromatography and terminated upon completion. The hot solution was filtered to get rid of unreacted materials and left overnight to crystallize. The crystals were filtered, dried and characterized by CHNS analysis, FTIR spectroscopy, ^{13}C NMR spectroscopy, single crystal X-Ray crystallography and mass spectrometry to confirm synthesis.

Yield: 1.9342 g, 95.2 %, m.p. 154.8 – 155.1 °C. FTIR (ATR)/cm^{-1}: 2999.17(C-H), 1517.91 (C-O). ^{13}C NMR (δ, 183.85 (s, 1C, HL^1), 182.65 (s, 1C, $Zn(TU)_2Cl_2$), Elemental analysis

calcd. (%) for $C_2H_8Cl_2N_4S_2Zn$: C, 8.32; H, 2.79; N, 19.42; S, 22.22. Found (%): C, 8.02; H, 2.63; N, 18.8; S, 21.26. ESI+ [M+]:: 288.56 m/z

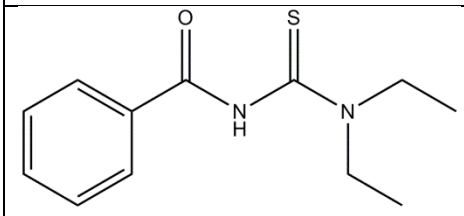
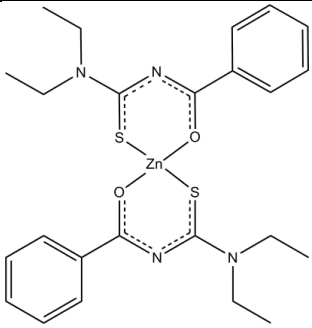
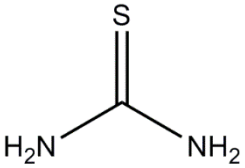
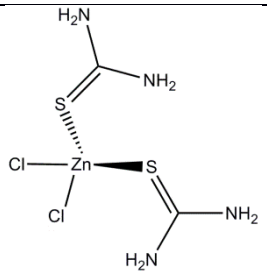
2.3. Results and discussion

General synthesis steps that will be discussed in the following chapter:

a) Synthesis of the *N*,*N*-diethyl-*N'*-benzoylthiourea ligand
b) Synthesis of the Bis(*N*,*N*-diethyl-*N'*-benzoylthiourea) Zinc (II) complex
c) Synthesis of the Bis(diaminomethylthio) Zinc(II) chloride

For ease of reference, Table 2.1 summarizes the complexes synthesized and their respective ligands.

Table 2.1: Ligands and complexes synthesized with full and abbreviated names

Ligand name	abbreviation	Complex name	abbreviation
 *N*,*N*-diethyl-*N'*-benzoylthiourea	ATU	 Bis(*N*,*N*-diethyl-*N'*-benzoylthiourea) Zinc (II)	Zn(ATU)
 Thiourea	TU	 Bis(diaminomethylthio) Zinc(II) Chloride	$Zn(TU)_2Cl_2$

2.3.1. Characterization of the ATU ligand

Figure 2.1 displays the ^{1}H NMR spectrum of the ATU ligand. The ^{1}H NMR spectrum of the ligand was assigned using assignments based on literature[14] and confirmed using COSY

(Appendix A Figure 1), ^{13}C NMR (Appendix A, Figure 2) and HSQC (Appendix A Figure 3) experiments. The ^{1}H NMR spectrum of the ligand displayed an intense singlet at 8.32 ppm, which was assigned to the NH proton. In the aromatic region, protons were observed at 7.84 ppm, 7.48 ppm and 7.40 ppm. The proton at 7.84 ppm was a doublet that integrated for two protons and was assigned to H^1, the proton observed at 7.48 ppm was a triplet that integrated for one proton and was assigned to H^3, and finally, the proton observed at 7.40 ppm was a triplet that integrated for 2 protons and was assigned to H^2.

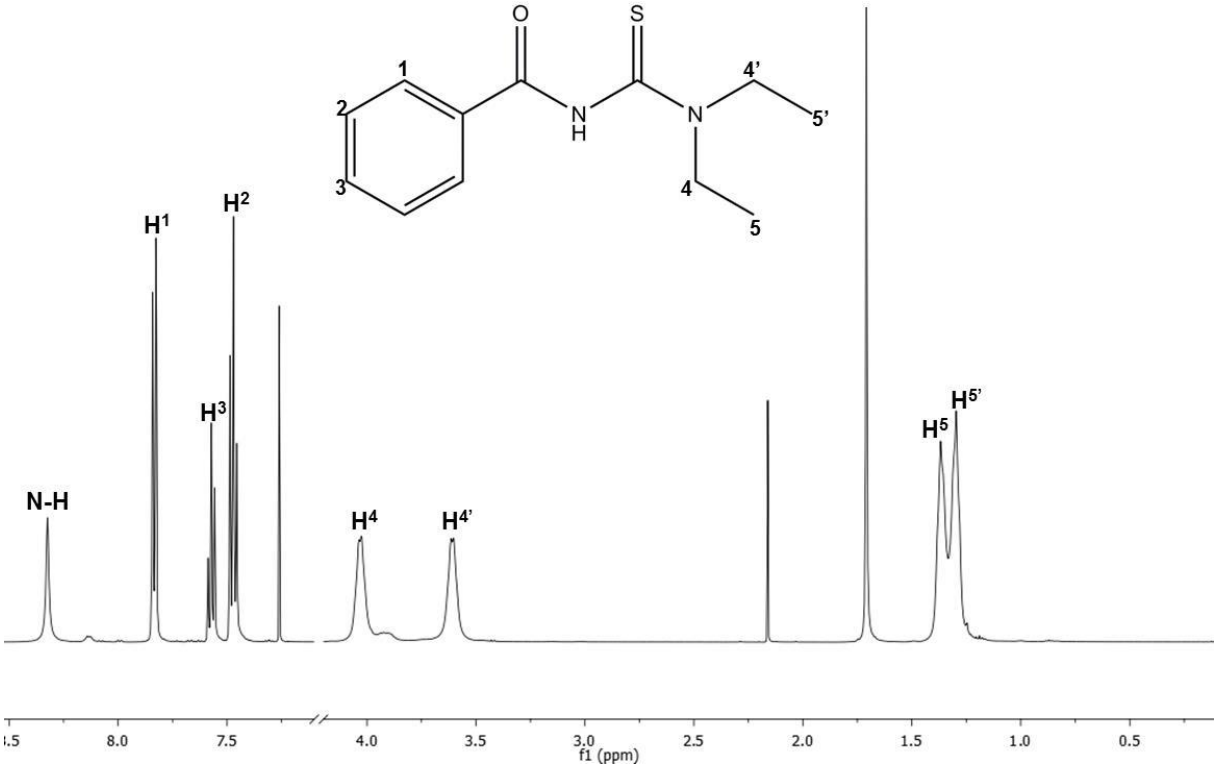


Figure 2.1: ^{1}H NMR spectrum of the ATU ligand in $CDCl_3$ at 300 K. (*Please note break between 4.2 ppm and 7.1 ppm*)

The two unresolved peaks observed at 4.03 ppm ad 3.61 ppm integrated for two protons each and were assigned to H^4 and $H^{4'}$, respectively. The protons corresponded to the CH_2 groups near the N atom. H^4 was assigned to the most deshielded CH_2 group as it was trans to the N atom. The protons observed at 1.37 ppm and 1.30 ppm was due to the CH_3's and was assigned using COSY (Appendix A, Figure 1). The protons at 1.37 ppm intersected with H^4 and the protons at 1.30 ppm intersected with $H^{4'}$ which facilitated the assignment of H^5 and $H^{5'}$, respectively.

2.3.2. Characterization of $Zn(ATU)_2$ complex

FT-IR spectroscopy was used to characterize and confirm the synthesized complex. FTIR spectra of the free ligand and the complex are shown in Figure 2.2. The ATU ligand gave rise to two characteristic bands in its FTIR spectrum which included the υ(N-H) stretching bands of the secondary amine which was observed at 3461 cm^{-1} and the prominent υ(C=O) stretching of the carbonyl moiety at 1598 cm^{-1}. Complex formation lead to the loss of the N-H proton resulting in the disappearance of the υ(N-H) stretching mode and a shift of the υ(C=O) stretching to lower wavenumbers. This behavior is expected as a result of a decrease in the double bond character of these groups. The thiocarbonyl υ(C=S) stretching mode should also display the shift to lower wavenumbers,[15] but we cannot identify this shift easily as this bond also falls within the finger print region (wavenumbers below 1500 cm^{-1}). The bands seen at the center of 2987 cm^{-1} which can be attributed to the υ(C-H) stretching frequency display no shift, which is in line with literature. [16]

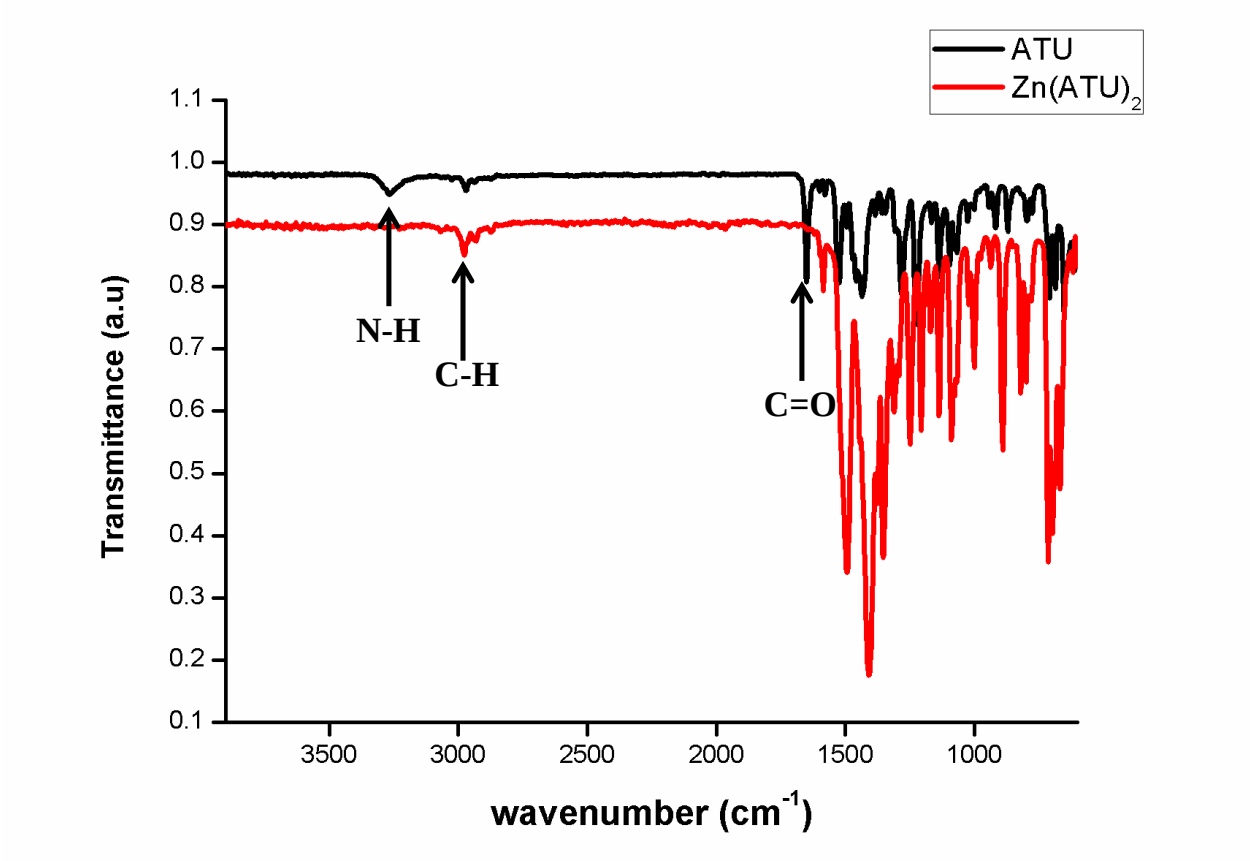


Figure 2.2: Infrared spectrum of a) ATU (black) and b) $Zn(ATU)_2$ (red).

In addition to the FT-IR spectral analysis, $Zn(ATU)_2$ was further characterized using NMR spectroscopy. The ^1H NMR spectrum of the complex is shown in Figure 2.3. The assignment

of the ^{1}H NMR of the metal complex was fairly straight forward as the ligand had already been assigned. $Zn(ATU)_2$ is a tetrahedral complex, only one half of the complex is accounted for as the protons from the other half should be in exactly the same position due to a similar chemical environment. In the ^{1}H NMR of the complex, a signal observed in the ligand at 8.32 ppm disappears, which was initially assigned to the proton from the N-H. This confirmed the deprotonation of the ligand to form the complex. The doublet observed at 8.19 ppm integrated for 4 protons and was assigned to H^1, the triplet observed at 7.57 ppm integrated for two protons and was assigned to H^3 and the triplet observed at 7.35 ppm integrated for 4 protons and was assigned H^2.

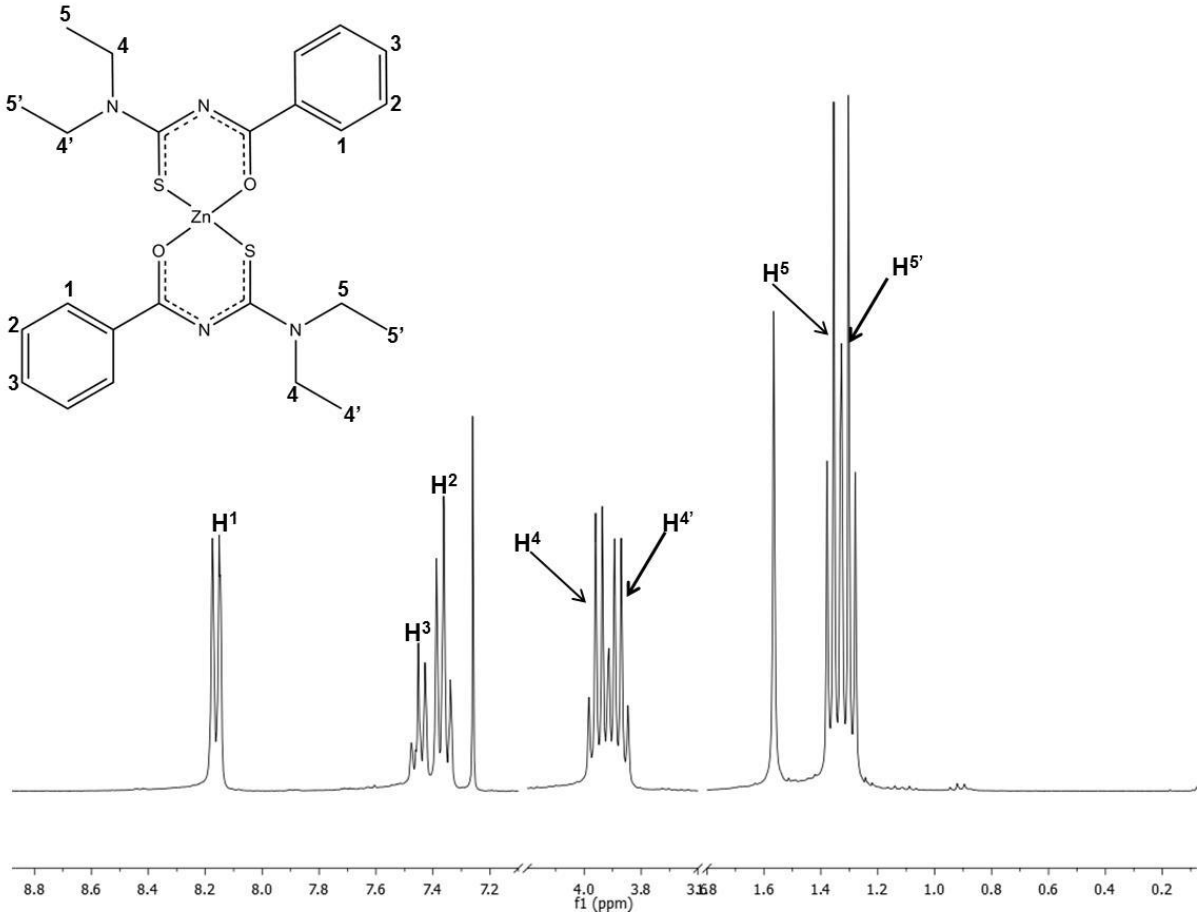
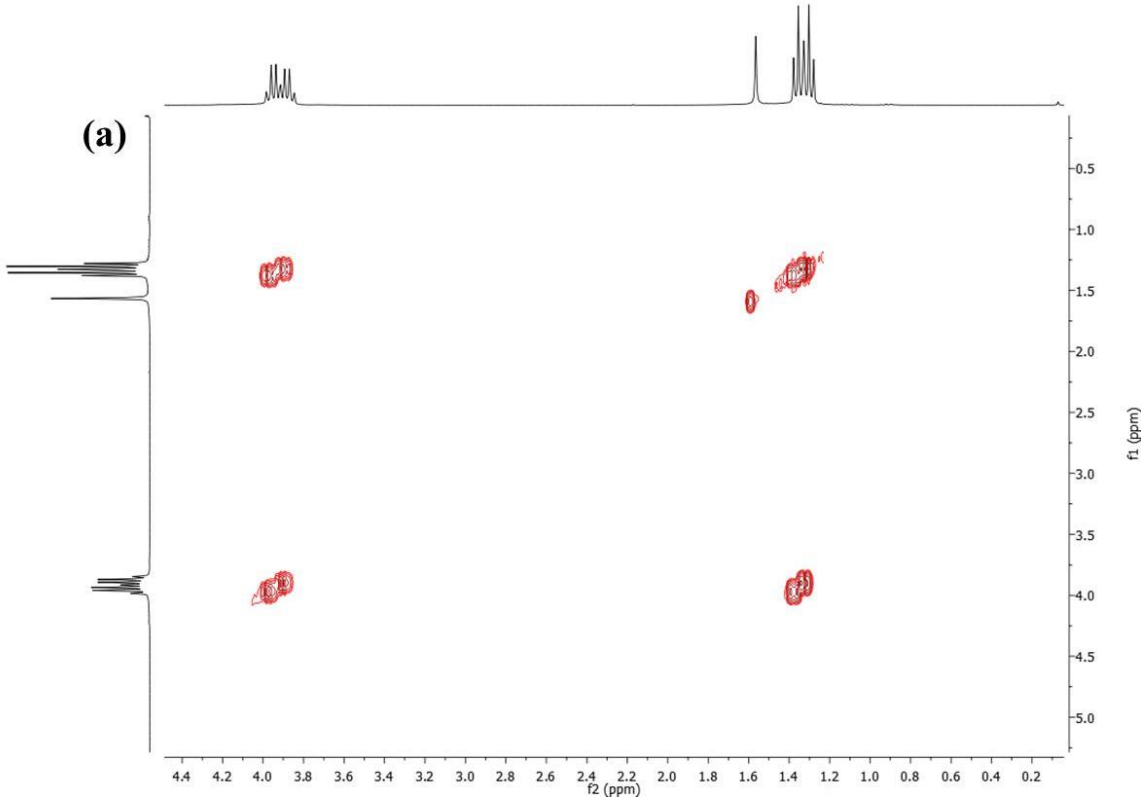


Figure 2.3: 1H NMR spectrum of the $Zn(ATU)_2$ complex in $CDCl_3$ at 300 K. (Please note breaks between 4.2 ppm and 7.1 ppm also between 1.8 ppm and 3.6 ppm)

The previously unresolved peaks observed in the region between 4.03 ppm and 3.61 ppm shifted to multiplets at 3.95 ppm and 3.88 ppm and were assigned H^4 and $H^{4'}$, respectively. The peaks were due to the CH_2 group nearer to the N atom and the shift was likely caused by

the lack of sufficient rotational freedom about the N-C bond due to the nitrogen lone pair and the delocalized electrons in the complex as compared to the previous intact thiocarbonyl bond. As was in the ligand, the CH_2 group trans to the electron withdrawing N group was the most de-shielded. The free rotation induced upon complexation also affected the methyl (CH_3's) protons which were shifted to 1.35 and 1.30 ppm. The two triplets at 1.35 ppm and 1.30 ppm integrated for 6 protons each and were assigned using COSY.(Figure 2.4) In the COSY, the triplet at 1.35 coupled to H^4, facilitating the assignment of H^5 and the proton at 1.30 coupled to $H^{4'}$, which enabled the assignment of $H^{5'}$.



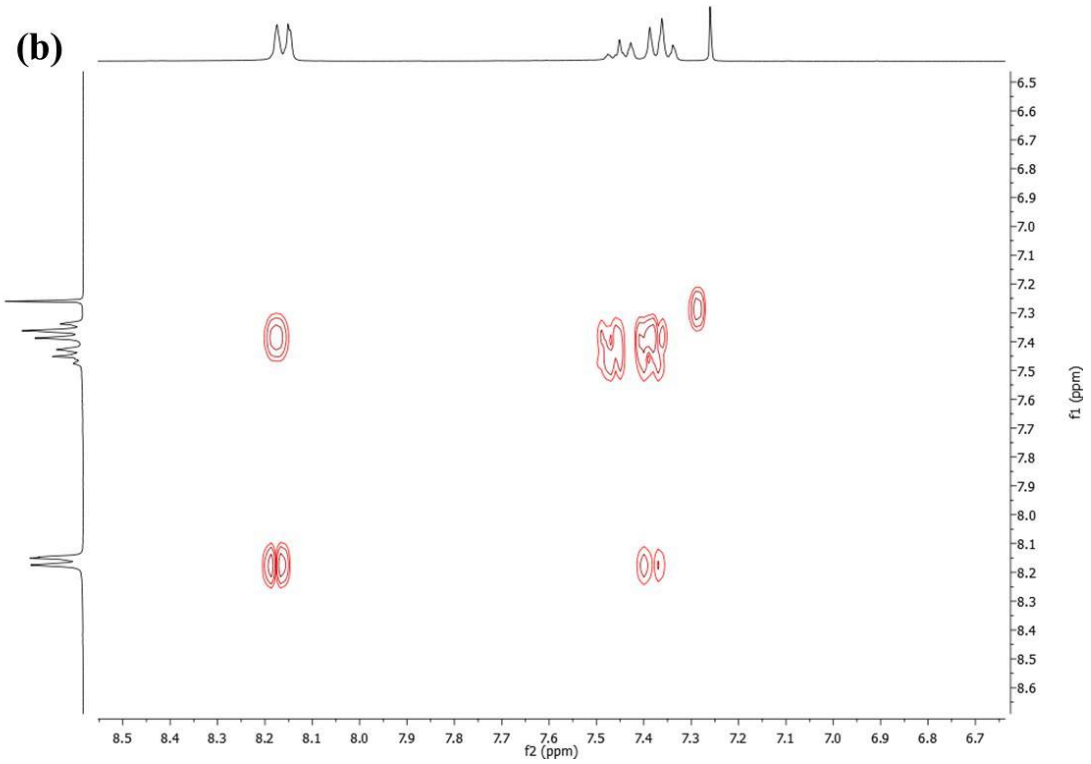


Figure 2.4: $^{1}H,^{1}H$ COSY spectra of Zn(ATU)2 in $CDCl_3$ at 300 K where (a) is the aliphatic region and (b) is the aromatic region.

So far, the assumption is that the protons from the aliphatic regions are H^4 and $H^{4'}$ for the CH_2 protons, and those from the CH_3 groups have been assigned H^5 and $H^{5'}$. Figures 2.5(a) and (b) are enlarged spectra of HSQC spectrum of the $Zn(ATU)_2$ where (a) is the aliphatic region and (b) is the aromatic region. The HSQC was used to assign the ^{13}C NMR. From Figure 2.5(a), it is clear that the proton at 3.95 ppm (H^4), couples to the proton at 1.35 ppm (H^5); similarly, the proton at 3.88 ppm ($H^{4'}$), couples to the one at 1.30 ppm ($H^{5'}$). The aromatic protons have been carefully assigned as well. Figure 2.5(b) shows us that the H^1 protons at 8.19 ppm couple to protons at 7.57 ppm (H^2). The proton at 7.35 ppm couples to proton H^2.

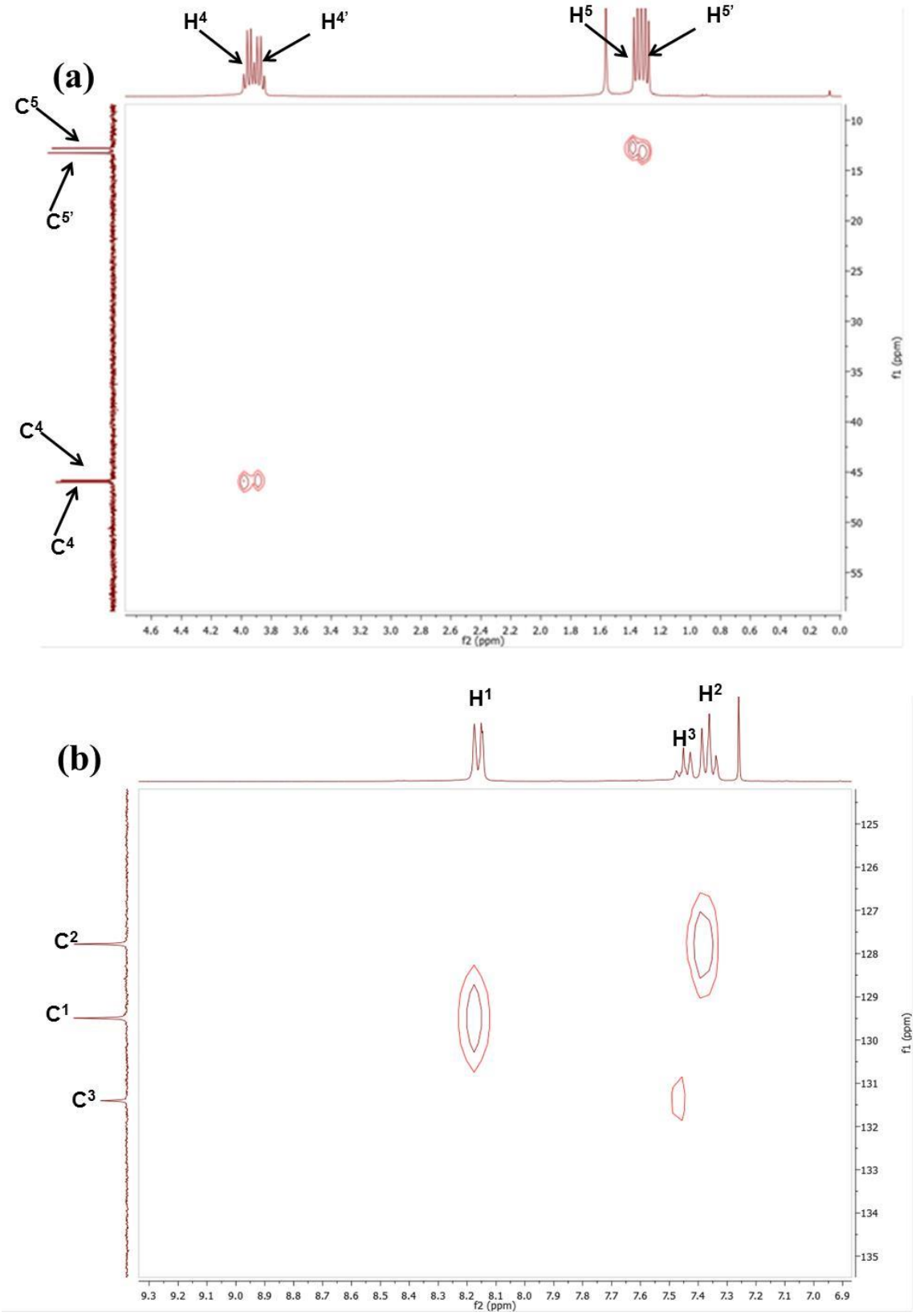


Figure 2.5: ^{1}H, ^{13}C HSQC spectra of $Zn(ATU)_2$ in $CDCl_3$ where (a) is the aliphatic region and (b) is the aromatic region.

From Figure 2.5 (a), it is evident that protons H^4 and $H^{4'}$ correlate to the carbons at 45.99 and 45.83 ppm, hence assigned to C^4 and $C^{4'}$, respectively. Consequently, protons H^5 and $H^{5'}$ correlate to carbons C^5 and $C^{5'}$ at 13.25 and 12.78 ppm. Protons H^1 are correlated to the carbons centred at 129.49 ppm, thus the assignment of C^1. Protons H^2 correlate to the carbons centred at 127.78 ppm, and to this we assign C^2. Consequently, H^3 correlates to the carbon at 131.40 ppm, thus C^3. The successful assignment of the HSQC NMR enabled the assignment of the ^{13}C NMR as seen in Figure 2.6.

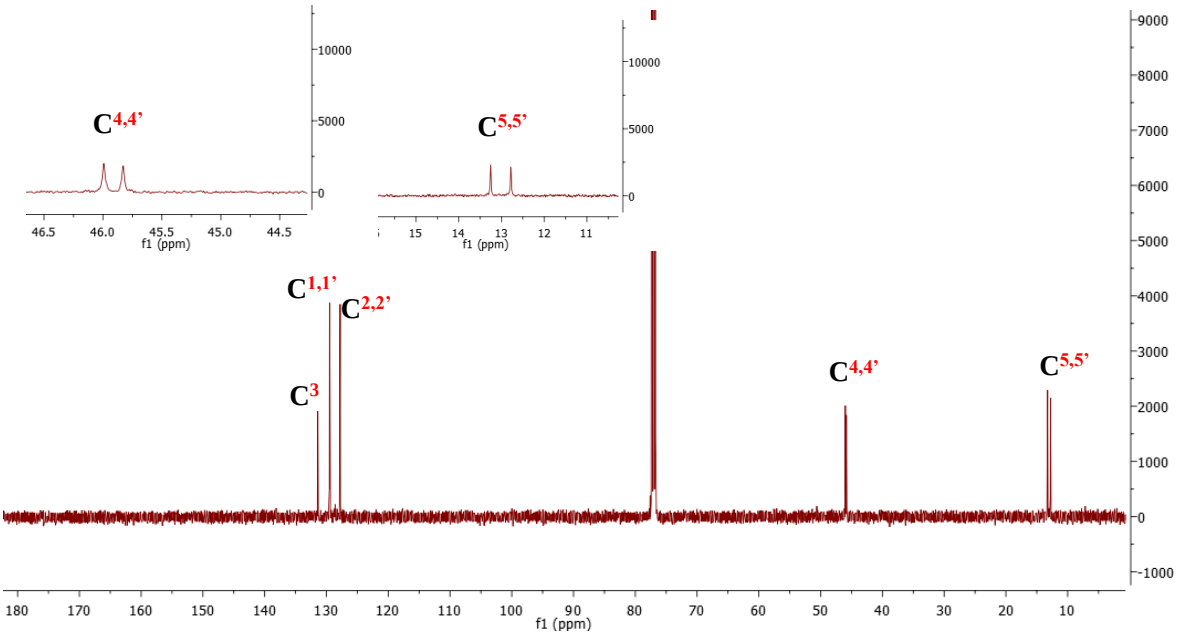
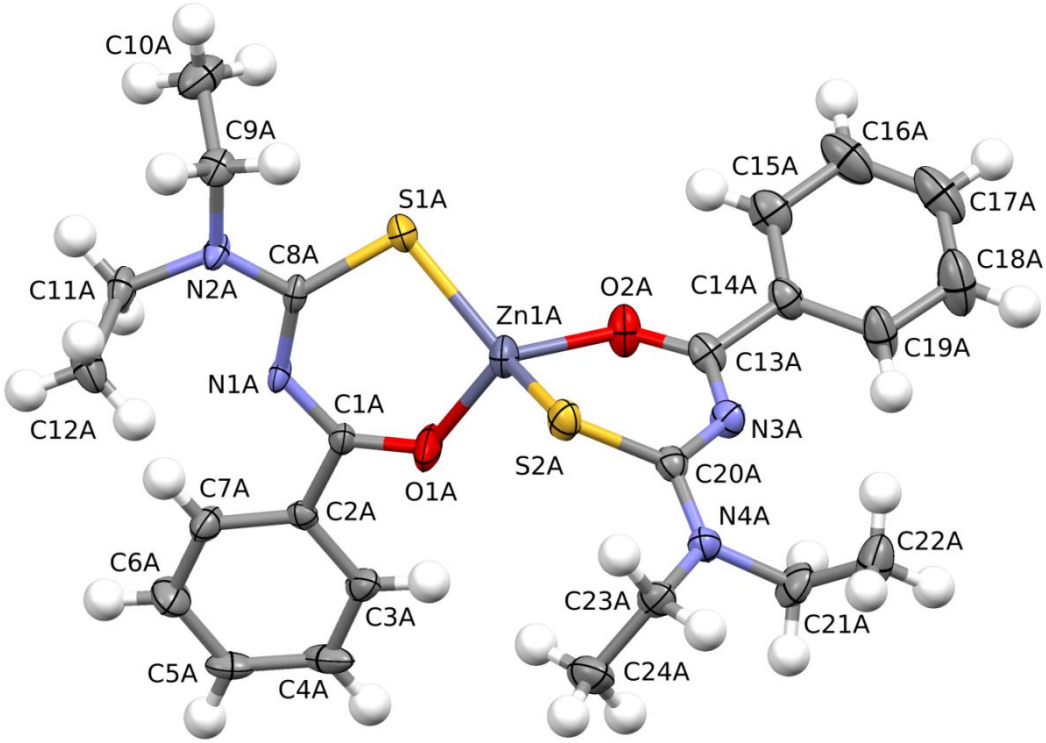


Figure 2.6: ^{13}C NMR spectra of $Zn(ATU)_2$ in $CDCl_3$ at 300 K with an insert of an enlarged view of the $C^{4,4'}$ and $C^{5,5'}$ carbons.

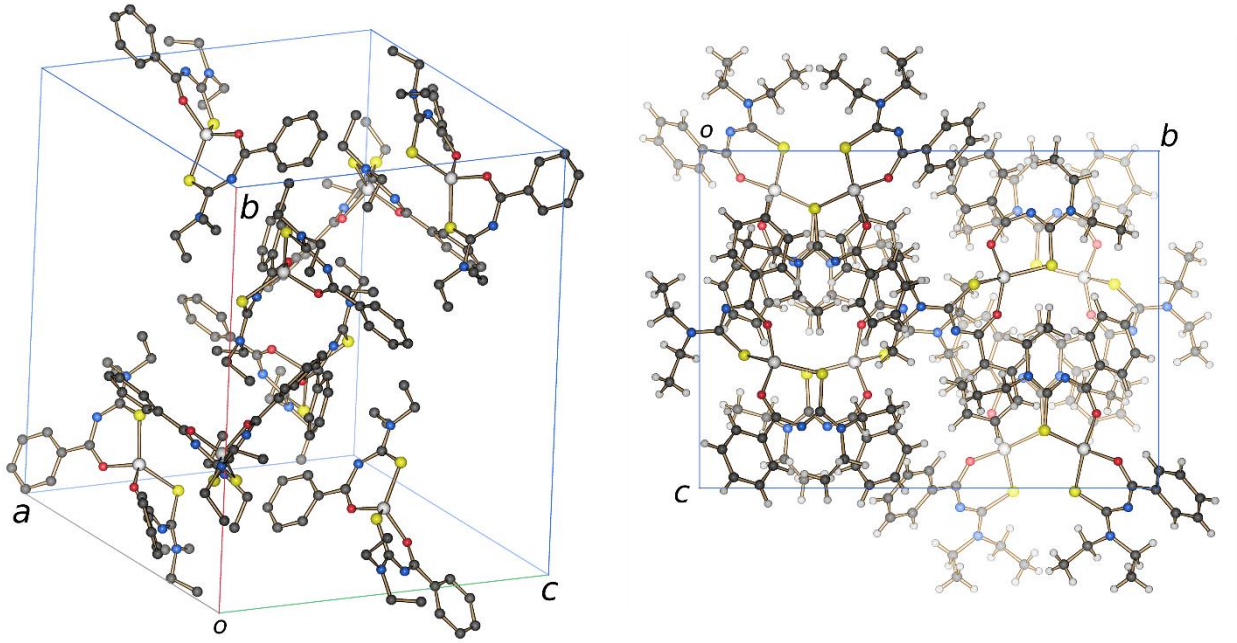
NMR spectroscopy unambiguously confirmed the synthesis of $Zn(ATU)_2$, furthermore, we used crystallographic data as given is Table 2.2. Single crystals of $Zn(ATU)_2$, suitable for x-ray diffraction were grown from an ethanol solution by slow evaporation at room temperature. This yielded transparent crystals that were air stable with melting points in the range between 135-141 ˚C in good yields. The structure of $Zn(ATU)_2$ was consistent with Infra-red and NMR spectroscopy. ORTEP diagrams of the complex are shown in Figure 2.7(a) and the packing diagrams were shown in Figures 2.7(b) and (c). $Zn(ATU)_2$ has 8 molecules in the asymmetric unit because of the monoclinic crystal system. (Table 2.2) The general distribution can be seen in the packing diagrams shown in Figures 2.7 (b) and (c).

The Zn atom of the complex was coordinated by two *N,N*-di(ethyl)-*N'*-benzoylthiourea anions via the S- and O- donor atoms. Their coordination geometry is tetrahedral, with the

tetrahedral angles being narrow 98.2 (2)˚ for O(1A)-Zn-S(1A) to a wide 113.1(2)˚ for O(2A)-Zn-S(1A), which is expected for the presence two bulky benzoyl ligands in the coordination sphere. Two polymorphs of the uncoordinated ligand, HL^1 have been reported in literature[17] for comparison. Using this data, it is interesting to compare the former C=S and C=O double bond distances of 1.6767 (12) and 1.2188 (15) Å, respectively with those given in Table 2.3. A significant elongation of these bonds upon complexation is notable in the molecule, where the C-S and C-O bond lengths are now 1.747(8) and 1.253(10) Å, respectively. These bonds display an intermediate character between a double and a single bond length. The C-N bond due to the diethyl atoms attached to the N atoms are of single bond character with a bond length of 1.317(11) Å.



(a)



(b) **(c)**

Figure 2.7: Molecular structure of $Zn(ATU)_2$ where (a) is the ORTEP diagram and (b) and (c) are the general packing diagrams.

In summary, we have confirmed that the coordination of the metal precursor to the free ligand through the O- and S- donor atoms by FTIR spectroscopy; where we saw the disappearance of the NH- stretching frequency upon the formation of the complex. The band corresponding to the thiocarbonyl stretching also shifts to lower wave numbers upon complexation due to the delocalization of electrons causing the bond to assume a one and a half bond character. This intermediate character of the C-S and the C-O bonds are further confirmed by single crystal x-ray diffraction where these bond lengths are in agreement with the FTIR. Even with all this information, FTIR spectroscopy could only confirm the presence of the relevant functional groups, but not the structure of the complex. Thus, we made use of ^{1}H, ^{13}C, DEPT and 2D NMR spectroscopy to confirm the synthesis and confidently assign the protons and carbons of the complex, $Zn(ATU)_2$. The correlation diagrams confirmed the explicit assignment of our protons and carbons in the ^{1}H and ^{13}C spectra, respectively. We have further investigated the structure of our complex using single-crystal xrd. Figures 2.7 show us the molecular structures of our complex.

2.3.3. Characterization of the zinc thiourea chloride

Both $Zn(TU)_2Cl_2$ and HL^2 have previously been synthesized in literature[18], the FTIR spectra of the thiourea ligand and complex are shown in Appendix A, Figure 1. The metal chloride can bind to the thiourea ligand in two possible ways; coordination can happen through the N- or the S- donor atoms of the ligand. However, it was previously [5] been confirmed that v(NH) bonds of thiourea are not significantly affected by upon coordination to the metal precursor, which indicates that the metal coordinates through the S atom. The signals positioned between 3000 and 3500 cm^{-1} correspond to the stretching modes of the NH_2 grouping of the thiourea. The bands from the thiourea ligand did not shift upon the formation of the complex, which indicated that N-Zn bonds are not present in the coordinated species. The absorptions observed at 1419 and 1089 in the thiourea spectrum correspond to the 1637 and 1110 absorption of the complex, respectively; these can be attributed to the N-C-N stretching vibrations. The increase in the frequency indicates a greater double bond character of th C to N bond when the complex forms. The bands due to the v(CS) stretching frequency for the ligand were seen at about 638 and 519 cm^{-1} and were shifted to lower frequencies upon coordination to 632 and 505 cm^{-1} for the complex, respectively. The shift to lower frequencies of v(CS) suggest the coordination of the metal is through the sulfur atom. Due to the metal chloride binding through the S atoms, it has been reported that the ^1H NMR shows little or no shift between the free and bound TU ligands, consequently, we have studied the ^{13}C NMR to confirm the synthesis of $Zn(TU)_2Cl_2$.The ^{13}C NMR of the $Zn(TU)_2Cl_2$ complex and the ligand, are shown in Figures 2.8.

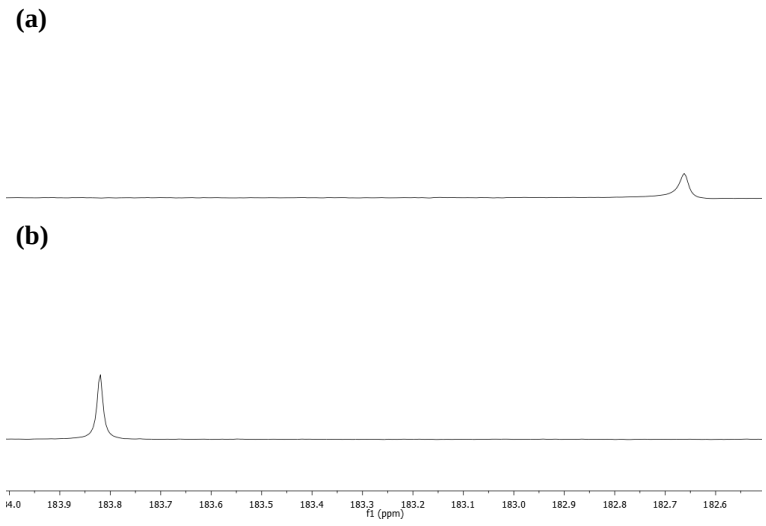


Figure 2.8: ^{13}C NMR spectrum of a) Zn(TU)2Cl2 and b) HL2 in DMSO-d6 at 300 K.

The ^{13}C NMR of free TU shows a singlet at 183.85 ppm, upon complexation with the Zn atom, the singlet shifts to 182.65 ppm. The shift is reported to be due to a lowering of the C=S bond order, upon coordination, a shift of the electron density yields a partial double bond character in the C-N bond.[19] X-ray molecular structures in Appendix A, Figure 2, confirm the coordination of the Zn atom through the S atom.

Table 2.2: Crystal data and structure refinement for $Zn(ATU)_2$

Empirical formula	$C_{24}\ H_{30}\ N_4\ O_2\ S_2\ Zn$	
Formula weight	536.01	
Temperature	173(2) K	
Wavelength	0.71073 Å	
Crystal system	Monoclinic	
Space group	P 21/c	
Unit cell dimensions	a = 15.7415(3) Å	α= 90°.
	b = 20.9289(4) Å	β= 103.1380(10)°.
	c = 15.9712(4) Å	γ= 90°.
Volume	5124.02(19) $Å^3$	
Z	8	
Density (calculated)	1.390 Mg/m^3	
Absorption coefficient	1.149 mm^{-1}	
F(000)	2240	
Crystal size	0.406 x 0.294 x 0.156 mm^3	
Theta range for data collection	1.328 to 28.364°.	
Index ranges	-19<=h<=21, -27<=k<=27, -19<=l<=21	
Reflections collected	54699	
Independent reflections	12778 [R(int) = 0.0645]	
Completeness to theta = 25.242°	100.0 %	
Absorption correction	None	
Refinement method	Full-matrix least-squares on F^2	
Data / restraints / parameters	12778 / 0 / 603	

Goodness-of-fit on F^2	1.560
Final R indices [I>2sigma(I)]	R1 = 0.1577, wR2 = 0.4093
R indices (all data)	R1 = 0.1984, wR2 = 0.4282
Extinction coefficient	n/a
Largest diff. peak and hole	12.742 and -1.306 e.$Å^{-3}$

Table 2.3: Bond lengths [Å] and angles [°] for $Zn(ATU)_2$

C(1A)-O(1A)	1.253(10)
C(1A)-S(1A)	1.747(8)
C(1A)-N(1A)	1.317(11)
O(1A)-Zn(1A)-S(1A)	98.2(2)
O(2A)-Zn(1A)-S(2A)	113.1(2)

2.4. References

1. Moloto N., Revaprasadu N., Moloto M.J., O'Brien P., Raftery J. N,N'-diisopropylthiourea and N,N'-dicyclohexylthiourea zinc (II) complexes as precursors for the synthesis of ZnS nanoparticles. *S. Afr. J. Sci.* **105,** 258–263 (2009).
2. Garnovskii A. D., Sennikova E. V & Kharisov B. I. Coordination aspects in modern inorganic Chemistry. *Open Inorg. Chem. J.* **1,** 1–20 (2009).
3. Westra A. N., Bourne S. A., Koch K. R. First metallamacrocyclic complexes of Pt(IV) with 3,3,3',3'-tetraalkyl-1,1'-phenylenedicarbonylbis(thioureas): synthesis by direct or electrolytic oxidative addition of I_2, Br_2 and Cl_2. *Dalton transactions* 2916–2924 (2005).
4. Che D., Li G., Yao X., Zhu Y. & Zhou D. Simultaneous formation of both novel bis(sulfur) and bis(oxo)- bridged copper(II) dimers by reaction of N-benzoyl-N,N'-dimethyl- thiourea (HL) with $CuCl_2$. *Dalt. Trans.* 2683–2687 (1999).
5. Moloto M. J., Revaprasadu N., O'Brien P., Malik M. A. N-alkylthioureacadmium (II) complexes as novel precursors for the synthesis of CdS nanoparticles. *J. Mater. Sci. Mater. Electron.* **1,** 313–316 (2004).
6. Moloto N., Revaprasadu N., Musetha P. L., Moloto M. J. The effect of precursor concentration, temperature and capping group on the morphology of CdS nanoparticles. *J. Nanosci. Nanotechnol.* **9,** 4760–4766 (2009).
7. Bruker. in *APEX2* **2014.5,** 1–3652 (2005).
8. Sheldrick, G. M. A short history of SHELX. *Acta Crystallogr. Sect. A Found. Crystallogr.* **1,** 112–122 (2007).
9. Farrugia, L. J. ORTEP-3 for Windows - A version of ORTEP-III with a Graphical User Interface (GUI). *J. Appl. Crystallogr.* **30,** 565 (1997).
10. Spek, A. L. Structure validation in chemical crystallography. *Acta Crystallogr.* **D,** 148–155 (2009).
11. Douglass I. B., Dains F. B. The preparation and hydrolysis of mono-and disubstituted benzoylthioureas. *J. Am. Chem. Soc.* **56,** 1408–1409 (1934).
12. Moloto M.J., Malik M.A., O'Brien P., Motevalli M., Kolawole G.A. Synthesis and characterisation of some N-alkyl/aryl and N, N'-dialkyl/aryl thiourea cadmium (II) complexes. *Polyhedron* **1,** 595–603 (2003).
13. Rajasekaran R., Ushasree P.M., Jayavel R., Ramasamy P. Growth and characterization

of zinc thiourea chloride: a semiorganic nonlinear optical crystal. *J. Cryst. Growth* **1,** 563–567 (2001).

14. Nkabyo, H. A. A study on the reversible photo-induced isomerisation of platinum(II) and palladium(II) complexes of the N,N-dialkyl-N'-acyl(aroyl)thioureas with reversed-phase HPLC separation from related rhodium(III), ruthenium(III) and iridium(III) complexes (2014).
15. Zhong Z., Xing R., Liu S., Wang L., Caia S., Li P. Synthesis of acyl thiourea derivatives of chitosan and their antimicrobial activities in vitro. *Carbohydr. Res.* **1,** 566–570 (2008).
16. Gunasekaran N., Ng S.W., Tiekink E.R.T., Karvembu R. Hypodentate coordination of N,N-di(alkyl/aryl)-N′-acylthiourea derivatives in Cu(I) complexes. *Polyhedron* **1,** 41–45 (2012).
17. Gomes L., Santos L., Coutinho J., Schro¨derc B. & Low J. N'-Benzoyl-N,N-diethyl-thio-urea: A monoclinic polymorph. *Acta Crystallogr. Sect. E Struct. Reports Online* **E,** 148–155 (2010).
18. Isab A. A. & Wazeer M. I. M. Complexation of Zn(II), Cd(II) and Hg(II) with thiourea and selenourea. *J. Coord. Chem.* **58,** 529–537 (2005).
19. Ahmad S. , Isab A. A. & Arnold A. P. Synthesis and spectroscopic characterization of Silver(I) complexes of selenones. *J. Coord. Chem.* **56,** 539–544 (2003).

Chapter 3: Synthesis and Characterization of ZnS nanocrystals from $Zn(ATU)_2$

3.1. Introduction

Waste water from textile, paper and other industries contain harmful residual dyes as they are not readily biodegradable.[1] Purification techniques such as ozonisation and chlorination have previously been used but they possess a number of disadvantages.[2] Among the various physical, chemical and biological techniques for treatment of waste water, semiconductor photocatalysis has been identified as a cost-effective alternative for water purification. A variety of semiconductor catalysts has been developed and utilized.[3] Their small sizes and good optical properties also make them interesting and advantageous for application in photocatalysis.[4] Several semiconductor photocatalysts have been used for the treatment of waste water pollutants and these include TiO_2, ZnO, WO_3, CdS and ZnS.[5]

Because of their size-dependent properties, a certain care has to be taken during the synthesis of these semiconductor nanocrystals.[6] While they have been synthesized using various methods, the single-source precursor method is of particular interest as it already contains the metal-chalcogenide bond within the molecular precursor thus leading to a more controlled synthesis of the nanoparticles. The single-source precursor method involves the thermolysis of a molecular precursor in a high boiling solvent to yield the desired nanocrystals. Acylthiourea complexes have been identified as good molecular precursors in the preparation of semiconductor nanocrystals. Saeed *et al.*[7] have shown studies on the successful synthesis of symmetrical and unsymmetrical nickel (II) complexes of N-(dialkylcarbamathiol)-nitro substituted benzamide as single-source precursors for the deposition of nickel sulfide nanoparticles. In their studies, they used the aerosol-assisted chemical vapour deposition to synthesize the nanoparticles. Similarly, Bruce *et al.*[8] also showed the thermolysis of (N,N-diethyl-N'-benzoylselenoureato)Cd(II) complexes and their sulphur analogues to achieve CdSe and CdS nanoparticles, respectively. In both studies, it was evident that the metal complexes had the potential to form either, or both the metal oxides or metal selenide/sulfide particles, however, reports showed that the metal chalcogenides were the preferred products. Bruce *et al*. also investigated the thermolysis of the (N,N-diethyl-N'-benzoylselenoureato)Zn(II) complexes and their sulphur analogues. In her studies, she

showed that ZnSe formed at reaction temperatures between 325 °C and 475 °C, however, ZnO formed at lower temperatures. Furthermore, using the sulphur analogue allowed the deposition of the crystalline ZnS in the hexagonal phase at temperatures of 400 °C and 475 °C and the lower temperatures yielding the cubic ZnS phase. As a "proof of concept", Bruce further thermolized (N,N-diethyl-N'-benzoylthiourea)Zn(II) at 150 °C for 60 min, in her studies, she confirmed the synthesis of cubic ZnS nanoparticles from this method. The preliminary investigations she conducted on the use of other N,N-dialkyl-N'-benzoyl(thio)selenourea metal complexes as single source precursors revealed that both (N,N-diethyl-N'-benzoylselenoureato)Zn(II) and its sulphur analogue showed the potential as single source precursors for the formation of ZnO and ZnS nanoparticles respectively.[8] Herein, in this chapter, the (N,N-diethyl-N'-benzoylthiourea)Zn(II) ($Zn(ATU)_2$, Figure 3.1) has been used as a single-source precursor for colloidal synthesis of ZnS nanoparticles. Parameters such as time, temperature, precursor concentration and capping agents were varied to study their effect on the properties of the nanoparticles and to modify these conditions to produce well-passivated ZnS nanoparticles.

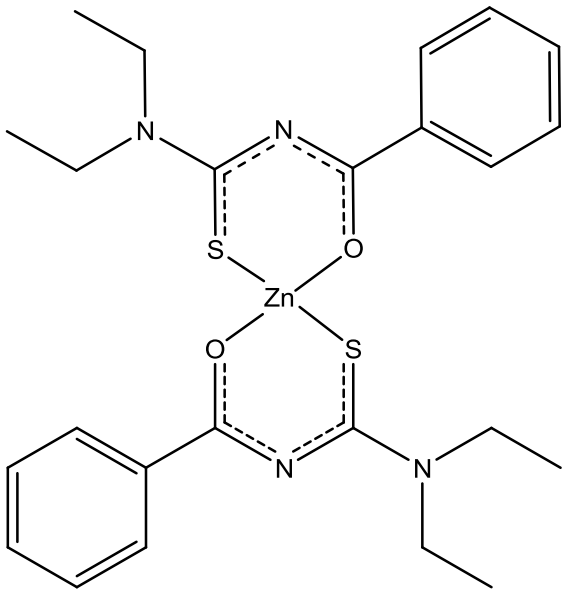


Figure 3.1: A structure of Zn(ATU)2.

3.2. Experimental procedures

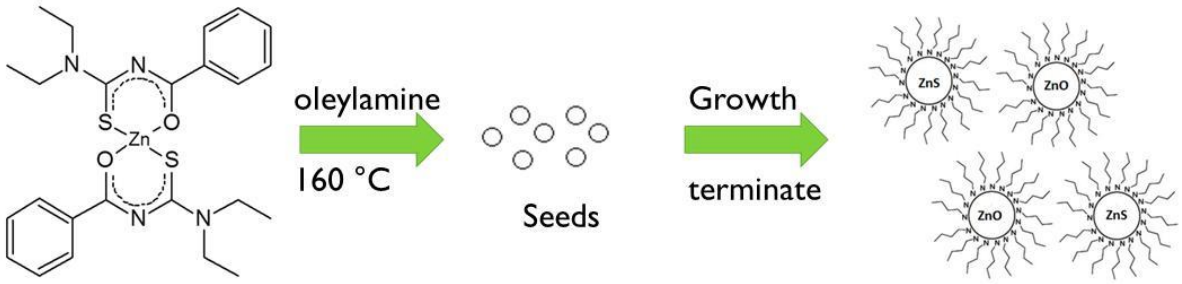
3.2.1. Chemicals

Oleylamine (OAm), dodecanethiol (1-DDT), tri-n-octylphosphine oxide (TOPO), hexadecylamine (HDA) and trioctylphosphine (TOP) were purchased from Sigma Aldrich

and used as received. Toluene, ethanol, acetone and methanol were obtained from Kemical and used as received. Thiourea was (analytical grade) obtained from Sigma Aldrich and was used as purchased to prepare the precursors.

3.2.2. Synthesis of ZnS nanoparticles using $Zn(ATU)_2$ complex as a single-source precursor

The ZnS nanocrystals were synthesized according to the method outlined in Scheme 3.1. The synthesis of ZnS nanocrystals using $Zn(ATU)_2$ as a single-source precursor was optimized by varying certain reaction parameters to achieve the best nanoparticle size and good dispersity. A series of experiments focussing on optimizing the time, temperature, precursor concentration and coordinating solvent were performed.



Scheme 3.1: A scheme showing the thermolysis of $Zn(ATU)_2$ in the presence of a capping agent to form metal chalcogenides.

In a typical experiment, OAm (3.71 mL) was degassed at 100 °C for 15 min and heated to 160 °C. 0.2014 g of the precursor was quantitatively transferred into the hot OAm. Upon contact of the solid precursor and the OAm, a slight decrease in the temperature of the solution was noted. The solution was allowed to stabilize at 160 °C and aliquots were obtained at 5 min time intervals from 5 min to 30 min. The reaction was then terminated and the resulting solutions were allowed to cool to 70 °C, methanol was then added to the solution to form a white precipitate. The precipitate was separated from the mother liquor by centrifugation and the particles were washed several times with methanol, and then air-dried to yield OAm-capped ZnS nanoparticles. Time, temperature, concentration and capping agents were varied and the conditions are tabulated in Table 3-1, 3-2, 3-3 and 3-4.

Table 3-1: Reaction parameters for time experiments

Samples	Precursor: capping agent molar ratio	Temperature	Time (min)	Coordinating solvent
A_1	1:1	160 °C	5	OAm
A_2	1:1	160 °C	10	OAm
A_3	1:1	160 °C	15	OAm
A_4	1:1	160 °C	20	OAm
A_5	1:1	160 °C	25	OAm
A_6	1:1	160 °C	30	OAm

Table 3-2: Reaction parameters for temperature experiments

Samples	Precursor: capping agent molar ratio	Temperature	Time (min)	Coordinating solvent
A_4	1:1	160 °C	20	OAm
B_1	1:1	180 °C	20	OAm
B_2	1:1	200 °C	20	OAm
B_3	1:1	220 °C	20	OAm
B_4	1:1	240 °C	20	OAm
B_5	1:1	260 °C	20	OAm

Table 3-3: Reaction parameters for the precursor: capping agent molar ratio experiments

Samples	Precursor: capping agent molar ratio	Temperature	Time	Coordinating solvent
B_2	1:1	200 °C	20 min	OAm
C_1	2.5:1	200 °C	20 min	OAm
C_2	5:1	200 °C	20 min	OAm
C_3	7.5:1	200 °C	20 min	OAm
C_4	10:1	200 °C	20 min	OAm

Table 3-4: Reaction parameters for the coordinating solvent experiments

Samples	Precursor: capping agent molar ratio	Temperature	Time	Coordinating solvent
C_1	2.5:1	200 °C	20 min	OAm
D_1	2.5:1	200 °C	20 min	HDA
D_2	2.5:1	200 °C	20 min	1-DDT
D_3	2.5:1	200 °C	20 min	TOPO

3.2.3. Characterisation techniques

3.2.3.1. Optical characterization

The optical properties of the materials were determined by placing the toluene dispersion of the nanoparticles into quartz cuvettes (1 cm path length). A Perkin Elmer Lambda 75S UV–Vis–NIR Spectrophotometer was used to carry out the optical measurements. A Perkin Elmer LS55 with a xenon lamp (150 W) and a 152 P photo multiplier tube as a detector was used to measure the photoluminescence of the particles.

3.2.3.2. Electron microscopy

The transmission electron microscopy (TEM) images were obtained using a Technai G2 TEM Spirit operated at 200 kV. The samples were prepared by placing a drop of a dilute solution of the sample in toluene onto carbon-coated copper grids. The samples were allowed to dry completely at room temperature.

3.2.3.3. Powder X-Ray diffraction

X-Ray diffraction (XRD) patterns of powdered samples were measured on Bruker D2 Phaser desktop diffractometer equipped with a LYNXEYE PSD detector (set to measure a 5° 2θ angular range), 2.5° primary and secondary beam Soller slits, and Co X-ray micro-source (Kα with λ = 1.78897 Å) operated at 30 kV and 10 mA. The goniometer radius of the diffractometer was 70.7 mm. The instrument was also fitted with a secondary beam Fe filter to attenuate Kβ radiation and a 3 mm air-scatter slit. Diffraction data were collected in the 2θ range 10-90° in 0.0260° steps and at a count time of 0.5 sec/step. Particle sizes were estimated using the Debye-Scherrer equation (Equation 3.1),

$$\tau = \frac{K\,\lambda}{\beta\,Cos\,\theta} \qquad (3.1)$$

where:

- τ is the mean size of the ordered (crystalline) domains.
- K is a dimensionless shape factor, with a value close to unity. The shape factor has a typical value of about 0.9, but varies with the actual shape of the crystallite.
- λ is the X-ray wavelength.
- β is the line broadening at full width at half the maximum intensity (FWHM), after subtracting the instrumental line broadening, in radians.
- θ is the Bragg angle (in degrees).

3.3. Results and discussion

3.3.1. Effect of time on the properties of ZnS

3.3.1.1. Structural properties

The effect of time on the properties of semiconductor nanoparticles is a well-studied discipline. Ostwald's ripening is considered a vital threshold to overcome when optimizing reaction parameters such as time and temperature.[9] The ripening effect results in smaller crystals dissolving and recrystallizing on larger more stable crystals, as a result, longer reaction times are associated with larger crystals. [10] A study on the on the size and shape determining properties of CdS previously showed a successive growth of particles with time.[11] The effect of time on the properties of ZnS nanoparticles synthesized from $Zn(ATU)_2$ has not been reported.

X-Ray diffraction studies were conducted to unambiguously confirm the type of nanoparticles obtained from the single-source precursor and also to establish the crystal phases of the particles formed. The XRD patterns obtained from the different times are depicted in Figure 3.2. The diffractograms from all the samples showed three peaks that were indexed to a cubic zinc blende phase (JCPDS card: 01-089-2427). The peaks corresponded to crystals planes at (111), (220) and (311). The XRD patterns gave broad peaks which were indicative of small sizes of the nanoparticles obtained. The Scherrer equation was used to estimate the crystallite sizes of the ZnS across all time intervals. The particles collected after 5 min and 10 min had average crystallite sizes of 2.56 nm and 2.55 nm respectively. At 15

min, the average crystallite size was 4.32 nm, with sizes dropping again at 20 min to 2.31 nm and slightly increasing for samples taken at 25 min (2.63 nm) and 30 min (2.75 nm). The nanoparticles are believed to grow as a result of crystal formation and the size drop is explained as due to nanoparticle precipitation.[12] This phenomenon is due to nanoparticles adsorbing non-specifically on to the surfaces of the growing crystals to physically slow down their growth, as nanoparticles gradually adsorb over time on to the crystal surface, the rate of the crystal growth also decreases.

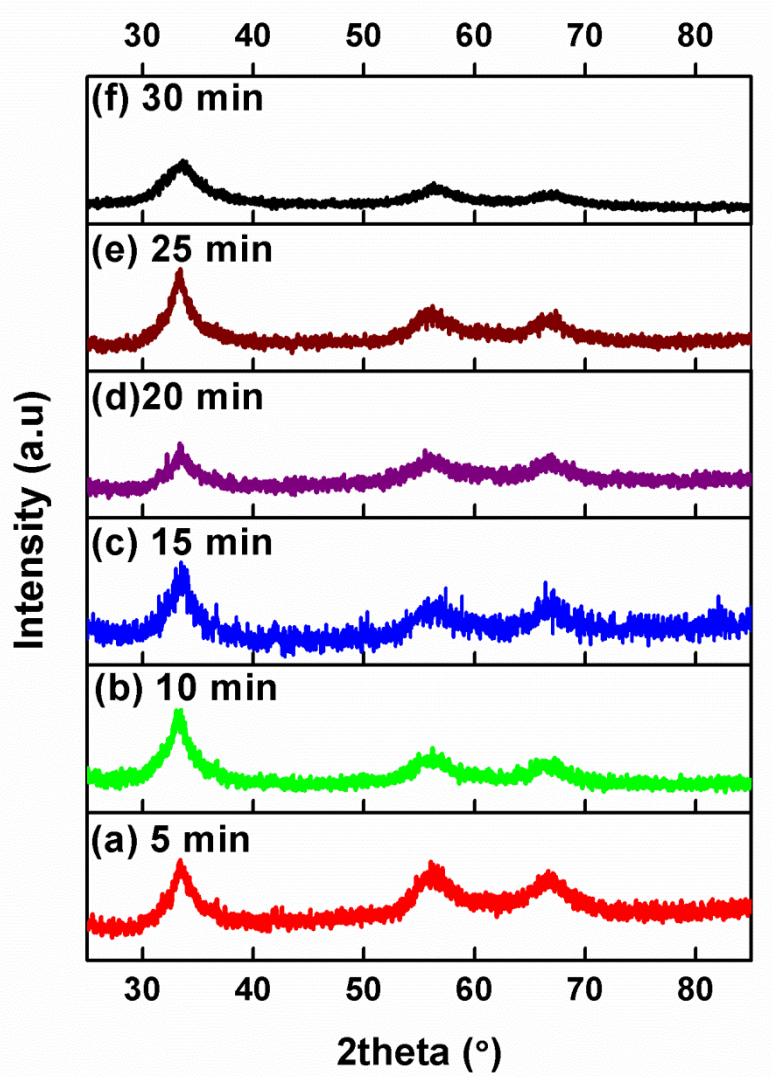


Figure 3.2: PXRD patterns of zinc sulfide nanoparticles collected from $Zn(ATU)_2$ at (a) 5 min, (b) 10 min, (c) 15 min, (d) 20 min, (e) 25 min and (f) 30 min in OAm at 160 °C.

The morphology of the nanoparticles was investigated using TEM. The micrographs displayed in Figure 3.3 showed the particles across all time intervals were needle-like in

shapes. The TEM micrographs also revealed that the particle sizes were very small. This was consistent with the trend obtained from the Scherrer calculations. It is important to note that the Scherrer equation was developed to estimate crystallite sizes for spherical and cubic particles where the shape factor K was estimated to be 0.89 and 0.94 for spherical and cubic particles respectively, however, it is generally accepted that for unknown particles, the estimated K value is 0.9.

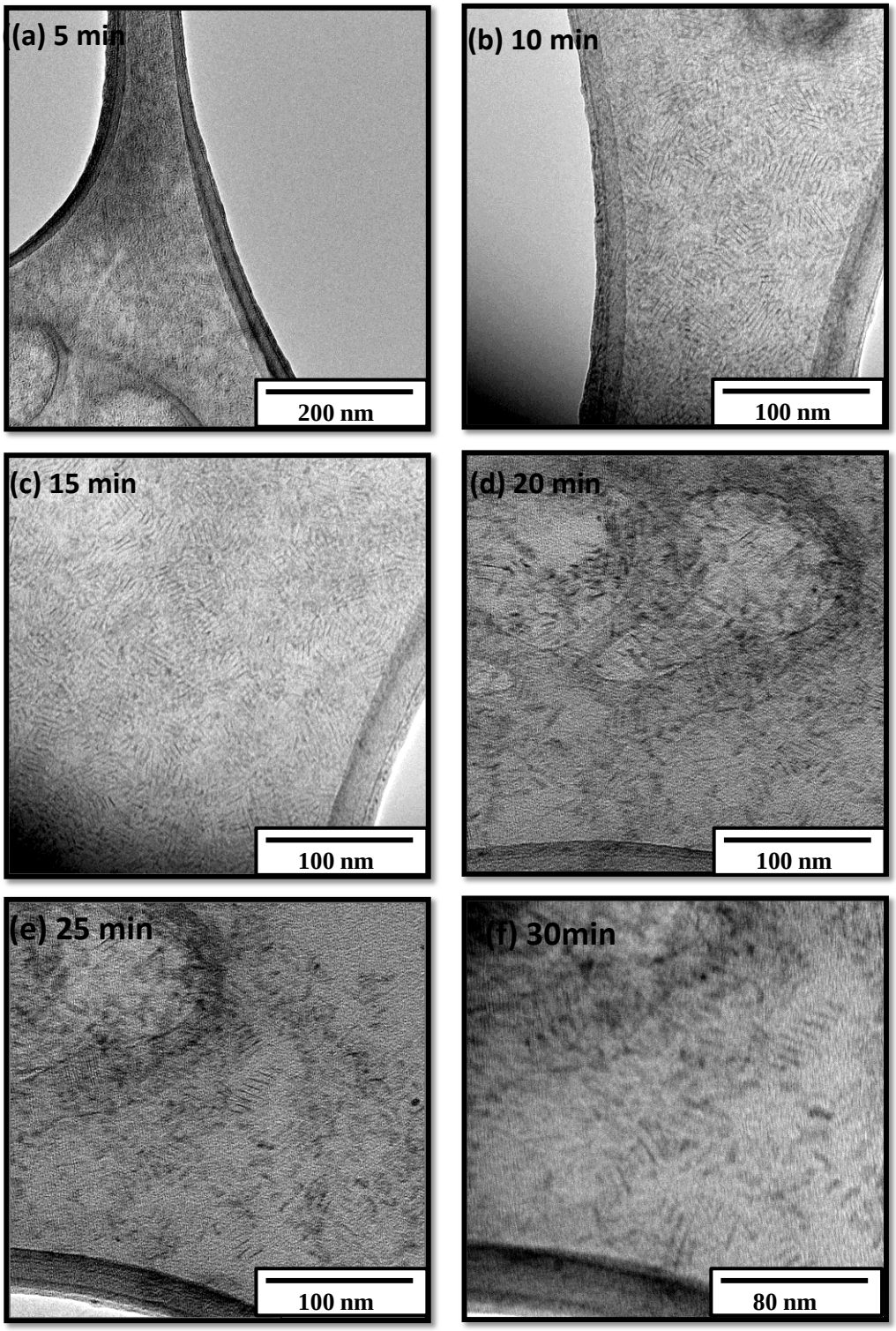


Figure 3.3: TEM micrographs of zinc sulfide nanoparticles collected from $Zn(ATU)_2$ at (a) 5 min, (b) 10 min, (c) 15 min, (d) 20 min, (e) 25 min and (f) 30 min in OAm at 160 °C.

3.3.1.2. Optical properties

The absorption and emission spectra of the ZnS nanoparticles synthesized at different times are shown in Figures 3.4 (a) and (b), respectively and summarized in Table 3-5. The absorption spectra of the samples showed that the particles had band-edges ranging between 325 nm and 338 nm. Table 3-5 shows that all the band-edges were blue-shifted from the bulk band-edge of ZnS that is 340 nm; the blue-shift in the band-edges indicates that the sizes of the nanoparticles were indeed in nanoscale regime and the excitons are under quantum confinement. The 5 min, 10 min and 25 min samples had a tailing shape which is indicative of a higher degree of poly-dispersity in these samples which was confirmed by the emission spectra, where the FWHM values listed in Table 3-5 were relatively higher for the above-mentioned samples. The emission Gaussian shape and relatively narrow size distribution in the samples indicated minimal to no surface defects, however, the 15 min sample had a broader emission peak, indicating a possible presence of surface defects perchance, caused by vacancies in the larger crystals as suggested by the Scherrer equation. The emission maxima were observed at 410 nm, which were red-shifted from the absorption spectra, also in agreement with the UV-Vis spectra that the nanoparticles are in nanoscale regime. The FWHM values revealed that the 20 min sample had a higher degree of monodispersity.

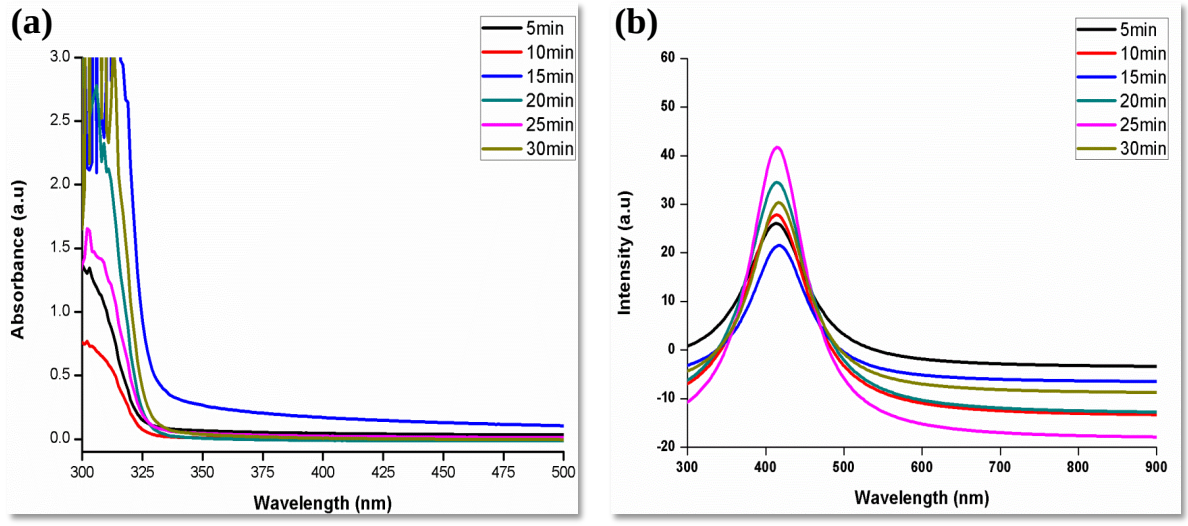


Figure 3.4: (a) Absorption and (b) emission spectra (λ_{exc}= 250 nm) of zinc sulfide nanoparticles collected from $Zn(ATU)_2$ at 5 min, 10 min, 15 min, 20 min, 25 min and 30 min in OAm at 160 °C.

Table 3-5: Optical properties of ZnS nanocrystals of the time experiments synthesized from $Zn(ATU)_2$

Time (minutes)	Band Edge (nm)	Emission max. (nm)	FWHM (nm)
5	325	410	93
10	325	410	91
15	338	410	77
20	326	410	69
25	327	410	80
30	328	410	77

3.3.2. Effect of temperature on the properties of ZnS

3.3.2.1. Structural properties

Using the optimal synthesis time of 20 min, a study on the effect of the reaction temperature was carried out. The single-source precursor method offers an impressive advantage of being able to control the properties of the nanoparticles by modifying the temperature. In her thesis, J. Bruce[8] reports the use of $Zn(ATU)_2$ as a single-source precursor for the deposition of ZnS nanoparticles, temperature conditions in this study ranged from 250 °C to 475 °C, these conditions were very high due to the Aerosol Assisted Chemical Vapour Deposition (AACVD) method she uses. The method makes the use of very high temperatures and complex processes, for that reason, the hot-injection method was used to study temperature and other parameter variations for this study. In her work, N. Moloto[13] reports that the synthetic temperature is highly determined by the capping agent where, in this case, OAm has a melting temperature of 21 °C and a boiling temperature of 364 °C and can thus be used within this range, herein this section reports on the hot-injection of $Zn(ATU)_2$ in OAm at temperatures ranging from 160 °C to 260 °C, with 20 °C intervals between the temperatures.

The X-Ray diffraction patterns are displayed in Figure 3.5. The nanoparticles synthesized at all temperatures were indexed to a cubic zinc blend phase (JCPDS card: 01-089-2427). Increasing the temperature from 160 °C across to 260 °C, a successive increase in the sharpness of the peaks is notable, which suggests that the crystallinity of our samples is also increasing. This undoubtedly meant that as the temperature was increased, the particle sizes

also increased. Using the Scherrer equation, average particle sizes from 160 °C to 260 °C were estimated to be 2.31 nm, 3.95 nm, 2.21 nm, 2.23 nm, 2.32 nm and 2.35 nm, respectively. The average particle sizes were seen to increase from 2.31 nm to 3.95 nm when increasing temperature from 160 °C to 180 °C, thereafter, at temperatures 200 °C and 220 °C, average particle sizes dropped to 2.21 nm and 2.23 nm, respectively and then increase again at 240 °C and 260 °C to 2.32 nm and 2.35 nm respectively. This scenario when nanoparticles increase in size until a certain threshold and then decrease again is described by Jiang *et. al.*[14] as caused by the fusion growth process. This is explained as a phenomenon when nanoparticles aggregate or come in contact and they fuse together like droplets to increase the total surface energy and form larger particles, upon frequent collision (which can be caused by increased temperatures), smaller particles are then formed from the bigger ones.[15] The growth of the nanoparticles after the formation of the smaller particles is then driven by Ostwald's ripening.

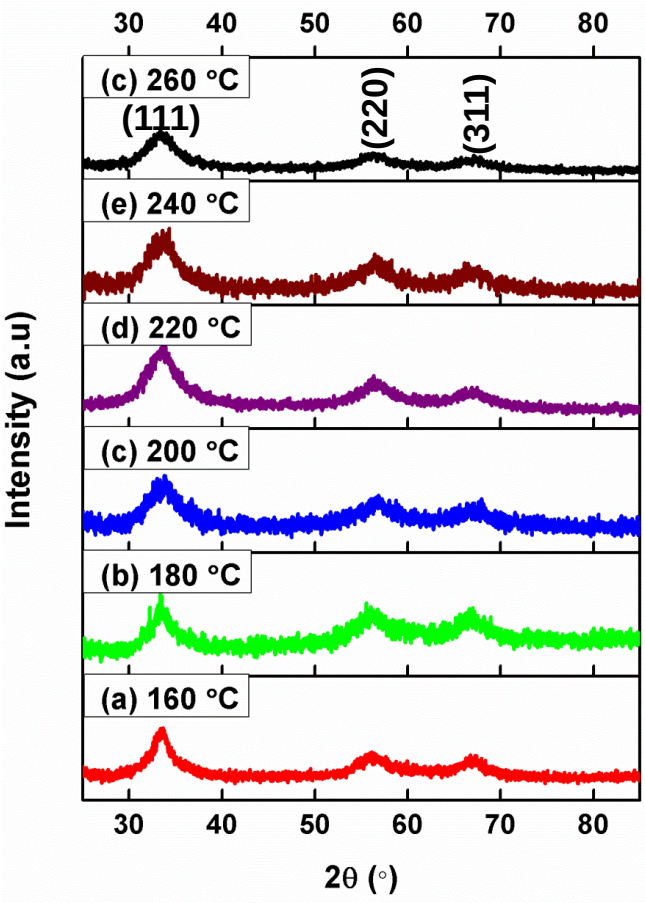


Figure 3.5: PXRD patterns of zinc sulfide nanoparticles collected from $Zn(ATU)_2$ at (a) 160 °C, (b) 180 °C, (c) 200 °C, (d) 220 °C, (e) 240 °C and (f) 260 °C in OAm.

The morphologies of the nanoparticles were determined by TEM as shown in Figure 3.6. The TEM micrographs show that the particles that were previously needle-like at 160 °C, became rather undefined at 180 °C more like there is a transition between needle-like and spheres. At higher temperatures, i.e. 200 °C, 220 °C and 240 °C, the particles became spheres. As the temperature was further increased, the needle-like nature of the particles reappeared. It is also interesting to note that as the temperature was increased, the particles seemed to be more mono-dispersed. Also evident from the TEM is that there is an increase of nanoparticles sizes from 160 °C to 180 °C, subsequently, a decrease in sizes from the 180 °C – 240 °C samples is observed, however, there is a slight increase is observe for the 260 °C sample. These observations are in agreement with the results obtained from XRD and the Scherrer calculations. The fusion growth process is validated by the clear increase of the nanoparticle sizes at 180 °C and the subsequent decrease in sizes from 200 °C onwards.

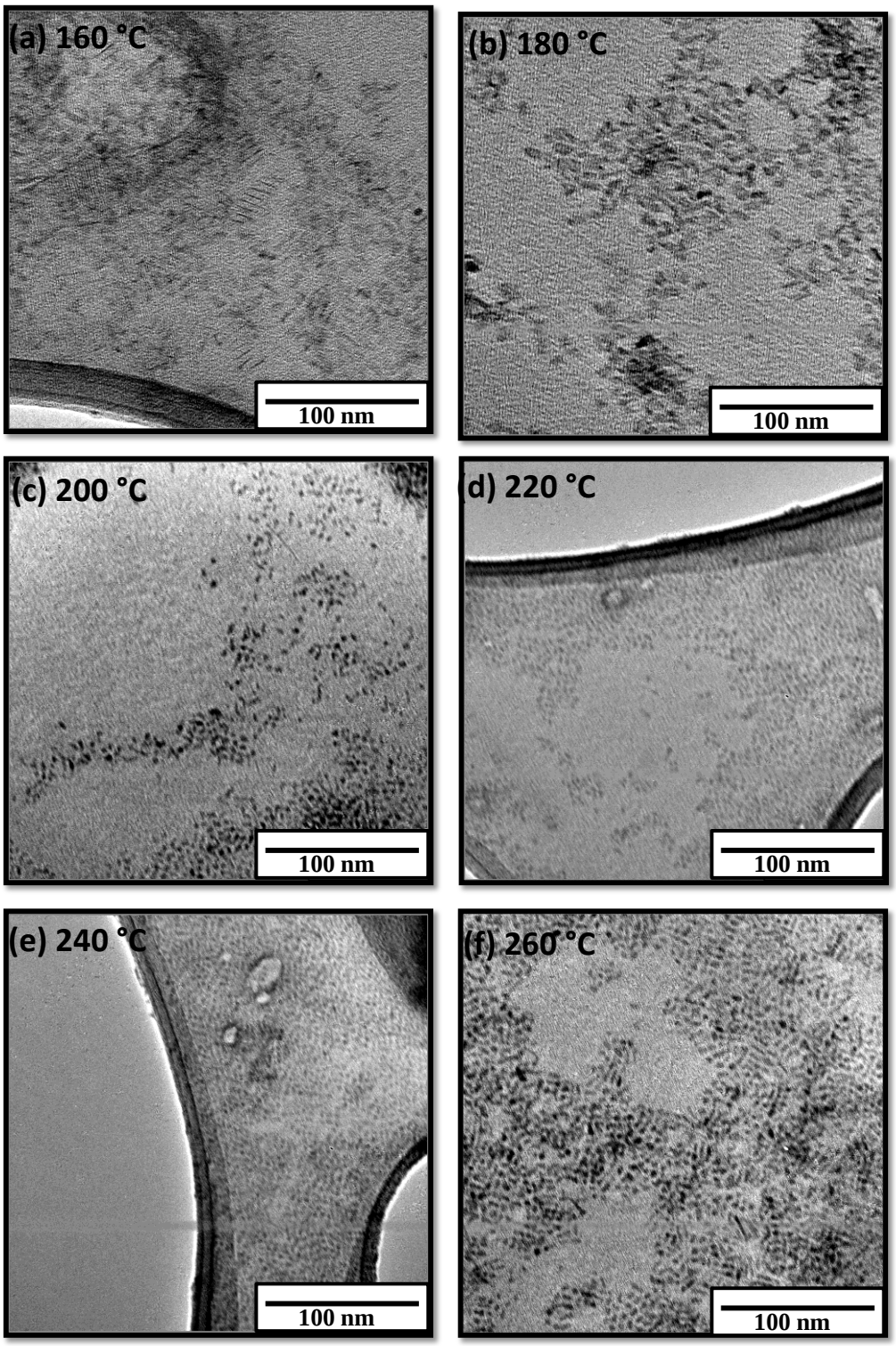


Figure 3.6: TEM micrographs of zinc sulfide nanoparticles collected from Zn(ATU)2 at (a) 160 °C, (b) 180 °C, (c) 200 °C, (d) 220 °C, (e) 240 °C and (f) 260 °C in OAm after 20 min

3.3.2.2. Optical properties

The optical characterization of the ZnS synthesized at different temperatures is shown in Figure 3.7 and summarized in Table 3-6. The absorption curves in Figure 3.7(a) range from 326 nm to 332 nm. According to the curves, the band edge of samples synthesized at 160 °C that were previously 326 nm increased to 332 nm at 180 °C, which suggested that nanoparticles increase in size at 180 °C. Thereafter, the band edges of the materials synthesized at 200 °C and 220 °C decreased to 310 nm and increase again at 240 °C and 260 °C to 330 nm and 331 nm, respectively. The band edges of the nanoparticles synthesized suggest the nanoparticles start by increasing in size at 180 °C, particle sizes dropped dramatically at temperatures 200 °C and 220 °C, and then an increase was later observed again when temperature was increased to 240°C and 260 °C. The trend observed in the band edges of these nanoparticles and consequently the particle sizes, was well in agreement with the trend observed in the TEM of the nanoparticles in Figure 3.6. From the optical spectra, curves of nanoparticles synthesized at 200 °C and 220 °C were tailing as compared to the curves obtained at temperatures 160 °C, 180 °C, 240 °C and 260 °C, the tailing behaviour of the nanoparticles was indicative of poly-dispersed samples.

The photoluminescence spectra were displayed in Figure 3.7 (b). The peaks from all the samples were red-shifted from their corresponding band-edges. The emission maxima for all temperature samples was at 410 nm, the Gaussian curves being relatively narrow for all samples except the samples synthesized at 260 °C which could be attributed to the development of the needle-like nature of the nanoparticles seen in the TEM images in Figure 3.6 causing surface defects in these nanoparticles. It is important to note that the FWHM (Table 3-5) decreases as temperature increases, suggesting that the particle size distribution becomes more mono-dispersed with increasing temperature. These findings were in agreement with the TEM observations in Figure 3.6.

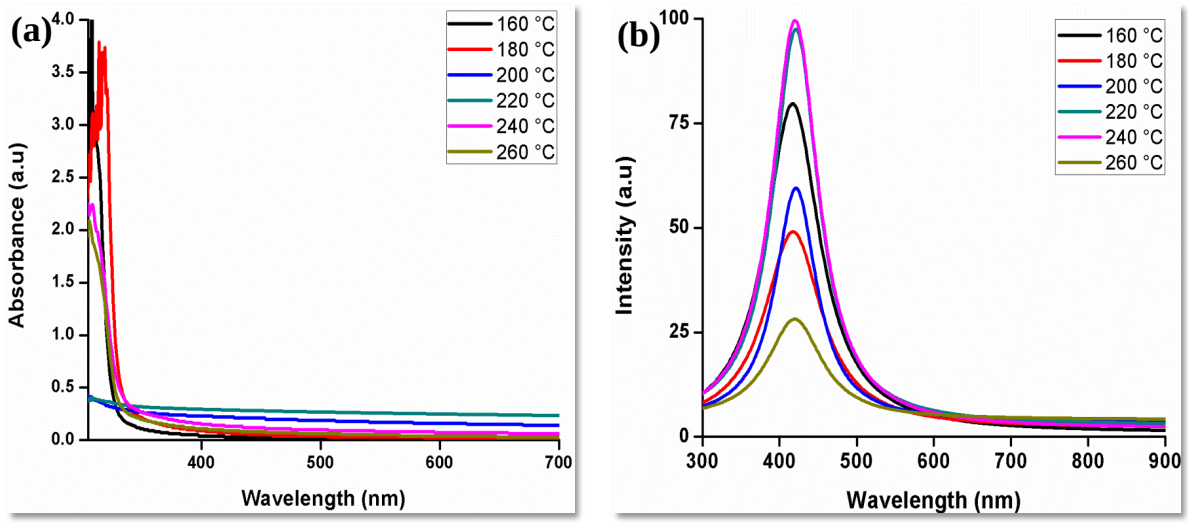


Figure 3.7: (a) Absorption and (b) emission spectra of zinc sulfide nanoparticles (λ_{exc}= 250 nm) collected from $Zn(ATU)_2$ at 160 °C, 180 °C, 200 °C, 220 °C, 240 °C and 260 °C in OAm.

Table 3-6: **Optical properties of ZnS nanocrystals of the temperature experiments synthesized from $Zn(ATU)_2$**

Temperature (°C)	Band Edge (nm)	Emission max. (nm)	FWHM (nm)
160	326	410	73
180	331	410	75
200	310	410	86
220	310	410	87
240	330	410	78
260	331	410	111

Evident from Figure 3.7 and Table 3-6, the optical properties of the nanoparticles at varied temperatures showed that the preferred temperatures were both 200 °C and 220 °C, however the 200 °C temperature was chosen to continue with precursor concentration studies for the main reason of saving energy by using low temperature yet still obtaining well passivated particles.

3.3.3. Effect of precursor concentration on the properties of ZnS

3.3.3.1. Structural properties

Having determined the optimum temperature, ZnS nanoparticles were synthesized at 200 °C for 20 min through varied precursor concentrations in OAm. The precursor and capping agent ratios were varied according to 1:15, 2.5:15, 5:15, 7.5:15 and 10:15 ratios. The XRD patterns of the synthesized particles are shown in Figure 3.8. The XRD patterns of the samples at a 1:15 ratio was indexed to the cubic ZnS (JCPDS card: 01-089-2427), however, the rest of the samples were indexed to the hexagonal phase of ZnS (JCPDS card: 01-089-2212). The peaks of the ZnS particles in XRD were largely broad, but for the 10:15 sample, there was a presence of sharp peaks that were not indexed and were considered impurities. The composition of these impurities could not be resolved; one could deduce that the impurities could be due to unreacted inorganic materials that cannot be indexed.[16]The ZnS peaks in the 10:15 sample had also shifted in comparison to the other ratios under study. This could have been a result of defects forming in nanoparticles or impurities due to materials that might not have reacted as the precursor concentration was high.[17] The size of nanoparticles was determined using the Scherrer equation where for ratios 1:15, 2.5:15, 5:15, 7.5:15 and 10:15 , average nanoparticle sizes were found to be 2.21 nm, 1.98 nm, 2.01 nm, 2.09 nm and 2.03 nm respectively. Evident from particle size calculations, the nanoparticle sizes drop at the ratio of 2.5:15, and slowly increase when the concentration is increased to 5:15 onwards. The increase in precursor concentration results in a reduced mean spacing between the molecules and nanoparticles,[17] which results in faster nanoparticle adsorption, consequently leading to slower crystal growth.[16]

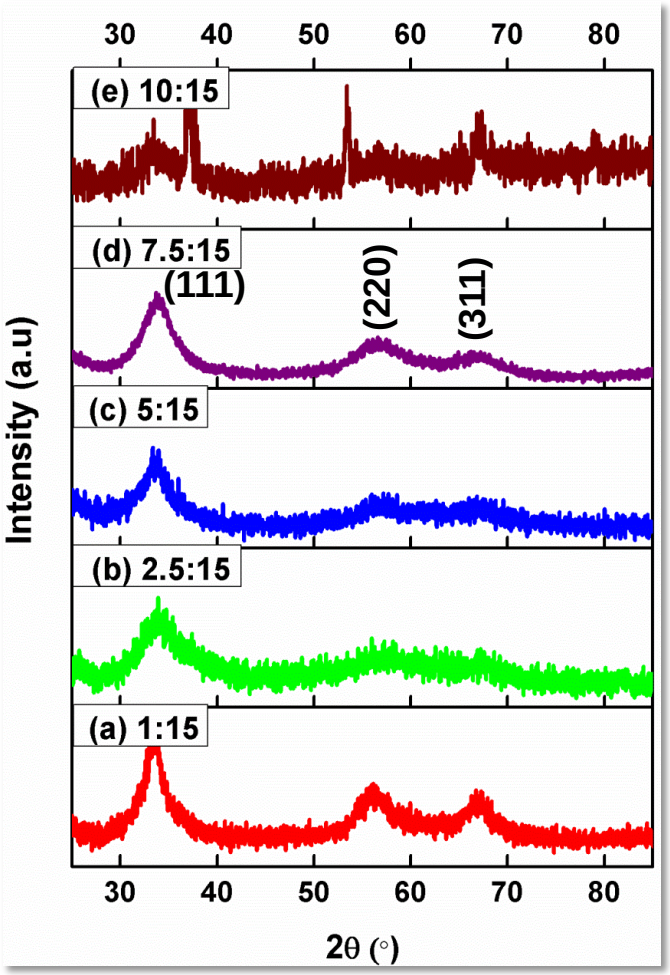


Figure 3.8: PXRD patterns of zinc sulfide nanoparticles collected from $Zn(ATU)_2$ at (a) 1:15, (b) 2.5:15, (c) 5:15, (d) 7.5:15 and (e) 10:15 in OAm.

The TEM micrographs of the synthesized ZnS at various concentration ratios revealed that particles generally agglomerated with increasing concentration as shown in Figure 3.9. Because nanoparticles have a high surface area to volume ratio, increasing the concentration results in surface atoms exhibiting stronger attractive forces between their nearest neighbours on the surface and hence the agglomeration witnessed[16] in the TEM images, confirming and agreeing with the results obtained from the XRD in Figure 3.8.

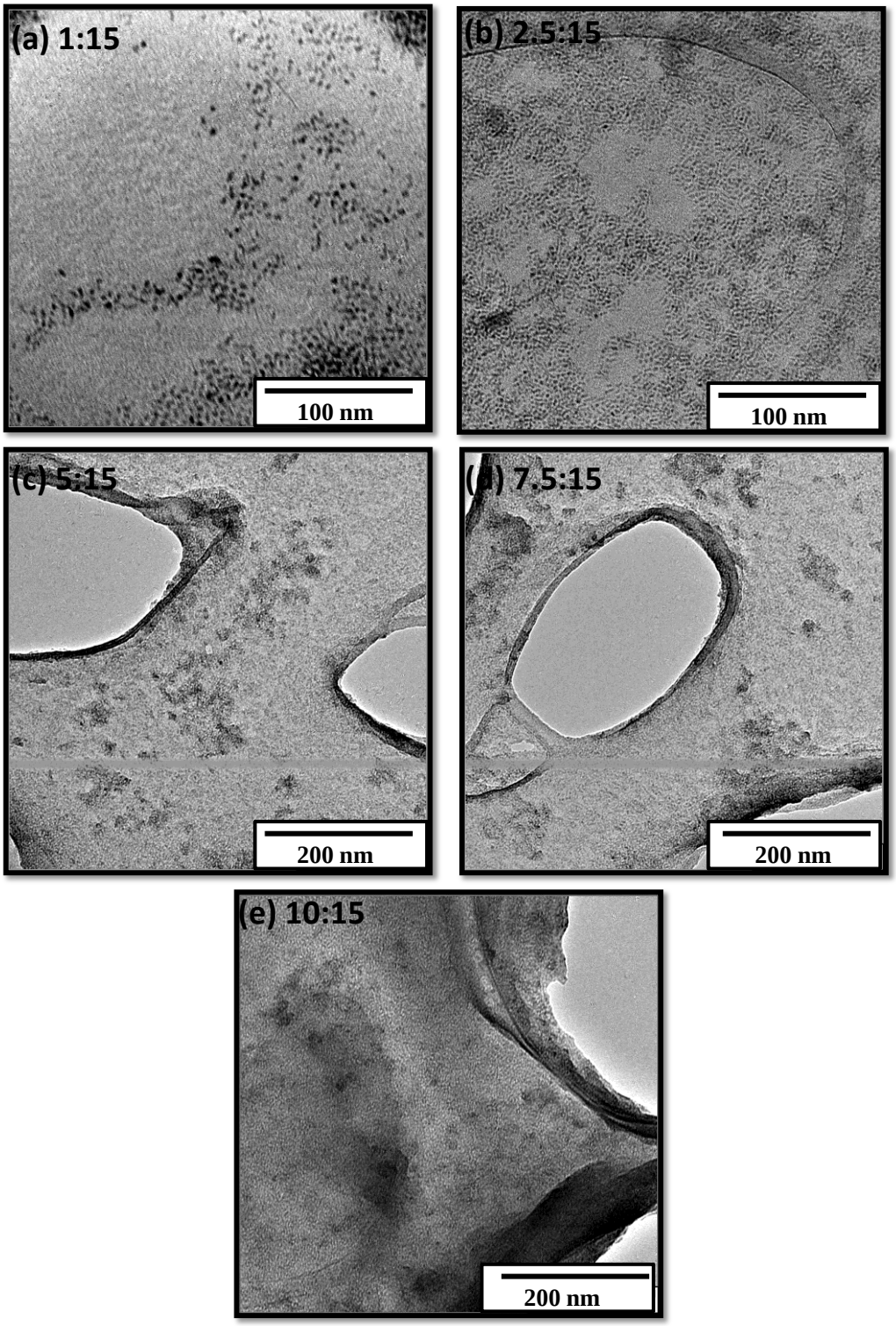


Figure 3.9: TEM micrographs of zinc sulfide nanoparticles collected from $Zn(ATU)_2$ at (a) 1:15, (b) 2.5:15, (c) 5:15, (d) 7.5:15 and (e) 10:15.

3.3.3.2. Optical properties

The UV-Vis absorption spectra of the ZnS prepared at different ratios were assembled in Figure 3.10 (a). The particles synthesized gave blue-shifted absorption band edges which ranged between 310 nm to 338 nm (Table 3-7). The particles synthesized gave blue shifted absorption band edges suggesting strong quantum confinement effects. The band edges of the concentration ratios from 1:15 to 10:15 were 310 nm, 310 nm, 312 nm, 313 nm and 315 nm respectively. The concentration ratio of 1:15 and 2.5:15 showed the highest blue-shift of all samples indicating the presence of smaller nanoparticles at these ratios; however the absorption curve of the 1:15 sample showed some degree of tailing, indicating polydispersity in the population of this sample, consequently, making the 2.5:15 ratios more favourable over the 1:15 ratio. These results are well in agreement with the TEM results observed in Figure 3.9. The photoluminescence spectra of the considered ratios were red-shifted from their corresponding band edges as shown in Figure 3.10 (b). The emission peaks were at maxima of nearly 410 nm for all ratios, there were slight differences in the maxima of the emission peaks (Table 3-7), from the emission maxima, it was noted that the more red-shifted the emission peaks from the corresponding band edges, the smaller particles.[18] The FWHM values have been summarized in Table 3-6 and have revealed that the particles synthesized with the ratio, 2.5:15 were more mono-dispersed and this was in agreement with the obtained TEM results in Figure 3.9.

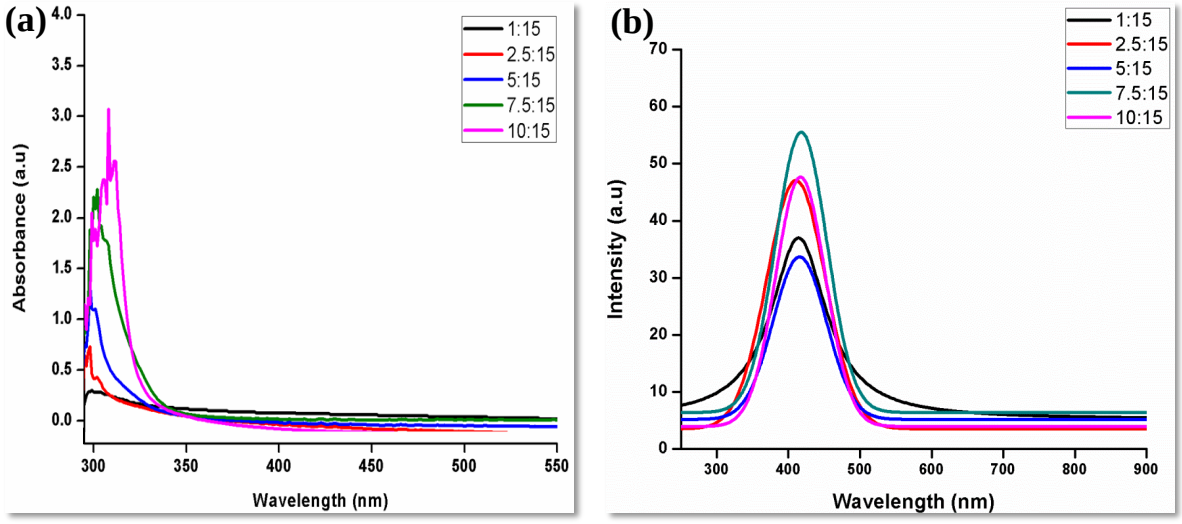


Figure 3.10: (a) Absorption and (b) emission spectra of zinc sulfide nanoparticles (λ_{exc}= 250 nm) collected from zinc (II) diethyl acylthiourea at 160 °C in OAm for various ratios (1:15, 2.5:15, 5:15, 7.5:15 and 10:15)

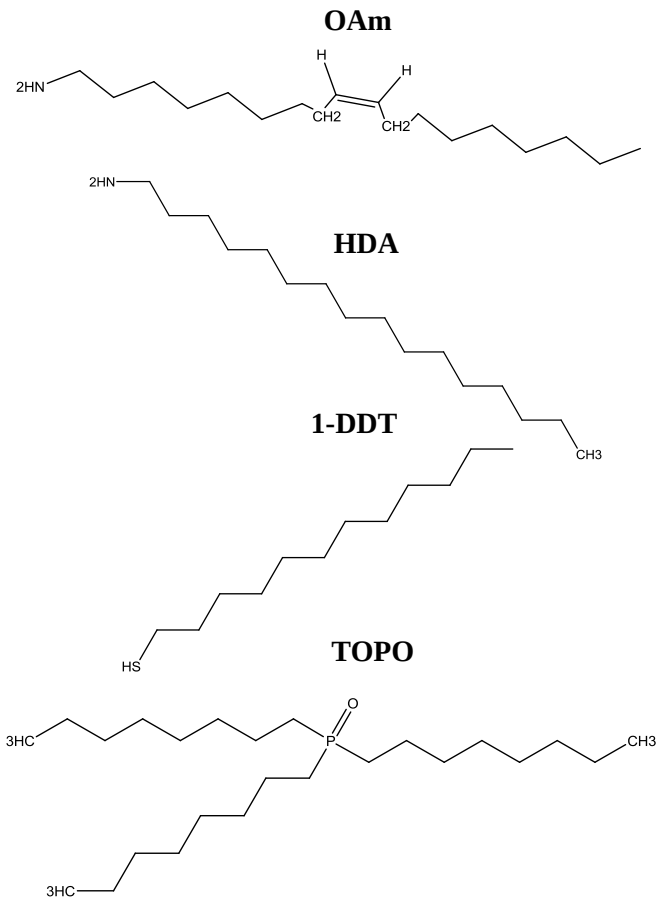
Table 3-7: Optical Properties of ZnS nanocrystals of the concentration experiments synthesized from $Zn(ATU)_2$

Precursor: capping agent molar ratio	Band Edge (nm)	Emission max. (nm)	FWHM (nm)
1:15	310	410	86
2.5:15	310	412	74
5:15	313	410	73
7.5:15	315	410	69
10:15	318	413	70

3.3.4. Effect of capping agent on the properties of ZnS

3.3.4.1. Structural properties

Capping agents are often used in the colloidal synthesis of nanoparticles to inhibit nanoparticle growth and aggregation as well as to control the structural characteristics of the resulting nanoparticles precisely.[19] Capping agents have also been reported to influence the reactivity hence the nucleation of the particles by binding to the surface of the nuclei either weakly or strongly. Additionally, they can have preferential attachment to specific crystallographic planes consequently resulting in the growth of anisotropic particles.[18] This section seeks to determine the effect that varying the capping agent has on the resulting ZnS nanoparticles, this was done by first replacing OAm with HDA and then with 1-DDT. Scheme 3.2 shows the structures and the functional groups that each capping agent possesses.



Scheme 3.2: Different capping agent molecules and their functionalities

Several attempts to study the effect of TOPO on the nanoparticles were unsuccessful, reaction conditions were modified to try and produce TOPO-capped nanoparticles with fail. Reaction times were extended, upon failure to produce any nanoparticles, then the reaction temperature was increased and as a last resort, the precursor concentration was varied still with no success. The crystallinity, phase composition and impurity detection of the synthesized ZnS particles were studied using XRD. Figure 3.11 shows the XRD diffractograms of the synthesized particles. As previously discussed, the XRD pattern of the OAm-synthesized material was indexed to the hexagonal ZnS phase (JCPDS card: 01-089-2212). Similarly, the DDT-synthesized sample was indexed to the same phase as the OAm sample. The HDA-synthesized particles were also indexed to the hexagonal ZnS phase, with a different JCPDS card number of 01-089-2145, indicating that the synthesized particles had different crystallographic planes from those synthesized from the OAm and HDA sample.[18] This comes as no surprise as the structure of 1-DDT introduces the presence of a sulfur atom (Scheme 3.2) that was previously not present in OAm and HDA hence changing the growth and nucleation kinetics of nanoparticles in the DDT solution. The crystallite sizes were

estimated from the Scherrer equation from the corresponding XRD diffractograms, these gave average sizes of 1.98 nm, 1.95 nm and 2.33 nm for the OAm-, DDT- and HDA-synthesized particles respectively.

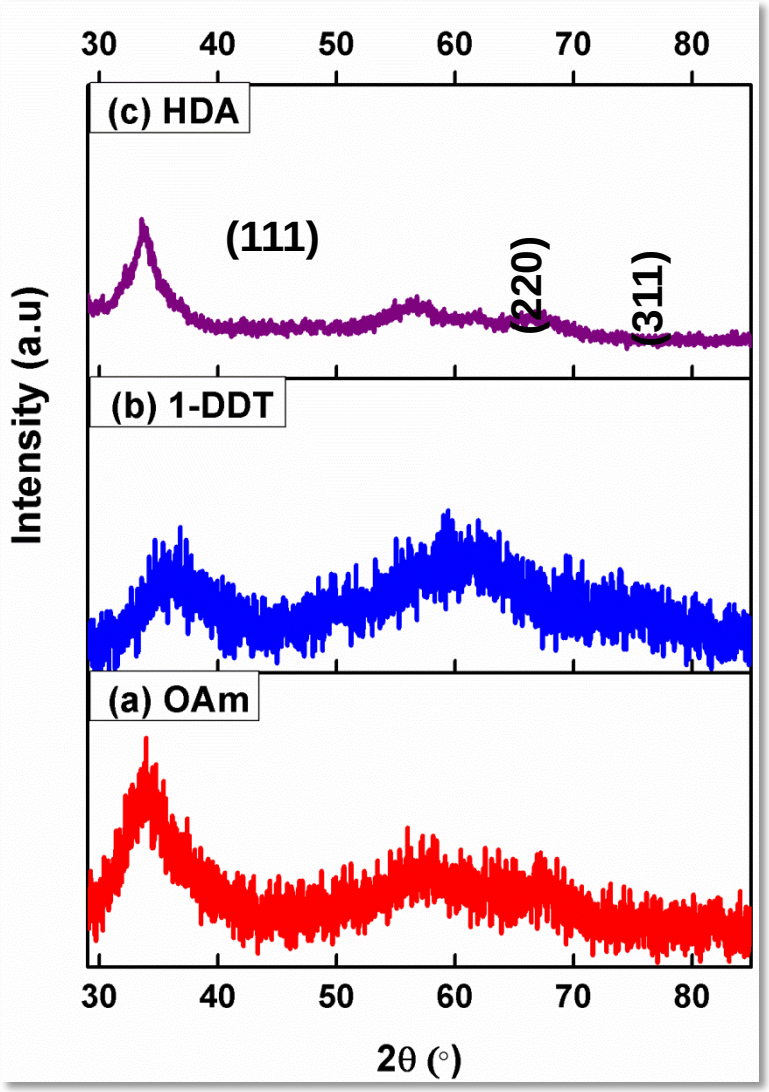


Figure 3.11: PXRD patterns of zinc sulfide nanoparticles collected from $Zn(ATU)_2$ in (a) OAm, (b) 1-DDT and (c) HDA after 20 minutes at 160 °C at a 2.5:15 ratio.

The TEM images displayed in Figure 3.12 showed that the nanoparticles were generally spherical when using the three different capping agents. The population in all the three samples was all fairly mono-dispersed. Evident from the micrographs, the HDA-synthesized particles were much larger and more well-defined and the 1-DDT gave the smallest nanoparticles in terms of size. The TEM results were well in agreement with the obtained XRD patterns (Figure 3.11) that showed narrow peaks for the HDA samples indicating a

higher degree of crystallinity and larger nanocrystals and much broader peaks from the DDT and OAm samples indicating much smaller particles in this regard.

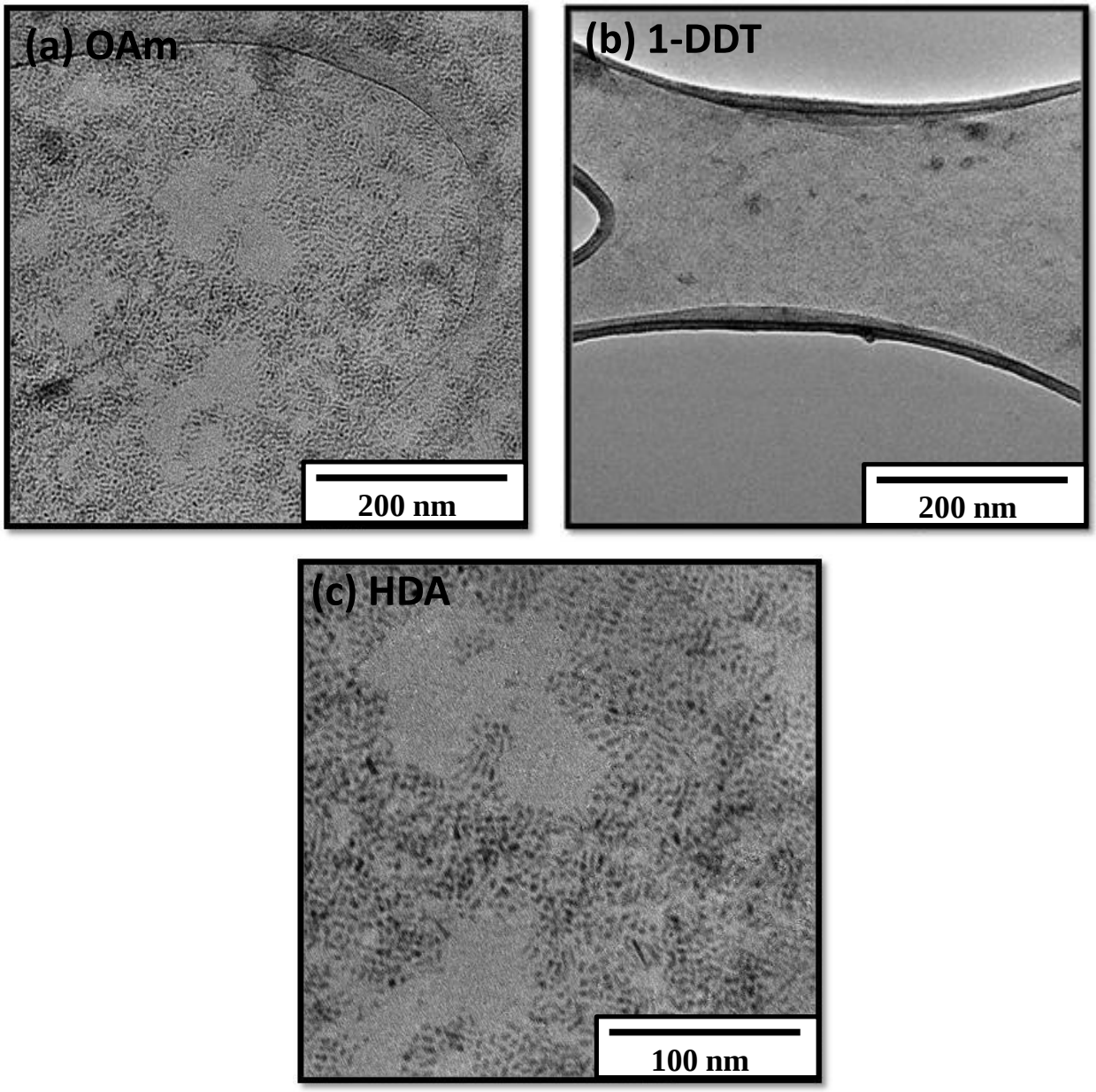


Figure 3.12: TEM micrographs of zinc sulfide nanoparticles from $Zn(ATU)_2$ in (a) OAm, (b) 1-DDT and (c) HDA after 20 minutes at 160 °C at a 2.5:15 ratio.

3.3.4.2. Optical properties

The optical absorption and photoluminescence spectra of the ZnS nanoparticles synthesized in OAm, 1-DDT, and HDA were assembled in Figures 3.13 (a) and (b), respectively and summarized in Table 3-8. The absorption curves showed that band edges of the samples

synthesized from OAm, 1-DDT and HDA were 310 nm, 308 nm and 313 nm, respectively. All band edges observed were blue-shifted from the bulk band edge of ZnS (340 nm) indicating strong quantum confinement effects and also confirming and consolidating data obtained from the XRD data (Figure 3.11) and TEM data (Figure 3.12). Particles synthesized from 1-DDT had the highest blue-shift which was attributed to smaller particles. The emission spectra in Figure 3.16 (b) showed that the peak due to OAm-capped nanoparticles was broad compared to the ones due to the DDT and HDA-capped particles (FWHM in Table 3-8). The broad peak indicated that the OAm-capped sample had a higher degree of poly-dispersity in their population; however, this was not visible in the TEM images (Figure 3.12), which showed that populations from all samples were mono-dispersed. Nevertheless, some particles did show some degree of elongation.

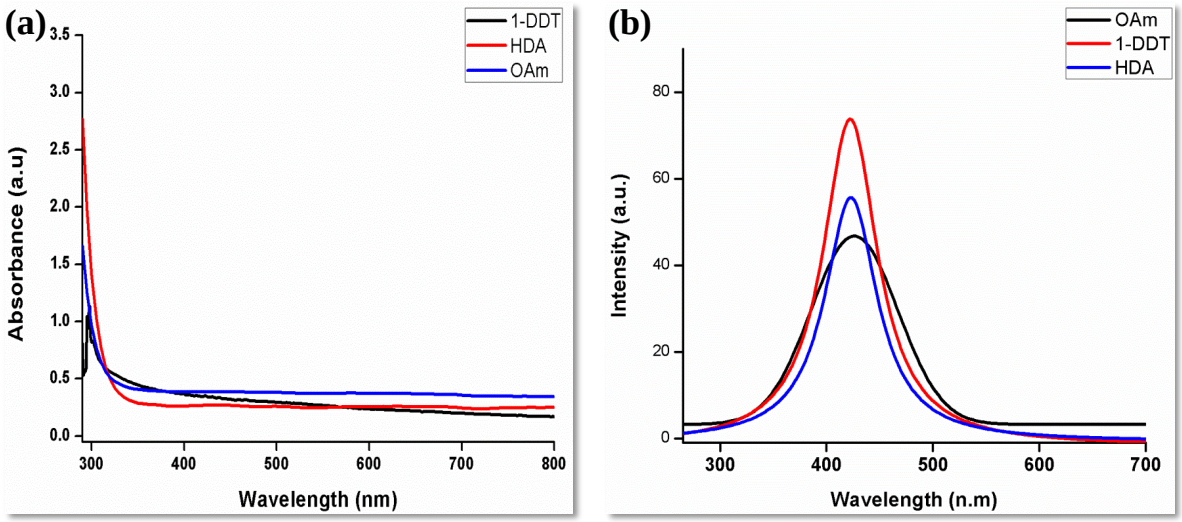


Figure 3.13: (a) Absorption and (b) emission spectra of zinc sulfide nanoparticles (λ_{exc}= 250 nm) collected from zinc(II) diethyl acyl thiourea at 160 °C for various capping agents (OAm, 1-DDT, and HDA)

Table 3-8: Optical Properties of ZnS nanocrystals of the capping agent experiments synthesized from $Zn(ATU)_2$

Capping agent	Band Edge (nm)	Emission max. (nm)	FWHM (nm)
OAm	310	410	78
1-DDT	308	410	52
HDA	313	410	53

Time and temperature tend to affect the sizes of nanocrystals through Ostwald ripening as stated earlier. The Ostwald ripening process is a thermodynamically driven spontaneous phenomenon where smaller particles re-dissolve and deposit on energetically more favorable larger particles.[9] Figure 3.14 shows size dependency of the nanoparticles to reaction parameters such time, temperature, concentration and the nature of the capping agent. It is no surprise that the particles sizes are mostly affected by time and temperature whilst a nearly linear trend is observed for the concentration and capping agent. The concentration and the nature of the capping agent tend to have a marked effect on the shapes of the nanocrystals, particularly if the reaction is under kinetic conditions. The kinetic growth regime is usually achieved at low reaction temperatures with higher monomer concentration.[20] The thermodynamic growth regime tends to produce isotropic nanocrystals such as spheres whereas the kinetic growth regime would produce anisotropic nanocrystals such as rods.[20,21] The chemisorption of the capping agent on the nanocrystal surface can also determine the resultant morphology. The growth of the nanocrystal can be hindered on the chemisorbed face hence resulting in directed crystal growth. Hexadecylamine, for instance, has been shown to adsorb preferentially on the (100) crystallographic plane hence resulting in the formation of nanorods.[22] Whilst needle-like morphologies have been observed in this study, it must be noted that their aspect ratios are quite small hence they constitute isotropic growth with 3D confinement similar to spheres. Therefore, thermodynamic conditions are evidently more prominent, consequently, the constant trend seen for concentration and capping agent curves.

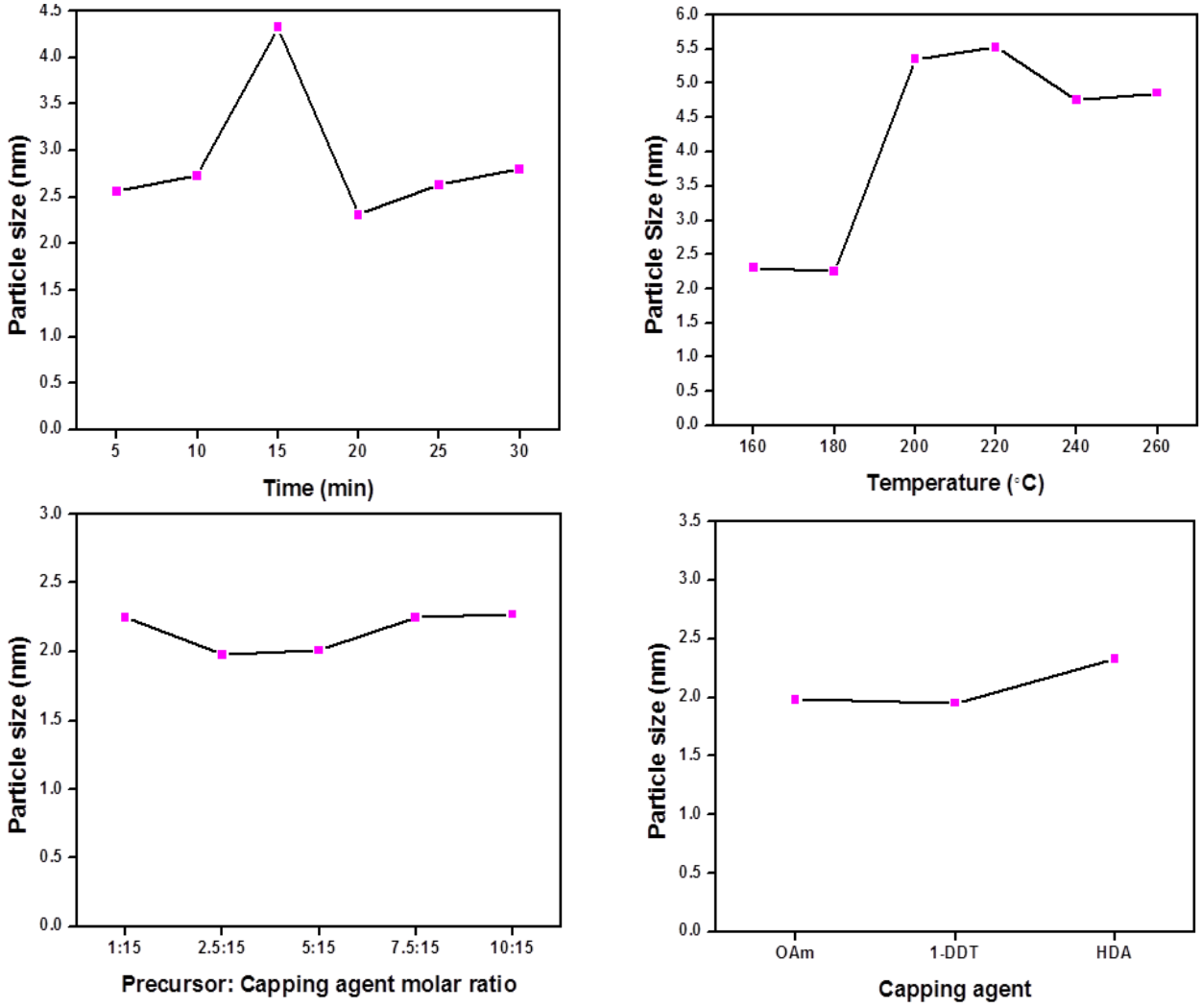


Figure 3.14: Size trends of the nanoparticles extracted from XRD using the Scherrer equation as a function of varying reaction conditions

As the time is increased from 5 to 15 min, there is an increase in particle sizes, a trend that is readily observed in colloidal synthesis. As the time is prolonged to 20 min, a sharp decrease in particle size is observed and thereafter a steady growth is observed from 25 to 30 min. The growth of the nanocrystals can generally be divided into two stages. The first stage being the burst nucleation followed by diffusional growth.[23] The nuclei form from a supersaturated solution of monomers. Over time, these nuclei can grow due to the Ostwald ripening process through diffusion hence resulting in an increase in particle sizes. However, as the time proceeds, there is a decrease in monomer concentration, resulting in nuclei falling way below the supercritical sizes. This triggers another nucleation process with new nuclei forming and growing overtime.[18] This therefore results in separate size distributions which can be extracted over time as seen in this case. Temperature can also be used to control the size of

the resultant nanocrystal. At higher temperatures, the reaction is thermodynamically driven. This therefore translates in such a manner that as the temperature of the reaction increases, there is an increase in disorder. To overcome this disorder, the particles tend to coagulate together and form bigger, stable particles.[24] Hence the increase in particle sizes at 200 °C. As the temperature is increased further, the average kinetic energy of the reaction is supposed to increase, however, due to the bigger particle sizes, there is a slight decrease in kinetic energy, thereby resulting in a minor increase in the particle sizes. The particles synthesized at 240 °C and above show a slight decrease in sizes; this is probably due to the increase in the rate of nucleation and diffusion which result in smaller nuclei.

3.4. Conclusions

Relatively small nanoparticles were obtained from the thermolysis of $Zn(ATU)_2$. Even with the varied reaction conditions, the production of ZnS nanoparticles were favoured over the ZnO nanoparticles. This can be attributed to the electron-rich nitrogen atom bonded to the thiocarbonyl and the ethyl groups; the electron-rich nitrogen atom has the potential to donate its electrons to the thiocarbonyl bond, resulting in a stronger bond between the Zn and the S hence favouring the formation of ZnS. The influence of the time, temperature, precursor concentration, and capping environments as parameters affecting the morphology and size of the nanoparticles were investigated. It was observed that with the increase in time, particle sizes increased while increasing the temperature had an influence on both the morphology and the particle sizes. The morphology of the particles evolved from needle-like to an undefined morphology and proceeded to become spherically shaped particles, while the particle sizes increased with the undefined morphology and decreased with the spherical particles. An increase in precursor concentration showed the evidence of increasing agglomeration of the particles whilst the capping environment had an impact on the particle sizes and the phase of the ZnS.

3.5. References

1. Wang P., Huang B., Zhang X., Qin X., Jin H., Dai Y., Wang Z., Jiyong Wei, Zhan J., Wang S. & Wang J. Highly efficient visible-light plasmonic photocatalyst Ag@AgBr. *Chem. - A Eur. J.* **15,** 1821–1824 (2009).
2. Hoffmann M. R., Martin S. & Choi W. B. Environmental Applications of Semiconductor Photocatalysis. *Chem. Rev.* **1,** 69–96 (1995).

3. Zegeye D. Z. Photocatalytic activity of N-doped ZnS nanoparticles for degradation of organic pollutant (methylene blue). *J. Photochem. Photobiol.* **5,** 214–219 (2016).
4. Sharma M., Singh S. & Pandey O. P. Photocatalytic degradation of organic dyes under UV-Visible light using capped ZnS nanoparticles. *Sol. Energy* **86,** 626–633 (2012).
5. Herrmann J. M. Heterogeneous photocatalysis: an emerging discipline involving multiphase systems. *Catal. Today* **24,** 157–164 (1995).
6. Govindraju S., Kalenga M.P., Airo M., Moloto M.J., Sikhwivhilu L.M., Moloto N. Size quantization in Cu_2Se nanocrystals. *Opt. Mater. (Amst).* **1,** 310–313 (2014).
7. Saeed S., Rashid N. & Woollins J. D. Growth and characterization of semiconducting nickel sulfide nanocrystals from air-stable single-source metal organic precursors. *Cogent Chem.* **15,** 103–195 (2015).
8. Bruce J. Single source precursors for the synthesis of semiconducting quantum dots. (2008).
9. Wageh S., Ling Z. S. & Xu-Rong X. Growth and optical properties of colloidal ZnS nanoparticles. *J. Cryst. Growth* **255,** 332–337 (2003).
10. Voorhees P. W. The theory of Ostwald ripening. *J. Stat. Phys.* **1,** 231–252 (1985).
11. Moloto M. J., Revaprasadu N.,O'Brien P. & Malik M. N-alkylthioureacadmium (II) complexes as novel precursors for the synthesis of CdS nanoparticles. *J. Mater. Sci. Mater. Electron.* **1,** 313–316 (2004).
12. Kowalczyk B., Kyle J., Bishop M., Lagzi I., Wang D., Wei Y. & Han S. Charged nanoparticles as supramolecular surfactants for controlling the growth and stability of microcrystals. *Nat. Mater.* **11,** 227–232 (2012).
13. Moloto N. Synthesis, properties and applications of Mn, Co, Ni and Cu chalcogenide nanoparticles. (2009).
14. Jiang X. C., Chen W. M., Chen C. Y. & Xiong S. X. Role of temperature in the growth of silver nanoparticles through a synergetic reduction approach. *Nanoscale Res. Lett.* **6,** 1–9 (2011).
15. Mann I., Meyer-Vernet N. *Nanodust in the Solar System: Discoveries and Interpretations*. (2012).
16. Khaleduzzaman S. S., Mahbubul I. M., Shahrul I. M. & Saidur R. Effect of particle concentration, temperature and surfactant on surface tension of nanofluids. *Int. Commun. Heat Mass Transf.* **49,** 110–114 (2013).
17. Bhuiyan M. H. U., Saidur R., Amalina M. A., Mostafizur R. M. & Islam, A. Effect of nanoparticles concentration and their sizes on surface tension of nanofluids. *Procedia*

Eng. **105,** 431–437 (2015).

18. Marqusee J.A.Theory of Ostwald ripening: Competitive growth and its dependence on volume fraction. *J. Chem. Phys.* **1,** 536–550 (1984).
19. Niu Z. & Li Y. Removal and utilization of capping agents in nanocatalysis. *Chem. Mater.* **26,** 72–83 (2014).
20. Peng X., Manna L., Yang W., Wickham J., Scher E., Kadavanich A. Shape control of CdSe nanocrystals. *Nature* **404,** 59–61 (2000).
21. Hu J., Li L., Yang W., Manna L. & Wang L. Linearly polarized emission from colloidal semiconductor quantum rods. *Science* **292,** 2060–3 (2001).
22. Mourdikoudis S. & Liz-Marzán L. M. Oleyamine in Nanoparticle Synthesis. *Chem. Mater.* **25,** 1465–1476 (2013).
23. Robb D. T. & Privman V. Model of nanocrystal formation in solution by burst nucleation and diffusional growth. *Langmuir* 1–10 (2007).
24. Stanley H. E., Family F. & Gould H. Kinetics of aggregation and gelation. *J. Polym. Sci. Polym. Symp.* **73,** 19–37 (1985).

Chapter 4: Synthesis and Characterization of ZnS nanocrystals from the $Zn(TU)_2Cl_2$ complex

4.1. Introduction

Thiourea (Figure 4.1a) and thiourea derivatives (Figure 4.1b) show diverse coordination possibilities due to their conformational isomerism, their stearic effects and the presence of multiple donor sites on their derivatives and intramolecular interactions.[1] In addition, their ability to coordinate to a range of metal centres as either neutral ligands[2], monoanions[3] and dianions[4] make them an interesting focus. Their ease of synthesis and ready modification of the substituents on the nitrogen have rendered them previously quite fascinating. Recent studies however, are more interested in the preferential coordination through the sulphur donor atom instead of the nitrogen during complex formation, making these complexes easy targets of sulphur sources in the synthesis of metal sulfides.

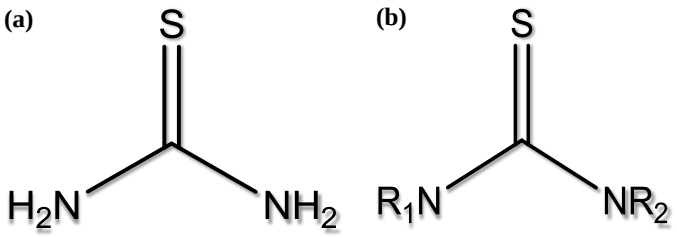


Figure 4.1: **The structure of (a) thiourea and (b) a general structure of substituted thiourea ligands.**

There have been many studies on thiourea and substituted thiourea coordinated to metals through sulphur. Amongst several studies, Rosenheim and Meyer[5] have described the coordination of Fe (II) with thiourea and found that the complex formed through the sulphur donor atom. In their long-standing research, Moloto *et al.*[6,7] have also reported on a series of N-alkyl substituted thioureas coordinating to metals that include lead, copper and cadmium. In their work, they made use of the thioureas and their constituents for the preparation of metal sulfides through thermal decomposition of the corresponding complex. They are

primarily used as sulphur sources in complexes because their advantages in this regard are that they are fairly easy to synthesize, stable for long periods and yield good quality semiconductor nanocrystals.

Semiconductor nanocrystals act as good photocatalysts in the application of photocatalysis. Although not well-studied, zinc sulphide has been identified as a potentially good photocatalyst. It is a wide-bandgap material with a band edge of 340 nm[8], because of this wide bandgap light absorption is only limited to the UV region. In the previous chapter, bis (N,N-diethyl-N'-benzoylthiourea)Zn(II) ($Zn(ATU)_2$) was used as a single source precursor to synthesize the metal chalcogenides. From the study, we discovered that even though the metal was coordinated to both an oxygen and sulphur atoms, ZnS was the preferred product under all the varied conditions. In this chapter, our interest is to investigate whether a precursor with only one sulphur would yield better quality zinc sulfide nanoparticles by using the thiourea zinc (II) complex ($Zn(TU)_2Cl_2$) as a single-source precursor which is shown in Figure 4.2. In the attempt to modify and optimize the properties, effect of temperature, precursor concentration and capping agent were investigated.

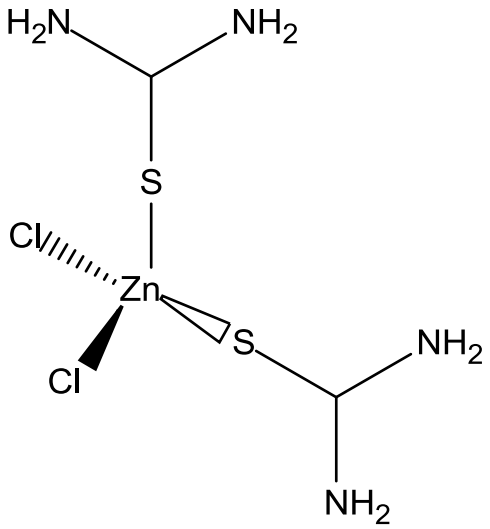


Figure 4.2: A structure of $Zn(TU)_2Cl_2$.

4.2. Experimental procedure

4.2.1. Chemicals

OAm (Oleylamine), 1-DDT (dodecanethiol), TOPO (tri-n-octylphosphine oxide), HDA (hexadecylamine) and TOP (trioctylphosphine) were purchased from Sigma Aldrich. Toluene, ethanol, acetone and methanol were obtained from Kemical. Thiourea was (analytical grade) obtained from Sigma Aldrich, were used as purchased to prepare the precursors.

4.2.2. Synthesis of ZnS nanoparticles using the $Zn(TU)_2Cl_2$ complex as a single-source precursor

In a typical experiment, OAm (5.70 ml) was injected in a clean 3-neck round bottom flask and heated to 160 °C. 0.2510 g of the precursor was quantitatively transferred to the hot OAm and a slight decrease in temperature of the solution by 5 – 10 °C was observed. The solution was allowed to stabilize at 160 °C and heated for 20 minutes at that temperature. The reaction was terminated and the resulting solution was allowed to cool to 70 °C methanol was added to form a white precipitate. The precipitate was separated from the mother liquor by centrifugation and the particles were washed several times with methanol, and then air-dried to yield OAm-capped ZnS nanoparticles. The synthesis time of the ZnS nanoparticles was obtained from Chapter 4, where the effect of time on the properties of the nanoparticles was studied and confirmed that even though there was no significant effect, the optimal synthesis time for these types of reactions is 20 minutes. Furthermore, the effect of temperature, precursor concentration and capping agents were studied but only the extreme conditions were considered as this the full studies had been carried out in Chapter 4. Temperature reactions were summarized in Table 4-1, Precursor concentration and coordinating solvents reactions were summarized in Tables 4-2 and 4-3, respectively.

Table 4-1: Reaction parameters for temperature experiments

Samples	Precursor: capping agent molar ratio	Temperature	Time (min)	Coordinating solvent
A_1	1:15	160 °C	20	OAm
A_2	1:15	200 °C	20	OAm
A_3	1:15	260 °C	20	OAm

Table 4-2: Reaction parameters for the precursor: capping agent molar ratio experiments

Samples	Precursor: capping agent molar ratio	Temperature	Time	Coordinating solvent
A_1	1:15	160 °C	20 min	OAm
B_1	2.5:15	160 °C	20 min	OAm
B_2	5:15	160 °C	20 min	OAm
B_3	7.5:15	160 °C	20 min	OAm
B_4	10:15	160 °C	20 min	OAm

Table 4-3: Reaction parameters for the coordinating solvent experiments

Samples	Precursor: capping agent molar ratio	Temperature	Time	Coordinating solvent
B_1	2.5:15	160 °C	20 min	OAm
C_1	2.5:15	160 °C	20 min	HDA
C_2	2.5:15	160 °C	20 min	1-DDT

4.2.3. Characterisation Techniques

4.2.3.1. Optical characterization

The optical properties of the materials were determined by placing the toluene dispersion of the nanoparticles into quartz cuvettes (1 cm path length). A Perkin Elmer Lambda 75S UV–Vis–NIR Spectrophotometer and an Analytica Jena Specord 5D UV-Vis Spectrophotometer were used to carry out the optical measurements. A Perkin Elmer LS55 with a xenon lamp

(150 W) and a 152 P photo multiplier tube as a detector were used to measure the photoluminescence of the particles.

4.2.3.2. Electron microscopy

The Transmission Electron Microscopy (TEM) images were obtained using a Technai G2 TEM Spirit operated at 200 kV. The samples were prepared by placing a drop of a dilute solution of sample in toluene onto the carbon-coated copper grids. The samples were allowed to dry completely at room temperature.

4.2.3.3. Powder X-Ray diffraction

X-Ray diffraction (XRD) patterns on powdered samples were measured on Bruker D2 Phaser desktop diffractometer equipped with a LYNXEYE PSD detector (set to measure a 5° 2θ angular range), 2.5° primary and secondary beam Soller slits, and Co X-ray micro-source (Kα with λ = 1.78897 Å) operated at 30 kV and 10 mA. The goniometer radius of the diffractometer was 70.7 mm. The instrument was also fitted with a secondary beam Fe filter to attenuate Kβ radiation and a 3 mm air-scatter slit. Diffraction data were collected in the 2θ range 10-90° in 0.0260° steps and at a count time of 0.5 sec/step. Particle sizes were estimated using the Scherrer equation. (Equation 4.1)

$$\tau = \frac{K\,\lambda}{\beta\,Cos\,\theta}$$

where:

- τ is the mean size of the ordered (crystalline) domains.
- K is a dimensionless shape factor, with a value close to unity. The shape factor has a typical value of about 0.9, but varies with the actual shape of the crystallite.
- λ is the X-ray wavelength.
- β is the line broadening at half the maximum intensity (FWHM), after subtracting the instrumental line broadening, in radians.
- θ is the Bragg angle (in degrees).

4.3. Results and discussion

4.3.1. Temperature effects on the nanoparticles using $Zn(TU)_2Cl_2$ as a single-source precursor method

4.3.1.1. Structural properties

Having established in the previous chapter that temperature plays an inherent role in the synthesis of zinc sulfide nanoparticles, the effect of temperature in synthesizing ZnS nanoparticles when using $Zn(TU)_2Cl_2$ as a single-source precursor was investigated. In this section, three temperatures were taken into account 160 °C, 200 °C and 260 °C, in order to monitor temperature effects on the resulting nanoparticles. XRD diffractograms were obtained for samples across all temperatures so as to confirm the synthesis of the nanoparticles, their phases and their crystallinity. Figure 4.3 displays XRD patterns obtained at different temperatures, the p-XRD patterns of the synthesized nanoparticles confirmed the synthesis of ZnS nanoparticles and that samples obtained at each temperature corresponded to cubic ZnS (JCPDS card: 01-077-2414). Evident from Figure 4.3(a) are the broad peaks for the samples synthesized at 160 °C, this was an indication of the small nature of the samples at this temperature. Increasing the temperature, the peaks became sharper indicating the growth of the nanoparticles and the improving crystallinity of the samples. Average nanoparticle sizes were calculated using the Scherrer equation, nanoparticle sizes were 1.95 nm, 2.11 nm and 4.01 nm for samples synthesized at 160 °C, 200 °C and 260 °C, respectively. The growth process was consistent with Ostwald's ripening, unlike in Chapter 4, where nanoparticles went through the fusion growth process. The Ostwald's ripening effect is a readily observed trend in the synthesis of nanoparticles.[9]

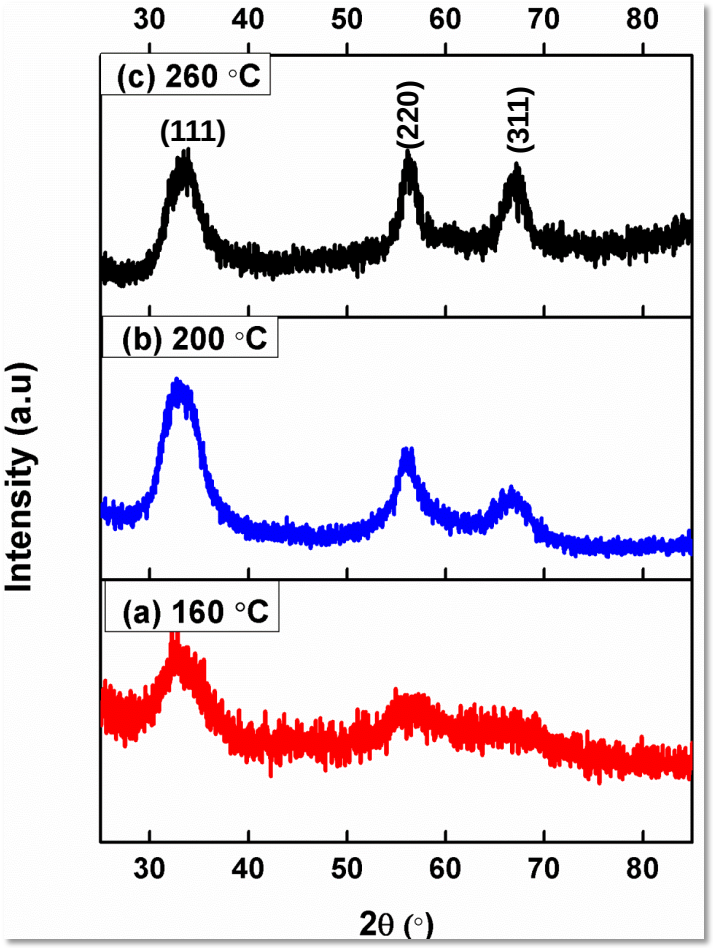


Figure 4.3: **PXRD patterns of zinc sulfide nanoparticles collected from $Zn(TU)_2Cl_2$ at (a) 160 °C, (b) 200 °C and (c) 260 °C.**

TEM micrographs obtained for samples at different temperatures are displayed in Figure 4.4. The TEM images obtained show that nanoparticle sizes steadily increased with increasing temperature. The morphology of the nanoparticles across all temperatures seemed to be a mixture of spherical and triangular particles. The obtained images were in good agreement with the results drawn from the XRD patterns.

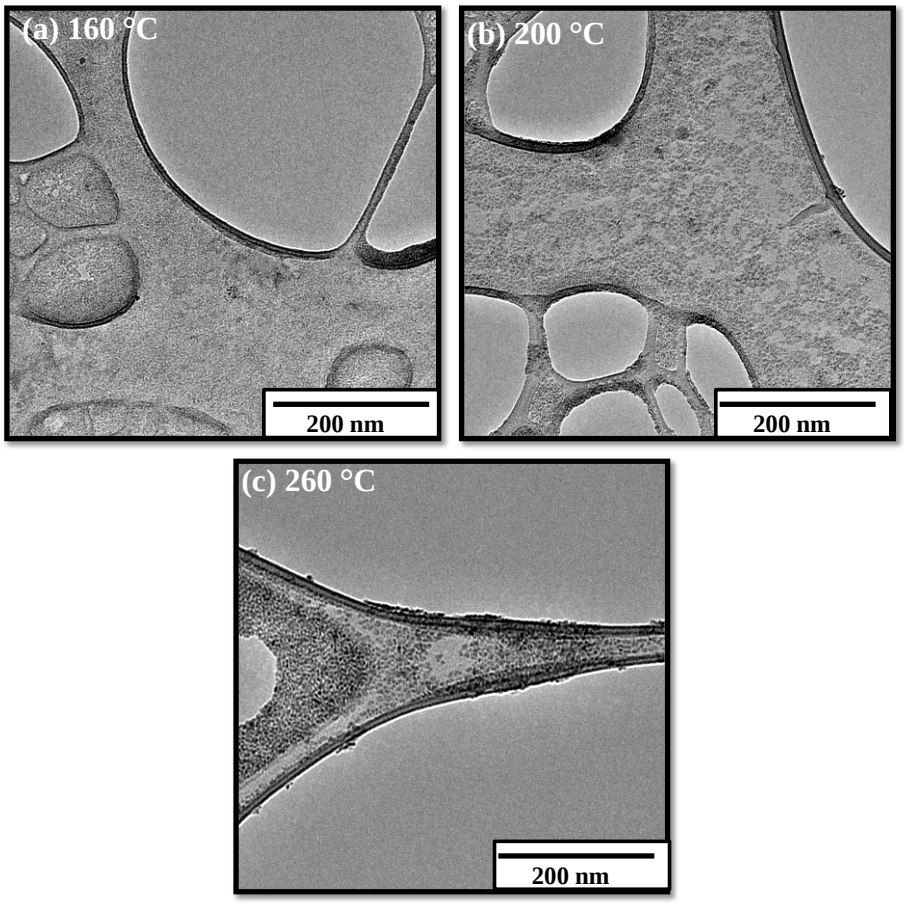


Figure 4.4: TEM micrographs of zinc sulfide nanoparticles collected from $Zn(TU)_2Cl_2$ at (a) 160 °C, (b) 200 °C and (c) 260 °C.

4.3.1.2. Optical properties

The optical properties of particles prepared at different temperatures are shown in Figure 4.5 and summarized in Table 4-4. The band edges of the nanoparticles were all blue-shifted from the bulk ZnS, indicating that nanoparticles were in nano-size regime. The absorption spectra of samples synthesized from 160 °C to 260 °C have band-edges of 312 nm, 318 nm and 348 nm respectively. The increasing band-edges as temperature was increased was indicative of increasing nanoparticle sizes, this was consistent with information obtained from TEM and XRD. The emission maxima of particles across all temperatures were red-shifted from their corresponding absorption band edges, this is attributed to quantum confinement effects.[10] The FWHM of the photoluminescence peaks can be an indication of the size distribution of the nanoparticles,[11] polydispersity in nanoparticles is generally characterized with a FWHM greater than 90 nm.[11] The FWHM of nanoparticles obtained at 160 °C, 200 °C and 260 °C were 89 nm, 62 nm and 50 nm, respectively. A notable trend in the size distribution of the

nanoparticles is that increasing the temperature, results in the increased degree of monodispersity, a similar pattern has been reported in the previous Chapter.

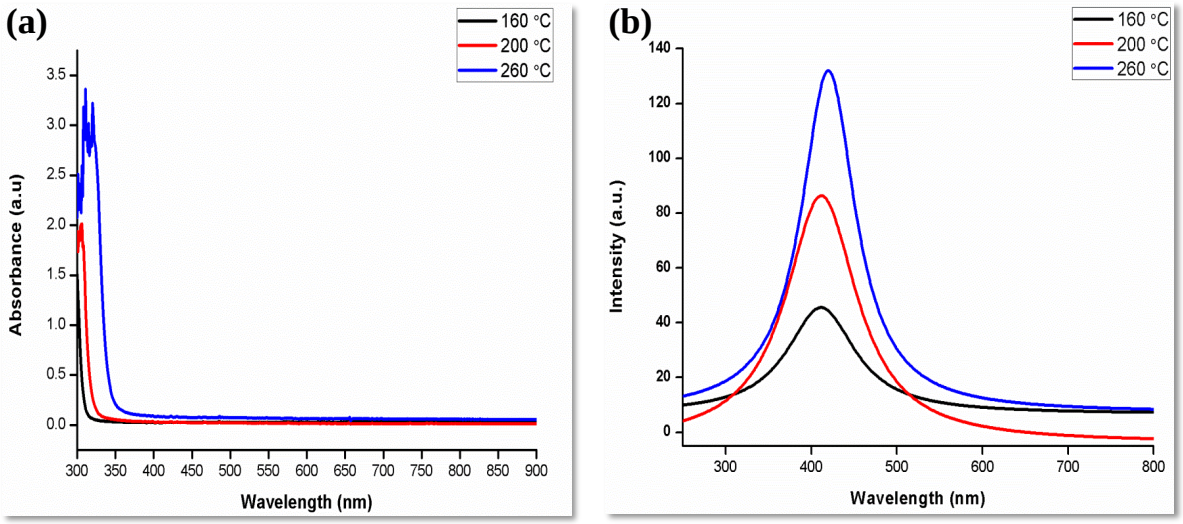


Figure 4.5: (a) Absorption and (b) Emission spectra of zinc sulfide nanoparticles collected from $Zn(TU)_2Cl_2$ at different temperatures.

Table 4-4: Optical properties of ZnS nanocrystals of the temperature experiments synthesized from $Zn(TU)_2Cl_2$

Temperature (°C)	Band Edge (nm)	Emission max. (nm)	FWHM (nm)
160	312	410	75
200	318	413	62
260	348	415	50

4.3.2. Precursor concentration effects on the nanoparticles using TU as a single-source precursor method

4.3.2.1. Structural properties

From the results obtained from the temperature study, 200 °C was identified as the most favourable temperature to continue studies on how increasing the precursor concentration would affect the properties of ZnS. At this temperature, nanoparticles were fairly small, crystalline and mono-dispersed, displaying better quality over the 160 °C and 260 °C nanoparticles. At 200 °C, the concentration used was a 1:15 $Zn(TU)_2Cl_2$:OAm ratio, the

$Zn(TU)_2Cl_2$ concentration was further increased to 2.5:15, 5:15, 7.5:15 and 10:15 ratios. XRD diffractograms of the nanoparticles synthesized accordingly were assembled in Figure 4.6. Samples across all concentrations were indexed to a cubic ZnS phase (JCPDS card: 01-077-2414). The XRD peaks of the 1:15 sample are sharp and well-defined, increasing the concentration to 2.5:15 led to broader peaks and each time the concentration was increased, peaks seemed to broaden even further, this was an indication that nanoparticles became smaller and smaller with increasing concentration. Using the Scherrer equation, average sizes were 2.11 nm for the 1:15 sample as previously calculated, 2.01 nm for the 2.5:15 sample, 1.81 nm for 5:15, 1.41 nm and 1.61 nm for the 7.5:15 and 10:15 ratios, respectively.

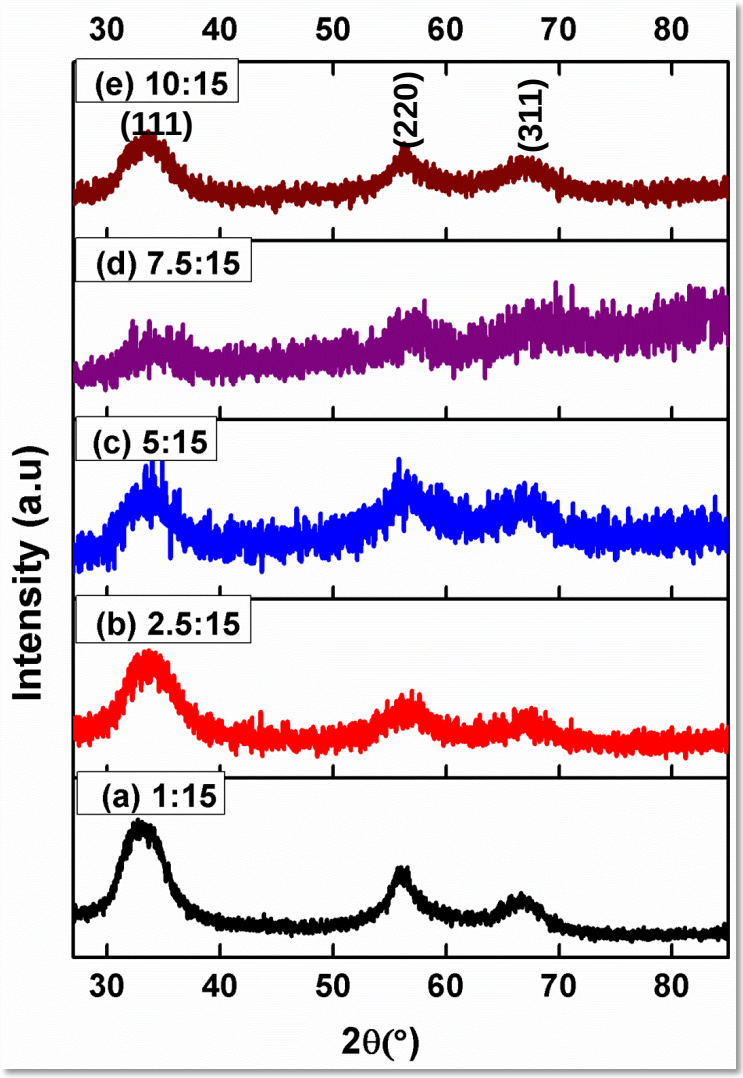


Figure 4.6: **PXRD patterns of zinc sulfide nanoparticles collected from $Zn(TU)_2Cl_2$ at different precursor concentrations.**

The TEM images of the synthesized nanoparticles are shown in Figure 4.7. The spherical morphologies of the nanoparticles remained consistent across all concentrations. Increasing the precursor concentration ultimately results in the agglomeration of the nanoparticles, this behaviour is commonly spotted when increasing precursor concentrations in nanoparticle synthesis.[12] It has been concluded that this is due to the fact that as the volume fractions increases, the addition of nanoparticles increases concurrently and then the surface tension of the nanoparticle solution increases consequently, hence resulting in nanoparticles agglomerating.[13]

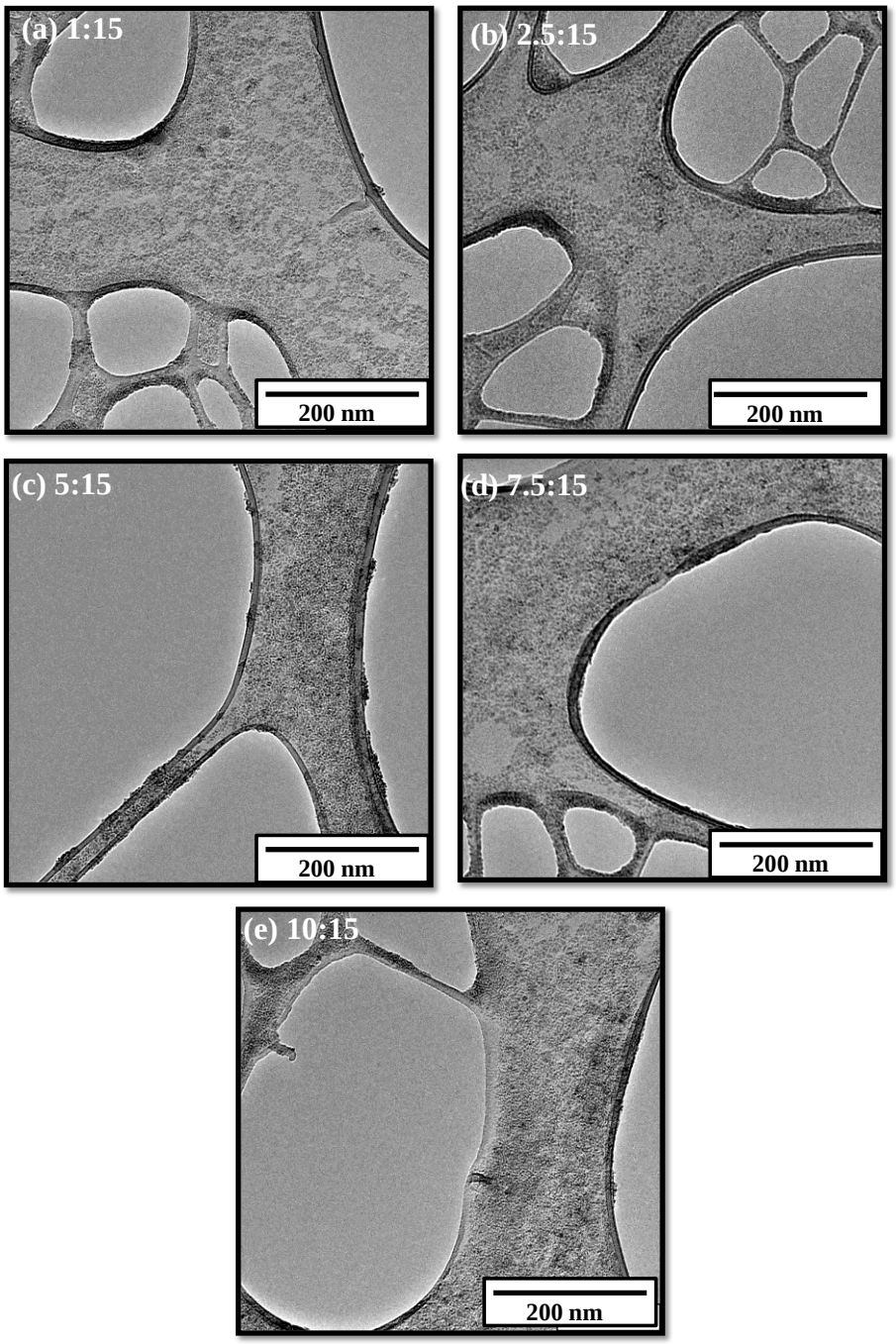


Figure 4.7: TEM micrographs of zinc sulfide nanoparticles collected from $Zn(TU)_2Cl_2$ at (a) 1:15, (b) 2.5:15, (c) 5:15, (d) 7.5:15 and (e) 10:15 precursor to capping agent molar ratios.

4.3.2.2. Optical properties

The absorption and emission spectra of the different concentration samples are displayed in Figure 4.8 and summarized in Table 4-5. The band edges of the samples were all blue-shifted from bulk ZnS. The band edge of the particles started by decreasing when concentration was

increased to 2.5:15, however, further increasing the precursor concentration resulted in the increase of the band edge which indicated that nanoparticles sizes were increasing when the precursor concentration was increased. The results obtained were not in agreement with the data obtained in XRD and TEM. The emission spectra of the ZnS nanoparticles synthesized show that nanoparticle size distribution was fairly monodispersed at all concentrations. Even though the emission peak of the 2.5:15 sample is wider compared to the rest of the samples, indicating a lower degree of polydispersity, the FWHM of the sample is still well below a 100 nm. From these results, the 2.5:15 samples were deemed optimal due their creditable optical and structural properties and consequently used for capping agent studies.

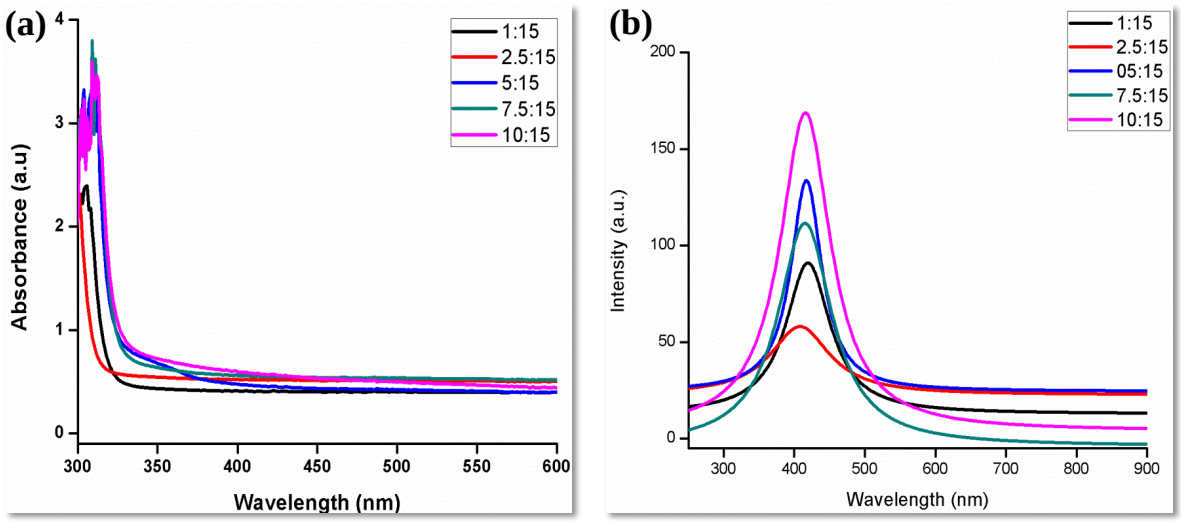


Figure 4.8: (a) Absorption and (b) Emission spectra of zinc sulfide nanoparticles collected from $Zn(TU)_2Cl_2$ at different precursor concentrations.

Table 4-5: Optical Properties of ZnS nanocrystals of the concentration experiments synthesized from $Zn(TU)_2Cl_2$

[Precursor]: [capping agent]	Band Edge (nm)	Emission max. (nm)	FWHM (nm)
1:15	318	410	62
2.5:15	310	400	74

5:15	324	410	62
7.5:15	324	410	62
10:15	331	410	65

4.3.3. Capping agent effects on the nanoparticles using TU as a single-source precursor method

4.3.3.1. Structural properties of the oleylamine capped ZnS

Using specific capping agents has been reported to significantly reduce nanoparticle sizes and consequently contribute to their stability.[14] The mechanisms is reported to proceed through the formation of strong covalent bonds between the capping agent and the surfaces of the nanoparticles that is responsible for stearic hindrance by which nanoparticles remain stable for long periods of time.[15] Interestingly, the sizes of nanoparticles have also been found to be inversely proportional to their reactivity and hence resulting in the enhancement of photocatalytic activities.[16] For these reasons, the effect of OAm, 1-DDT and HDA have been investigated in the synthesis of the ZnS nanoparticles and the XRD diffractograms have been assembled in Figure 4.9. The XRD of the nanoparticles were indexed to cubic ZnS in accordance with JCPDS card: 01-077-2414. The HDA-capped nanoparticles yielded broad XRD peaks indicating that nanoparticles were small while the OAm- and DDT-capped particles gave sharp XRD peaks indicating well-crystallized particles but larger in size. As discussed in the previous section (Section 4.3.2.), the average sizes of the OAm-capped nanoparticles as calculated by the Scherrer equation was 2.01 nm, while the DDT- and HDA-capped particles were around 2.03 nm and 1.95 nm, respectively.

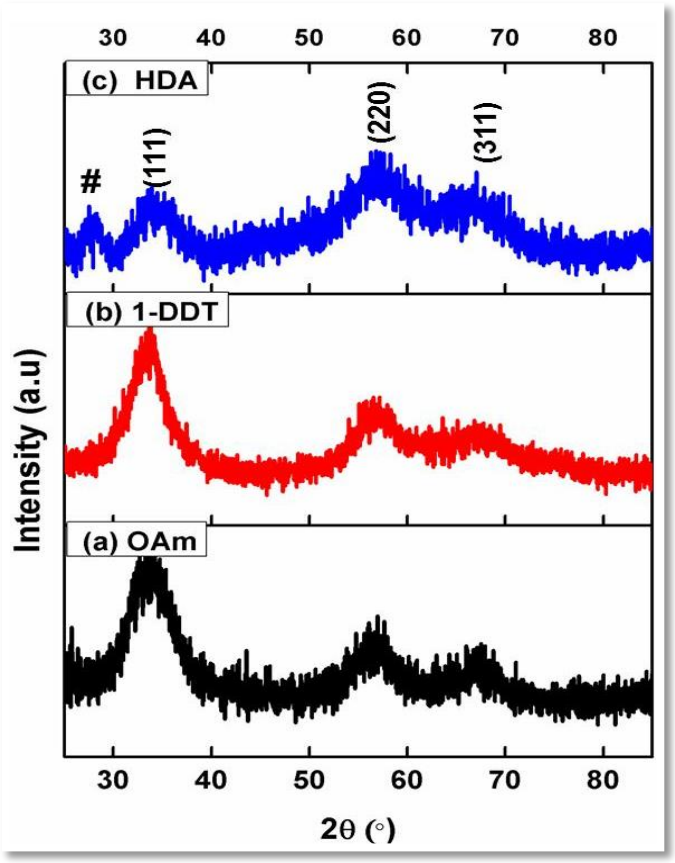


Figure 4.9: PXRD patterns of zinc sulfide nanoparticles collected from $Zn(TU)_2Cl_2$ at different precursor concentrations.

The TEM images of the particles capped with different surfactants are shown in Figure 4.10. The morphology of OAm capped nanoparticles were as previously mentioned a mixture of spherical and triangular shaped. The 1-DDT and HDA capped nanoparticles showed spherical morphologies and some agglomeration of ZnS nanoparticles was consistent in all surfactants. Size distribution in the obtained samples was difficult to comment due to the agglomeration and the small nature of the particles as a result, photoluminescence spectroscopy (Figure 4.11(b)) was used as an indicator of size distribution.

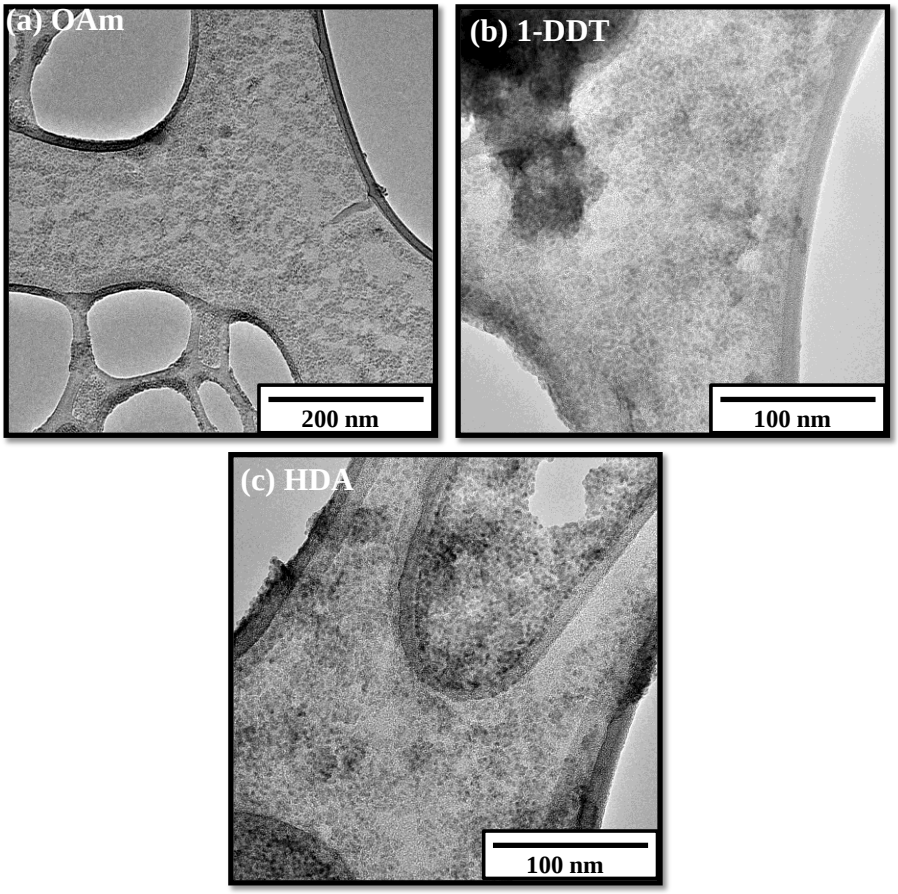


Figure 4.10: TEM micrographs of zinc sulfide nanoparticles collected from $Zn(TU)_2Cl_2$ in (a) OAm, (b) 1-DDT and (c) HDA.

4.3.3.2. Optical properties

The optical properties of the synthesized zinc sulfide nanoparticles are shown in Figure 4.11 and summarized in Table 4.6. All band edges were blue-shifted from the bulk band edge of 340 nm. Consistent with XRD, the absorption curves showed that the HDA-capped particles were most blue-shifted with a band edge of 305 nm, suggesting that nanoparticles synthesized in this regard were the smallest. As previously discussed, nanoparticles synthesized from OAm had a band edge of 310 nm which was similar to the band-edge of the DDT-capped particles. The absorption curves of nanoparticles capped with OAm and DDT were slightly tailed indicating that particle distribution within these samples was almost poly-dispersed. The FWHM of the emission peaks however were well under a 100 nm, suggesting a fairly mono-dispersed sample distribution in all nanoparticle populations. From this study, HDA-capped nanoparticles seemed to yield best quality nanoparticles; hence they were used for photocatalysis testing to complete the study.

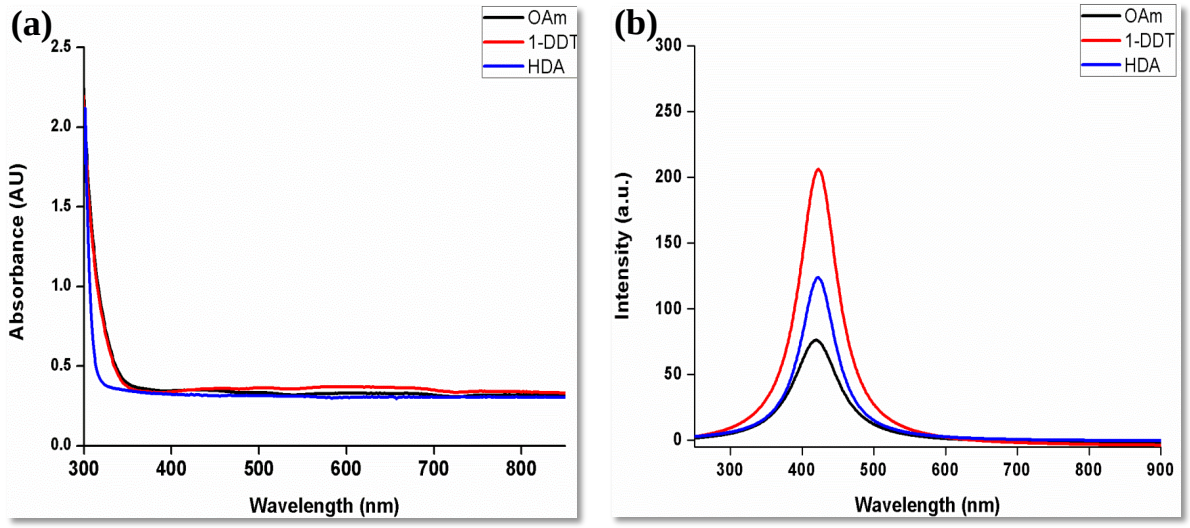


Figure 4.11: (a) Absorption and (b) Emission spectra of zinc sulfide nanoparticles collected from $Zn(TU)_2Cl_2$ at different capping agents

Table 4-6: Optical Properties of ZnS nanocrystals of the capping agent experiments synthesized from $Zn(TU)_2Cl_2$

Capping agent	Band Edge (nm)	Emission max. (nm)	FWHM (nm)
OAm	310	400	74
1-DDT	310	400	68
HDA	305	410	69

The effect of changing the reaction conditions on the resulting nanoparticles have been summarized in Figure 4.12, where the graphs show the particle size vs the reaction conditions. According to the particle size vs temperature graph, increasing temperature results in the successive growth of the nanoparticles, which is a similar trend observed in the previous chapter when $Zn(ATU)_2$ was used. These results were attributed to a mechanism based on Ostwald's ripening as previously discussed in which diffusion is followed by nucleation on the nucleating sites leading to the formation of larger nanoparticles.[17]

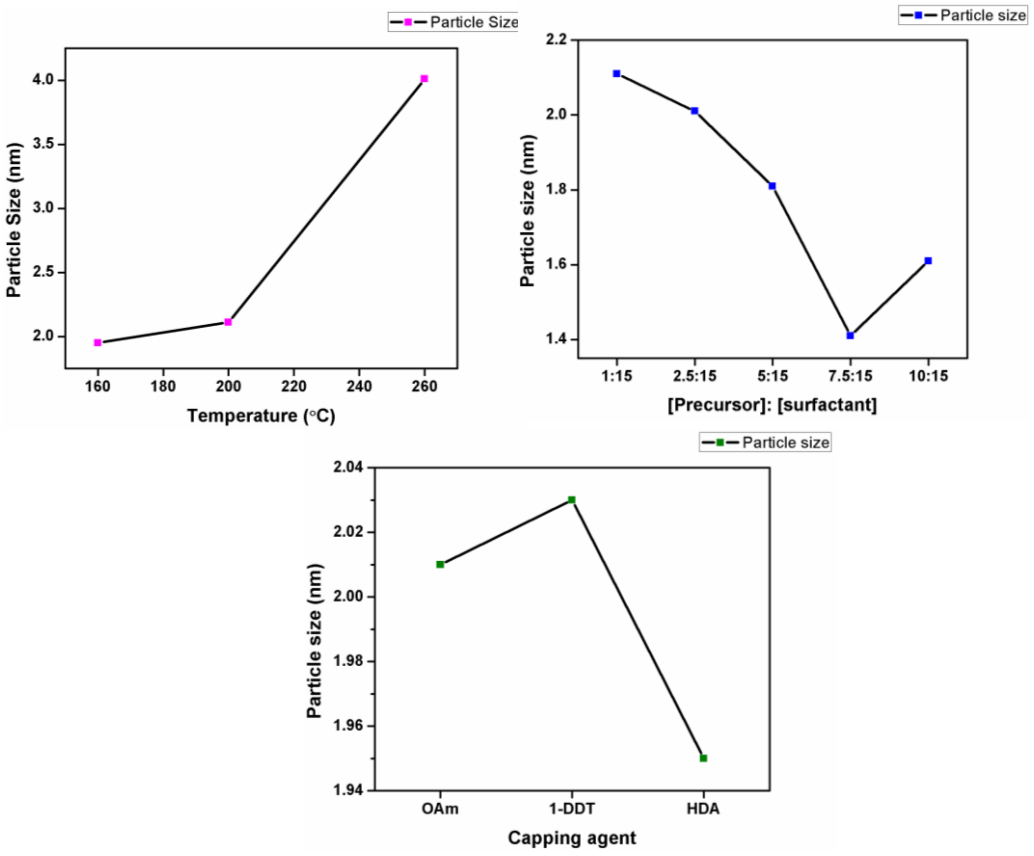


Figure 4.12: Size trends of the nanoparticles extracted from XRD using the Scherrer equation as a function of varying reaction conditions.

The size dependency of the nanoparticles on increasing precursor concentration as depicted in Figure 4.12 revealed a decrease of the particle sizes until 7.5:15 and was followed by an increase when the concentration was further increased to 10:15. The increase in precursor concentration results in a reduced mean spacing between the molecules and nanoparticles,[13] which results in faster nanoparticle adsorption and leading to slower crystal growth.[12] After nucleation and growth, the average particle size and size distribution may change by aging.[18]

4.4. Conclusions

The $Zn(TU)_2Cl_2$ complex was successfully used as single-source precursor for the preparation of zinc sulfide nanoparticles. Temperature studies revealed that the most preferred temperature when synthesizing nanoparticles in this chapter as 200 ºC. At this temperature, nanoparticles were fairly small, crystalline and mono-dispersed. When varying

capping agents in this chapter, the HDA-capped nanoparticles yielded the smallest nanoparticles. Capping agents typically play crucial roles in the particle size and size distribution.

4.5. References

1. Ajibade P. A. & Zulu N. H. Synthesis, characterization, and antibacterial activity of metal complexes of phenylthiourea. *J. Coord. Chem.* **63,** 3229–3239 (2010).
2. Sacht C., Datt M. S., Otto S. & Roodt A. Synthesis, characterisation and coordination chemistry of novel chiral N,N-dialkyl-N ′-menthyloxycarbonylthioureas. *J. Chem. Soc. Dalt. Trans.* 4579–4586 (2000).
3. Zuckerman R. L. & Bergman R. G. Structural factors that influence the course of overall [2+2] cycloaddition reactions between imidozirconocene complexes and heterocumulenes. *Organometallics* **19,** 4795–4809 (2000).
4. Henderson W., Kemmitt R., Mason S. & Moore M. Thiad iazatrimethylenemethane and N,N',p-triphenyl- phosphonothioic diamide complexes of platinum(II). *J. Chem. Soc., Dalt. Trans.* **1,** 59–66 (1992).
5. Rossenheim A. Notiz iiber die Absorptionsspektra von Losungen isomerer komplexer Kobaltsalze. *Z. Anorg. Chem.* **49,** 28–33 (1906).
6. Moloto M.J., Revaprasadu N., Kolawole G.A., O'Brien P., Malik M. A. The synthesis and characterization of Cu_xS_y and PbS nanoparticles from alkylthiourea lead and copper complexes. *S. Afr. J. Sci.* **1,** 463–465 (2005).
7. Moloto M.J., Revaprasadu N., O'Brien P. & Malik M. A. N-alkylthioureacadmium (II) complexes as novel precursors for the synthesis of CdS nanoparticles. *J. Mater. Sci. Mater. Electron.* **1,** 313–316 (2004).
8. Li S.L., Pradhan N. & Wang Y. High quality ZnSe and ZnS nanocrystals formed by activating zinc carboxylate precursors. *Nano Lett.* **4,** 2261–2264 (2004).
9. Marqusee J.A. Theory of Ostwald ripening: Competitive growth and its dependence on volume fraction. *J. Chem. Phys.* **1,** 536–550 (1984).
10. Trindade T. & O'Brien P. Nanocrystalline semiconductors: Synthesis, properties, and perspectives. *Chem. Mater.* **11,** 3843–3858 (2001).
11. Jia X., Zhang P., Lin Z., Anthony R., Kortshagen U., Huang S. & Puthen-Veettil B. Accurate determination of the size distribution of Si nanocrystals from PL spectra. *RSC Adv.* **5,** 55119–55125 (2015).
12. Khaleduzzaman S. S., Mahbubul I. M., Shahrul I. M. & Saidur R. Effect of particle

concentration, temperature and surfactant on surface tension of nanofluids. *Int. Commun. Heat Mass Transf.* **49,** 110–114 (2013).

13. Bhuiyan M. H. U., Saidur R., Amalina M. A., Mostafizur R. M. & Islam A. Effect of nanoparticles concentration and their sizes on surface tension of nanofluids. *Procedia Eng.* **105,** 431–437 (2015).
14. Javed R., Usman M., Tabassum S. & Zia M. Effect of capping agents: Structural, optical and biological properties of ZnO nanoparticles. *Appl. Surf. Sci.* **386,** 319–326 (2016).
15. López-Serrano A. Comparison of bioconcentration of ionic silver and silver nanoparticles in zebrafish eleutheroembryos. *Environ. Pollut.* **191,** 207–214 (2014).
16. Nair S., Sasidharan A., Rani D., Menon D., Nair S. & Manzoor K. Role of size scale of ZnO nanoparticles and microparticles on toxicity toward bacteria and osteoblast cancer cells. *J. Mater. Sci. Mater. Med.* **20,** 235–241 (2009).
17. Mohamed M. B., Wang Z. L. & El-Sayed M. A. Temperature-dependent size-controlled nucleation and growth of gold nanoclusters. *J. Phys. Chem. A* **103,** 10255–10259 (1999).
18. Oskam G. Metal oxide nanoparticles: Synthesis, characterization and application. *J. Sol-Gel Sci. Technol.* **37,** 161–164 (2006).

Chapter 5: Photocatalytic degradation of Rhodamine B using the as-synthesized ZnS photocatalysts

5.1. Introduction

The photocatalytic oxidation of organic and biological molecules is considered one of the most efficient methods used for the treatment of wastewater from the toxic pollutants released from textile and other industrial processes.[1] The quick oxidation, high efficiencies and no formation of polycyclic products makes the photocatalytic technique advantageous over the previously used traditional techniques.[2] The photocatalytic activity of semiconductor materials can be controlled by three key factors: light absorption property, the rate of reduction and oxidation of reaction substrates by, the electron and hole, and the rate of electron–hole recombination. These factors are mostly governed by the crystal structure, particle size and surface texture of the semiconductor. The structure of semiconductors depends upon the synthesis methods and conditions. The size effects originate primarily from the size quantization in nanoscale that can change the band gap of semiconductor and size-related surface characteristics such as surface area and defects. The redox potential of the reaction substrates, which adsorbed on the surface varies to the surface chemical structure and the amount of adsorbed substrates, depends more directly on the specific surface area. Thereby the high surface area to volume ratio of particles in nano-size regime appears to be an important parameter for seeking to synthesize photocatalytic materials in nanoscale.[3] An ideal photocatalytic material would operate on a combination of high activity regarding the relevant process of interest and high efficiency of solar energy conversion. The photocatalyst materials should also be stable over a long period of the operation. However, no such material or system currently ever exists to satisfy all these requirements.[4]

TiO_2 is an excellent photocatalyst for the degradation of organic contaminants in water and air. Most organic compounds are degraded to CO_2, H_2O, and appropriate inorganic ions on exposure to TiO_2 in the presence of light and oxygen.[5] A distinct hindrance, however, for more widespread application of TiO_2 as a catalyst is its lack of absorption in the visible

spectrum and its relatively low efficiency due to fast recombination rates.[6] TiO_2 has three common crystalline polymorphs: anatase, rutile and brookite. The crystalline phase, brookite is known to be inactive for water treatment, while studies have been made intensively in order to determine the most active crystalline phase, anatase or rutile, it is widely held that anatase (band gap = 3.2 eV, absorption ≤ 385 nm) is the most active photocatalyst.[7] Semiconductor nanoparticles such as ZnO and ZnS bear the potential to have many of these right entities. ZnO has been reported to be a suitable alternative to TiO_2 since its photodegradation mechanism has been proven to be similar to that of TiO_2.[8] In fact, ZnO has been reported, sometimes, to be more efficient than TiO_2, its efficiency has been reported to be particularly noticeable in the advanced oxidation of pulp mill bleaching wastewater.[9] ZnS nanocrystals are also believed to hold the potential to be effective photocatalysts, resulting from their rapid generation of electron–hole pairs and the highly negative redox potentials of excited electrons.[10] While ZnO and TiO_2 photocatalytic activities have been widely reported,[11–15] very little work has been carried out on the photocatalytic activity of ZnS nanoparticles. One study performed by Soltani *et al.*[6] which aimed to enhance the photocatalytic activity of ZnS nanoparticles by coating them with polyvinyl pyrrolidone (PVP) revealed that while the photocatalytic activity improved compared to the uncapped particles, the PVP-capped ZnS nanoparticles were still quite inefficient in the degradation of the methylene blue (MB) dye. They observed that only a little fraction (~ 10 %) of the dye had been degraded after 3 hours of the photocatalytic reaction. He *et al.*[1] enhanced the photocatalytic activity of ZnS nanoparticles by immobilizing the nanocrystals on the surface of fluoropolymer resulting in the formation of nanocomposites and observed a complete degradation of MB after 6 hours. They postulated that degradation proceeds through an adsorption—migration photodegradation, where the dye was first adsorbed by the fluoropolymer nanofibers, then migrated to the ZnS nanoparticles and finally degraded by the ZnS catalyst under UV irradiation. Zegeye's study involved the doping of the ZnS nanoparticles with nitrogen and revealed that only 50% of the MB dye was degraded after 3 hours.[16] In our study of ZnS and by using different precursors to synthesize the ZnS. The aim of this work was therefore to evaluate and compare the photocatalytic degradation rates when using the commercial TiO_2 (anatase), commercial ZnO and the previously synthesized ZnS nanoparticles from the acylthiourea and thiourea complexes. Also, to determine whether there was any advantage in using the acylthiourea complex to synthesize the ZnS nanoparticles over the thiourea complex. The results obtained should be considered preliminary as they

merely provide a good starting point for further investigation on the understanding about the role of the ZnS nanoparticles in determining photocatalytic effectiveness.

5.2. Experimental

1.5.1. Chemicals

For the photocatalytic reactions, Rhodamine B (RhB, $C_{28}H_{31}ClN_2O_3$, and Figure 5.1) was chosen as a pollutant for these studies. Zinc oxide (ZnO) and anatase-titanium dioxide (TiO_2) were of analytical grade and were purchased from Sigma Aldrich. ZnS nanoparticles that displayed optimal properties synthesized from both the ATU and TU ligand were used for photocatalysis testing, conditions used have been summarized in Table 5-1 From the ATU ligand, the nanoparticles used were synthesized for 20 minutes. De-ionized water was obtained from the labs.

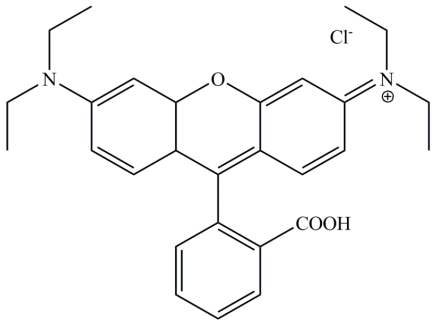


Figure 5.1: The chemical structure of RhB.

Table 5-1: Reaction conditions used to prepare the a-synthesized ZnS nanoparticles from both the ATU and the TU precursors.

Reaction Condition	ZnS-ATU	ZnS-TU
Time (min)	20	20
Temperature (˚C)	200	200
Concentration: [precursor]:[capping agent]	2.5:15	2.5:15
Capping agent	OAm	HDA

1.5.2. Photocatalytic degradation of RhB over commercial and the a-synthesized photocatalysts

The photocatalytic activity of the nanoparticles was investigated by the decomposition of RhB and monitored by the decreasing absorbance of a 20 ppm aqueous solution of RhB. The characteristic optical absorption peak of RhB at 554 nm was used to monitor the photocatalytic degradation process. The reactions were performed by first sonicating a suspension of 0.25 g of the photocatalyst in 100 mL of the RhB solution in the dark. The sonication was carried out for 30 minutes and stirred in the dark for another 1 hour prior to starting the reaction to ensure that all the active sites of catalysts were in contact with the dye solution. The solution was then illuminated with light from the 180-W Xenon arc lamp with continuous stirring. Sampling was performed before the illumination and after illumination; thereafter, samples were obtained periodically to determine the degradation of RhB. The photocatalytic decomposition of RhB was investigated over commercial TiO_2 (anatase), commercial ZnO and the two ZnS samples previously synthesized from the ATU and TU precursors. (Please see Table 5-1)

1.5.3. Characterisation Techniques

5.2.1.1. Powder X-Ray diffraction

X-Ray diffraction (XRD) patterns of powdered samples were measured on Bruker D2 Phaser desktop diffractometer equipped with a LYNXEYE PSD detector (set to measure a 5° 2θ angular range), 2.5° primary and secondary beam Soller slits, and Co X-ray micro-source (Kα with λ = 1.78897 Å) operated at 30 kV and 10 mA. The goniometer radius of the diffractometer was 70.7 mm. The instrument was also fitted with a secondary beam Fe filter to attenuate Kβ radiation and a 3 mm air-scatter slit. Diffraction data were collected in the 2θ range 10-90° in 0.0260° steps and at a count time of 0.5 sec/step.

5.2.1.2. Optical characterization

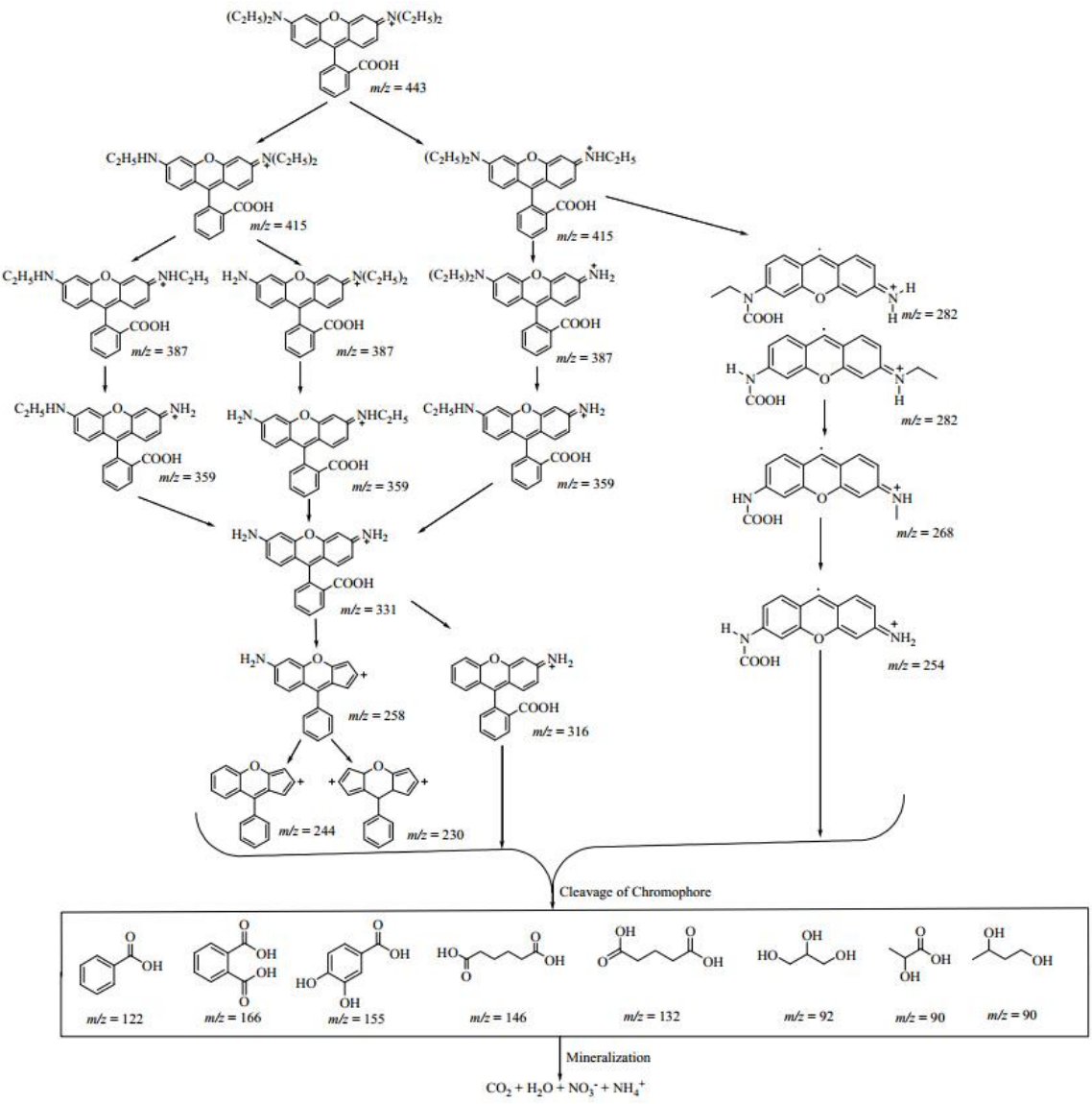
The optical properties of the materials were determined by placing the toluene dispersion of the nanoparticles into quartz cuvettes (1 cm path length). A Perkin Elmer Lambda 75S UV–Vis–NIR Spectrophotometer was used to carry out the optical measurements.

5.2.1.3. Electron microscopy

The transmission electron microscopy (TEM) images were obtained using a Technai G2 TEM Spirit operated at 200 kV. The samples were prepared by placing a drop of a dilute solution of the sample in toluene onto carbon-coated copper grids. The samples were allowed to dry completely at room temperature.

5.3. Results and discussion

Rhodamine B has been shown using mass spectrometry to degrade to form H_2O, CO_2, NO_3^- and NH_4^+ as shown in Scheme 5.1.



Scheme 5.1: Mechanism of photocatalytic mineralization of Rhodamine B.[17]

The photocatalytic degradation of RhB was tested against the two a-synthesized ZnS nanocrystals synthesized from the TU and ATU complexes and activities were compared to those of commercial ZnO and TiO_2 (anatase). [8] X-ray diffraction data displayed in Figure 5.2 confirmed the good crystallinity of the commercial samples. The diffractions of the ZnO indicate the presence of wurtzite structured ZnO (JCPDS card No. 76-0704). Broadening of the XRD peaks in both the ZnS samples in comparison to the commercial samples indicates the smaller sizes in the synthesized ZnS particles. The average crystallite sizes estimated from the planes of the ZnO and TiO_2 (anatase) by the Scherer equation were 39 nm and 45 nm, respectively.

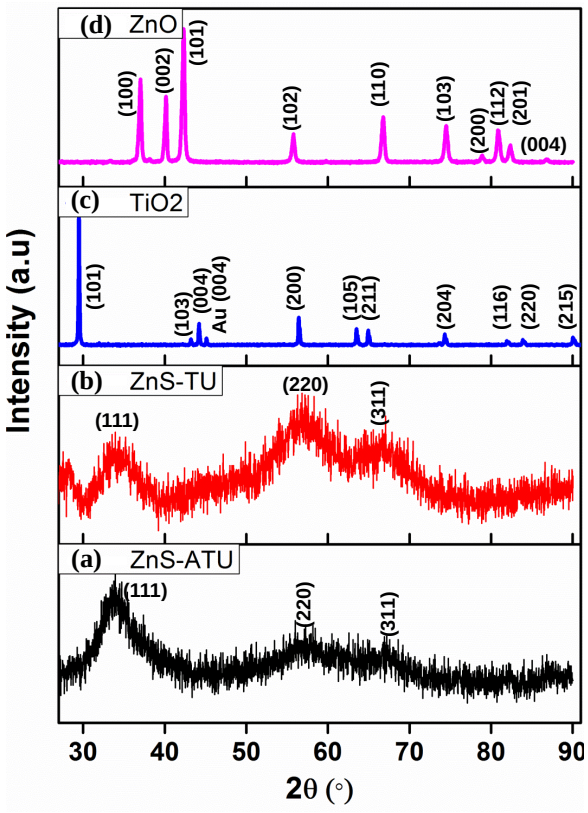


Figure 5.2: XRD pattern of (a) ZnS QDs synthesized from the ATU ligand, (b) ZnS QDs synthesized from the TU ligand, (c) commercial TiO_2 (anatase) and (d) commercial ZnO.

Figure 5.3 shows the TEM micrographs of the synthesized ZnS nanoparticles and the commercial samples obtained from ZnO and TiO_2. The TEM images show the larger particles from the commercial samples and the much smaller samples from the as-synthesized samples clearly in nanosized regime. The results are in accordance with the information deduced from

X-ray diffraction. The TEM micrographs revealed that the ZnO nanoparticles were rod-like in shape and the anatase particles consisted of spheres and cubes while the ZnS nanoparticles remained spherical as previously discussed.

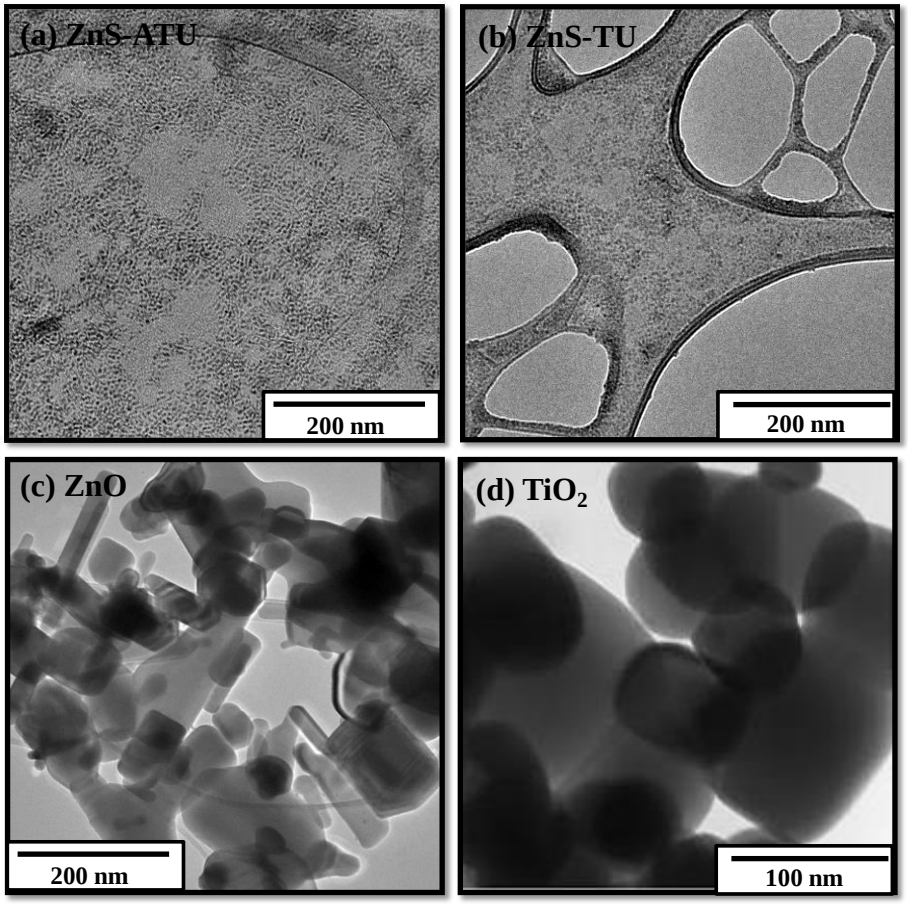


Figure 5.3: TEM micrographs of (a) ZnS QDs synthesized from the ATU ligand, (b) ZnS QDs synthesized from the TU ligand, (c) commercial anatase and (d) commercial ZnO.

The photocatalytic degradation of RhB using commercial TiO_2 and ZnO nanoparticles were initially studied in order to compare the photocatalytic activity of the as-synthesized particles. The corresponding time-dependent absorption spectra of RhB aqueous solutions under the irradiation of UV light are shown in Figure 5.4 and the concentration degradation rates are shown in Figure 5.5. The absorption peaks of RhB when using TiO_2 and ZnO (Figures 5.4(a) and (b), respectively) disappeared completely after 30 min and 15 min, respectively, while it took around 3 and a half hours for the ATU and TU-synthesized ZnS to effectively degrade the RhB.

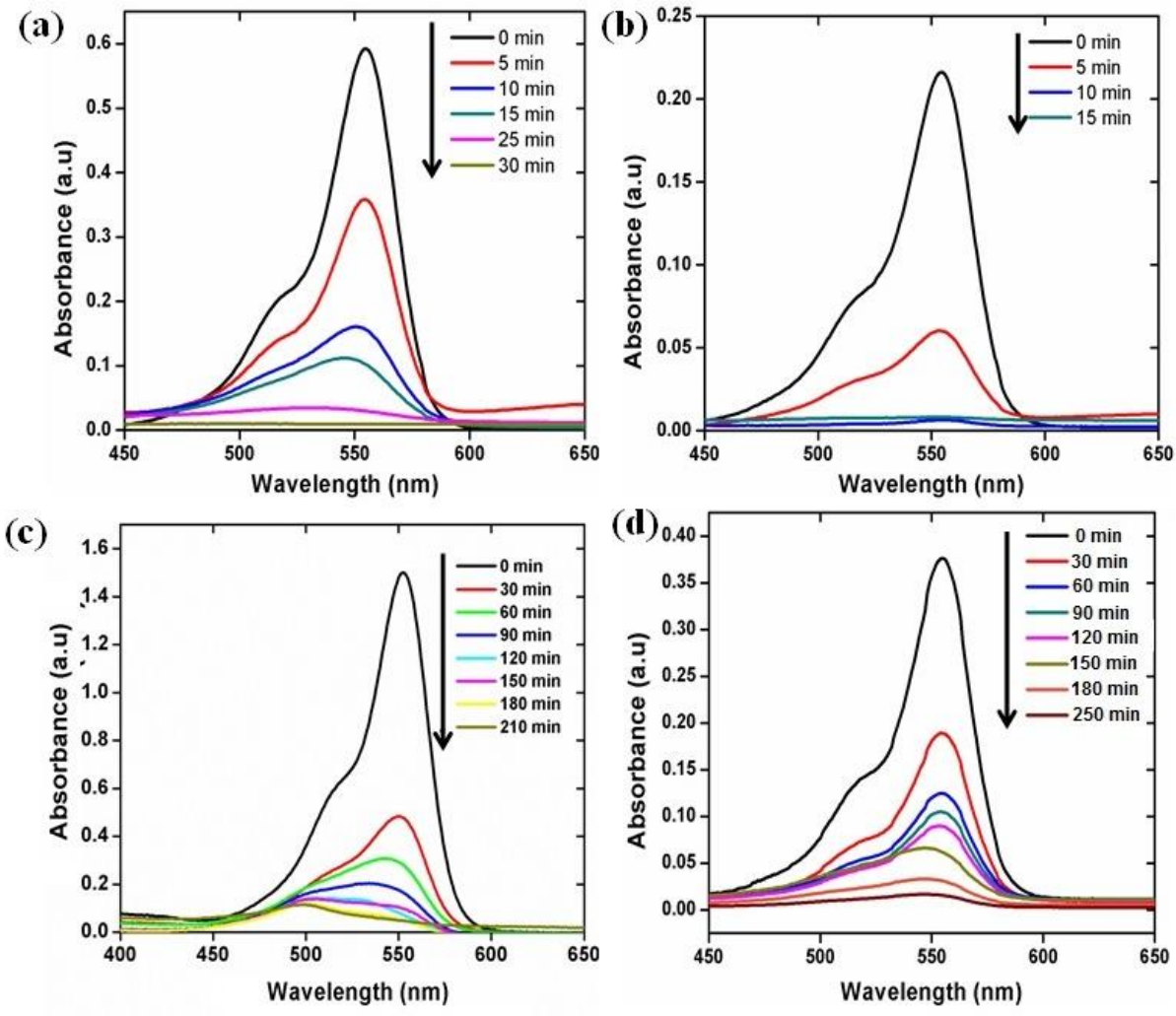


Figure 5.4: The absorbance spectra changes of RhB solution in (a) commercial TiO_2(anatase), (b) commercial ZnO, (c) ZnS nanoparticles synthesized from $Zn(ATU)_2$ and (d) ZnS nanoparticles synthesized from $Zn(TU)_2Cl_2$.

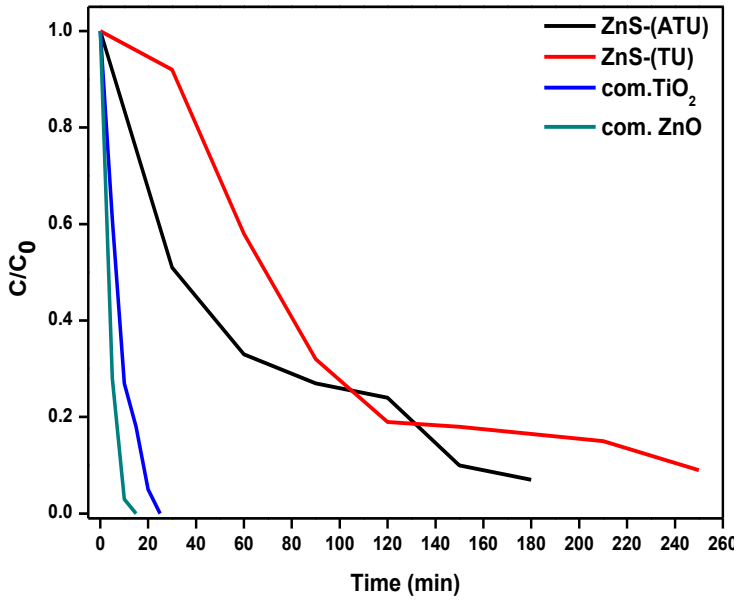


Figure 5.5: Photocatalytic degradation kinetics of RhB using different photocatalysts under visible light. (C_0 and C are the equilibrium concentrations of RhB before and after irradiation, respectively).

Compared to the commercial catalysts, the synthesized ZnS photocatalysts required longer times to degrade the dye. Since the photo-assisted degradation of dyes occurs predominantly on the surface of the photocatalyst [18], the commercial photocatalysts which were not capped by any surfactant had a greater advantage in this regard, hence the better photocatalytic activity. Furthermore, the lack of surfactant on the commercial photocatalysts makes them more hydrophilic and able to absorb more RhB molecules in water,[19] as opposed the hydrophobic surfactants used in the synthesis of the ZnS nanoparticles. The ZnO photocatalyst showed better photocatalytic activity over the TiO_2 photocatalyst probably due to the larger surface area as a result of the rod-like particles.

5.4. Conclusions

The ATU-synthesized ZnS nanoparticles displayed marginally higher photocatalytic activity compared to the TU-synthesized ZnS. These results may not have shown the complete degradation of RhB, and times may have been longer. The photocatalytic activity may not be ideally fast but certain parameters can be monitored and varied in order to improve it, these parameters include the pH of the solution, the loading of the photocatalyst and the intensity of

the light used to degrade the dye. In addition, the small sizes of the nanoparticles versus the long-chained ligands can possibly result in poor interaction of the light with the ZnS core.

5.5. References

1. He T., Ma H., Zhou Z., Xu W. & Ren F. Preparation of ZnS-Fluoropolymer nanocomposites and its photocatalytic degradation of methylene blue. *Polym. Degrad. Stab.* **94,** 2251–2256 (2009).
2. Rajabi H. R., Khani O., Shamsipur M. & Vatanpour V. High-performance pure and Fe^{3+}-ion doped ZnS quantum dots as green nanophotocatalysts for the removal of malachite green under UV-light irradiation. *J. Hazard. Mater.* **250,** 370–378 (2013).
3. Leary R. & Westwood A. Carbonaceous nanomaterials for the enhancement of TiO_2 photocatalysis. *Carbon N. Y.* **49,** 741–772 (2011).
4. Janin T., Goetz V., Brosillon S. & Plantard G. Solar photocatalytic mineralization of 2,4-dichlorophenol and mixtures of pesticides: Kinetic model of mineralization. *Sol. Energy* **87,** 127–135 (2013).
5. Lee S. Y. & Park S. J. TiO_2 photocatalyst for water treatment applications. *J. Ind. Eng. Chem.* **19,** 1761–1769 (2013).
6. Soltani N., Saion E., Yunus M., Navasery M & Rezaee K.. Enhancement of visible light photocatalytic activity of ZnS and CdS nanoparticles based on organic and inorganic coating. *Appl. Surf. Sci.* **290,** 440–447 (2014).
7. Kumar S. G. & Devi L. G. Review on modified TiO_2 photocatalysis under UV/visible light: Selected results and related mechanisms on interfacial charge carrier transfer dynamics. *J. Phys. Chem. A* **115,** 13211–13241 (2011).
8. Dindar B. & Içli S. Unusual photoreactivity of zinc oxide irradiated by concentrated sunlight. *J. Photochem. Photobiol. A Chem.* **140,** 263–268 (2001).
9. Kumar S. G. & Saion E. Photocatalysis, *J. Photochem. Photobiol. A Chem.* **39,** 1679–1688 (1999).
10. Kansal S. K., Singh M. & Sud D. Studies on photodegradation of two commercial dyes in aqueous phase using different photocatalysts. *J. Hazard. Mater.* **141,** 581–590 (2007).
11. Benjamin S., Vaya D., Punjabi P. B. & Ameta S. C. Enhancing photocatalytic activity of zinc oxide by coating with some natural pigments. *Arab. J. Chem.* **4,** 205–209 (2011).

12. Apostolescu G. A., Cernatescu C., Cobzaru C., Tataru-farmus R. E. & Apostolescu N. Studies on the photocatalytic degradation of organic dyes using CeO_2-ZnO mixed oxides. **14,** 415–420 (2015).
13. Khezrianjoo, S. & Revanasiddappa, H. D. Photocatalytic Degradation of Acid Yellow 36 Using Zinc Oxide Photocatalyst in Aqueous Media. **20,** 420-450 (2013).
14. Sakthivel S., Shankar M., Arabindoo B. & Palanichamy M. Solar photocatalytic degradation of azo dye. *J. Photochem. Photobiol.* **77,** 65–82 (2003).
15. Chakrabarti S. & Dutta B. K. Photocatalytic degradation of model textile dyes in wastewater using ZnO as semiconductor catalyst. *J. Hazard. Mater.* **112,** 269–278 (2004).
16. Zegeye D. Z. Photocatalytic Activity of N-doped ZnS nanoparticles for degradation of organic pollutant (methylene blue). **5,** 214–219 (2016).
17. Wan-Kuen R. J. T. Recent developments in photocatalytic dye degradation upon irradiation with energy-efficient light emitting diodes. *Chinese J. Catal.* **35,** 108–119 (2014).
18. Rashad M. M., Ismail A. A., Osama I., Ibrahim I. A. & Kandil A. H. T. Photocatalytic decomposition of dyes using ZnO doped SnO2 nanoparticles prepared by solvothermal method. *Arab. J. Chem.* **7,** 71–77 (2014).
19. Sudha M., Senthilkumar S., Hariharan R., Suganthi A. & Rajarajan M. Synthesis, characterization and study of photocatalytic activity of surface modified ZnO nanoparticles by PEG capping. *J. Sol-Gel Sci. Technol.* **65,** 301–310 (2013).

Summary and Recommendations

The synthesis and structural characterization of the ATU ligand has been completed. The coordination of the ATU ligand to the Zn metal center has been studied in detail, together with the coordination of the TU ligand to the Zn metal center. Elemental analysis, NMR, FTIR and mass spectrometry have been used to confirm the successful synthesis of the Zn complexes. Studies on the thermolysis profiles of (*N*,*N*-diethyl-*N'*-benzoyl(thiourea) ZnII) and bis(diaminomethylhio)Zn(II) complexes suggest the formation of ZnS nanoparticles, confirming their potential as single-source precursors for the synthesis of ZnS quantum dots. Optimization studies revealed that the formation of ZnS nanoparticles from the thermolysis of their respective precursors takes place over a range of different temperatures, time, concentration and capping agents. A direct correlation between thermolysis reaction parameters and nanoparticle diameter was evident, this being further reflected in the size-dependent emission of the nanoparticles. From these investigations it was apparent that varying the reaction conditions had little influence on the morphology. Preliminary investigations into the use of the ATU- and TU- synthesized ZnS nanoparticles as photocatalysts in the degradation of Rhodamine B (RhB) were successfully carried out. ZnS nanoparticles that displayed optimal properties from each precursor were used and their photocatalytic activities were compared to the commercial TiO_2 and ZnO. The degradation times of the RhB dye when using the ZnS nanoparticles were on average 3 hours, showing the potential to use ZnS nanoparticles synthesized from single-source precursors as photocatalysts. While commercial photocatalysts still displayed better degradation times and photocatalytic activities with total degradation of the dye after 30 min, this was seen as an opportunity and an open door for further investigation in the optimization of the synthesis and the preparation of monodisperse, evenly passivated material.

In future, it would be interesting to alter the chemistry of the benzene ring in order to influence the reactivity of Zn-O bond by adding electron donating and electron withdrawing groups. The photocatalytic activities could potentially be improved by using less bulky capping agents as they may interfere with the interaction of the light with the core ZnS. This can be achieved through ligand exchange, by removing the long chained organic ligands (OAm, HDA and etc.) to shorter chained ligands such as ethanethiol or mercaptopropionic

acid for example. The post ligand exchange is necessary as it has been shown that direct synthesis using shorter chained ligands yields nanoparticles with inferior quality which are polydispersed and agglomerated samples are usually obtained. It would also be of great interest to determine with high-resolution Mass Spectrometry what the degradation products are.